AFOSR-TR- 88-1273



Prepared for
Air Force Office of Scientific Research
under the
University Research Initiative Program

# CENTER FOR THIN FILM STUDIES

## ANNUAL REPORT





Robert R. Shannon
Optical Sciences Center
University of Arizona
Tucson, Arizona 85721



October 31, 1988

UNCLASSIFIED
SECURITY CLASSIFICATION OF THIS PAGE

# REPORT DOCUMENTATION PAGE

Form Approved OMB No. 0704-0188

| | |
|---|---|
| 1a. REPORT SECURITY CLASSIFICATION: Unclassified | 1b. RESTRICTIVE MARKINGS: |
| 2a. SECURITY CLASSIFICATION AUTHORITY | 3. DISTRIBUTION/AVAILABILITY OF REPORT: Approved for public release; distribution unlimited. |
| 2b. DECLASSIFICATION/DOWNGRADING SCHEDULE | |
| 4. PERFORMING ORGANIZATION REPORT NUMBER(S) | 5. MONITORING ORGANIZATION REPORT NUMBER(S): AFOSR-TR- 88-1273 |
| 6a. NAME OF PERFORMING ORGANIZATION: Optical Sciences Center; 6b. OFFICE SYMBOL (If applicable): | 7a. NAME OF MONITORING ORGANIZATION: ~~UNIRR~~ AFOSR |
| 6c. ADDRESS (City, State, and ZIP Code): University of Arizona, Tucson, Arizona 85721 | 7b. ADDRESS (City, State, and ZIP Code): Bld 410, Bolling AFB DC 20332-6448 |
| 8a. NAME OF FUNDING/SPONSORING ORGANIZATION: ~~USAF AFSC~~ AFOSR; 8b. OFFICE SYMBOL (If applicable): ~~F08671~~ NE | 9. PROCUREMENT INSTRUMENT IDENTIFICATION NUMBER: F49620-86-C-~~0~~-0123 |
| 8c. ADDRESS (City, State, and ZIP Code): Air Force Office of Scientific Research, Building 410, Bolling AFB, Washington, DC 20332-6448 | 10. SOURCE OF FUNDING NUMBERS: PROGRAM ELEMENT NO. 61102F; PROJECT NO. 3484; TASK NO. A3; WORK UNIT ACCESSION NO. |

11. TITLE (Include Security Classification)

Center for Thin Film Studies (unclassified)

12. PERSONAL AUTHOR(S) Robert R. Shannon, Ursula J. Gibson, et al.

| 13a. TYPE OF REPORT | 13b. TIME COVERED | 14. DATE OF REPORT (Year, Month, Day) | 15. PAGE COUNT |
|---|---|---|---|
| Annual | FROM 10/1/87 TO 10/1/88 | 10/31/88 | 171 |

16. SUPPLEMENTARY NOTATION

| 17. COSATI CODES | | | 18. SUBJECT TERMS (Continue on reverse if necessary and identify by block number) |
|---|---|---|---|
| FIELD | GROUP | SUB-GROUP | |
| | | | |
| | | | |

19. ABSTRACT (Continue on reverse if necessary and identify by block number)

This report covers the second year of operation of the URI Thin Film Center.

This report contains a summary of the research performed under this umbrella grant; separate sections cover work on growth and characterization of thin films by different methods, modeling of thin film growth, and preparation and characterization of substrates for growth.

The task numbers have been reassigned from the previous year.

(myn)

(1)

| 20. DISTRIBUTION/AVAILABILITY OF ABSTRACT | 21. ABSTRACT SECURITY CLASSIFICATION |
|---|---|
| ☒ UNCLASSIFIED/UNLIMITED ☐ SAME AS RPT. ☐ DTIC USERS | Unclassified |
| 22a. NAME OF RESPONSIBLE INDIVIDUAL: ~~Floyd L. Lance~~ Lilton | 22b. TELEPHONE (Include Area Code): ~~(602) 621-6996~~ 202 767-4931 |
| | 22c. OFFICE SYMBOL: NE |

DD Form 1473, JUN 86 — Previous editions are obsolete. — SECURITY CLASSIFICATION OF THIS PAGE

UNCLASSIFIED

## CONTENTS

## INTRODUCTION

The Center for Thin Film Studies was formed in 1986 under the University Research Initiative Program, funded by the Air Force Office of Scientific Research.

This report contains a summary of the research performed under this umbrella grant; separate sections cover work on growth and characterization of thin films by different methods, modeling of thin film growth, and preparation and characterization of substrates for growth.

The task numbers have been reassigned from the previous year.

The work described herein was performed under Contract # F49620-86-C-0123P00001.

TASK 1

# NUCLEATION AND GROWTH STUDIES BY CONVENTIONAL AND ATOMIC LAYER EVAPORATION

Principal Investigator: U. J. Gibson

## Project Goal

The goal of the project is to study the details of nucleation and film growth, primarily in systems that lend themselves to deposition by different evaporation methods. The research over the last year had two major thrusts: 1) study of the properties of, and manipulation of growth habits in, conventional and ion-assisted ZnS deposition, and 2) detailed study of the formation of initial layers of ZnS by molecular beam epitaxy (MBE) and atomic layer evaporation (ALE) on substrates prepared using different protocols.

## Work Accomplished

### *ZnS Films*

ZnS is an interesting material for many reasons, including its high refractive index, wide transparency range, and a large thermal nonlinearity that is useful for demonstration experiments. It is also an interesting system for studies of growth, since it is one of the few materials that form compressive thin films when deposited at room temperature. This is believed to occur because the Zn and S dissociate during evaporation, and the individual mobilities of the elements dominate the growth kinetics at the substrate. It thus fails to fit into the empirical structure zone model, and may provide more rigorous tests of first principle theories of film growth.

The properties of ZnS films were studied using waveguiding experiments, x-ray diffraction, electron microscopy, and, in collaboration with G. Stegeman, Brillouin scattering and second harmonic generation measurements. Rutherford backscattering spectroscopy (RBS) was also an invaluable resource.

Despite extensive development for integrated optics applications, waveguiding techniques have been used only recently for analysis of the properties of thin films. Single layers can be analyzed readily to determine thickness and refractive index, and waveguiding techniques provide an extremely sensitive measure of losses caused by both absorptive and scattering mechanisms.

*Structural and waveguide studies*

The waveguide loss effects of water vapor and oxygen partial pressures during evaporation were reported on previously.[1] Changes in the orientation and average sizes of the grains within the film were correlated with these partial pressures. Those experiments indicated that the dominant loss mechanism in ZnS waveguides was scattering from large crystallites. The crystallite size is strongly dependent on substrate temperature, and implementation of substrate cooling has allowed achievement of essentially amorphous films. ZnS crystallite size (determined by XRD) as a function of deposition temperature is shown in Fig. 1. Using cooled substrates, reductions of waveguide losses from approximately 10 dB/cm to less than 0.5 dB/cm in the red, and from 25 dB/cm to less than 5 dB/cm in the green, have been achieved. These lower losses may permit further investigation and exploitation of the nonlinear properties of ZnS in integrated optics applications.

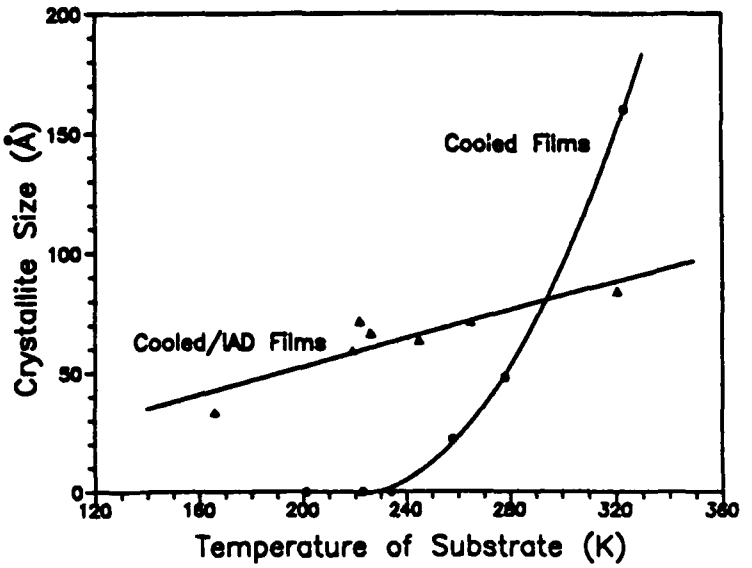


*Figure 1. ZnS crystallite size versus the substrate temperature during deposition.*

The films made at reduced temperatures also have reduced indices of refraction, as shown in Fig. 2. The observed reduction for cooled films may be caused by formation of ZnO during deposition, or by a fibrous or columnar structure with a large volume of pores. At present, there is evidence for each of these models. RBS analysis reveals a stoichiometric Zn to S ratio, favoring the porosity model. High-power waveguiding experiments also displayed long-term instabilities, which may be caused by water desorption; vacuum waveguiding experiments will be undertaken to clarify these results. Alternatively, neither electron microscopy nor second harmonic generation studies revealed evidence of columnar growth for the cooled films.

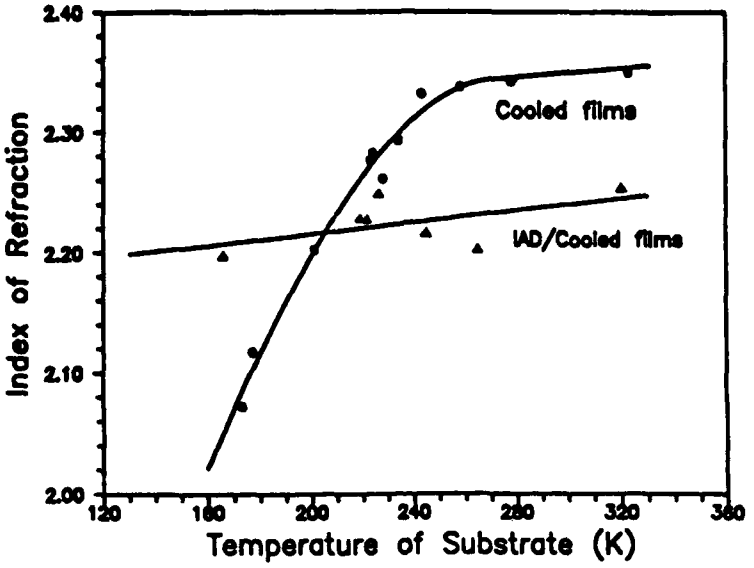


*Figure 2. Index of refraction versus substrate temperature.*

The structure zone model of Movchan and Demchishin predicts a changeover from a columnar film to an equiaxed grain structure at a temperature of approximately 0.45 $T_m$, where $T_m$ is the melting point of the material being deposited. For ZnS, the melting temperature is 1830°C, implying a transition temperature of 673°C, whereas films deposited at temperatures as low as 30°C display the dense structure expected above the transition. If $T_m$ for Zn is used, the transition would be expected at approximately 38°C. It is more difficult to assign a value for the sulfur transition, since sulfur clusters of different sizes (2, 4, 8) are readily formed. For $S_8$, the transition temperature would be about -98°C. Obviously, assigning these individual values is less than entirely appropriate. Work on use of mobilities and chemical potentials to describe the competing mechanisms in growth of these films is underway in Task 4.

Index-of-refraction data for ion-assisted deposition at low temperatures are shown in Fig. 2. In this case, the reduction of index is much less masked. Chemical changes induced by the bombardment compete with densification effects. RBS indicates the presence of significant amounts of argon in the films, as well as a sulfur deficiency. These results suggest use of $H_2S$ as the bombarding species in future work.

*Stress changes*

A significant change in the stress properties of ZnS has also been observed on cooling, with the stress going from compressive at room temperature, to strongly tensile at -100°C. At about -50°C, the stress is minimized, and much thicker layers than normally achievable are readily attained. This may have significant impact on the deposition of narrow-band filters, where stress effects often limit the choice of materials and the maximum spacer layer thicknesses. Compressive stress problems are particularly severe in ion-beam-sputtered coatings; the results of this work suggest the use of a cooled substrate for these depositions. Further studies on ion-assisted deposition are aimed at understanding the potential of the combination of energetic bombardment with a reduced temperature substrate.

*Second harmonic studies*

Earlier results on the sensitivity of the second harmonic generation (SHG) process to columnar structure[2] led to similar studies in ZnS, a material in which second harmonic generation is a symmetry-allowed process. However, ambient temperature depositions often resulted in preferential crystal orientation of the ZnS, which dominated the column-induced anisotropy in the second harmonic signal. Ion bombardment during deposition was used in an attempt to quench the preferential orientation; this merely introduced additional texture into the SHG signal. Recently, ZnS was deposited at low temperature (-50°C), with a substrate incidence angle of 30 degrees. Conventional wisdom implies that this would result in a highly columnar microstructure, with a clear anisotropy in SHG. It was found, however, that the SHG signal, while still strong, gave no indication of the formation of columns. The measurement geometry is shown in Fig. 3a. The results of SHG measurements for 1) ZnS deposited at room temperature (without preferential orientation), 2) ion-assisted ZnS deposition, with evidence of additional symmetry breaking caused by the beam, 3) the room-temperature film measured with $\theta \neq 0$, and 4) a cooled film measured at the same $\theta$ are shown in Fig. 3b. For $\theta = 0$, there was no signal from the cooled film, indicating symmetry in the plane of the film. All films were deposited with a vapor incidence angle of 30 degrees to the substrate normal.

*Brillouin Samples*

ZnS samples were also prepared for Brillouin adhesion studies, as described in the Task 3 report.

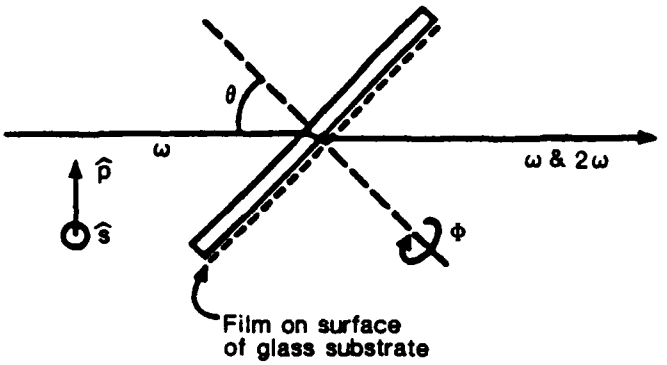


(a)

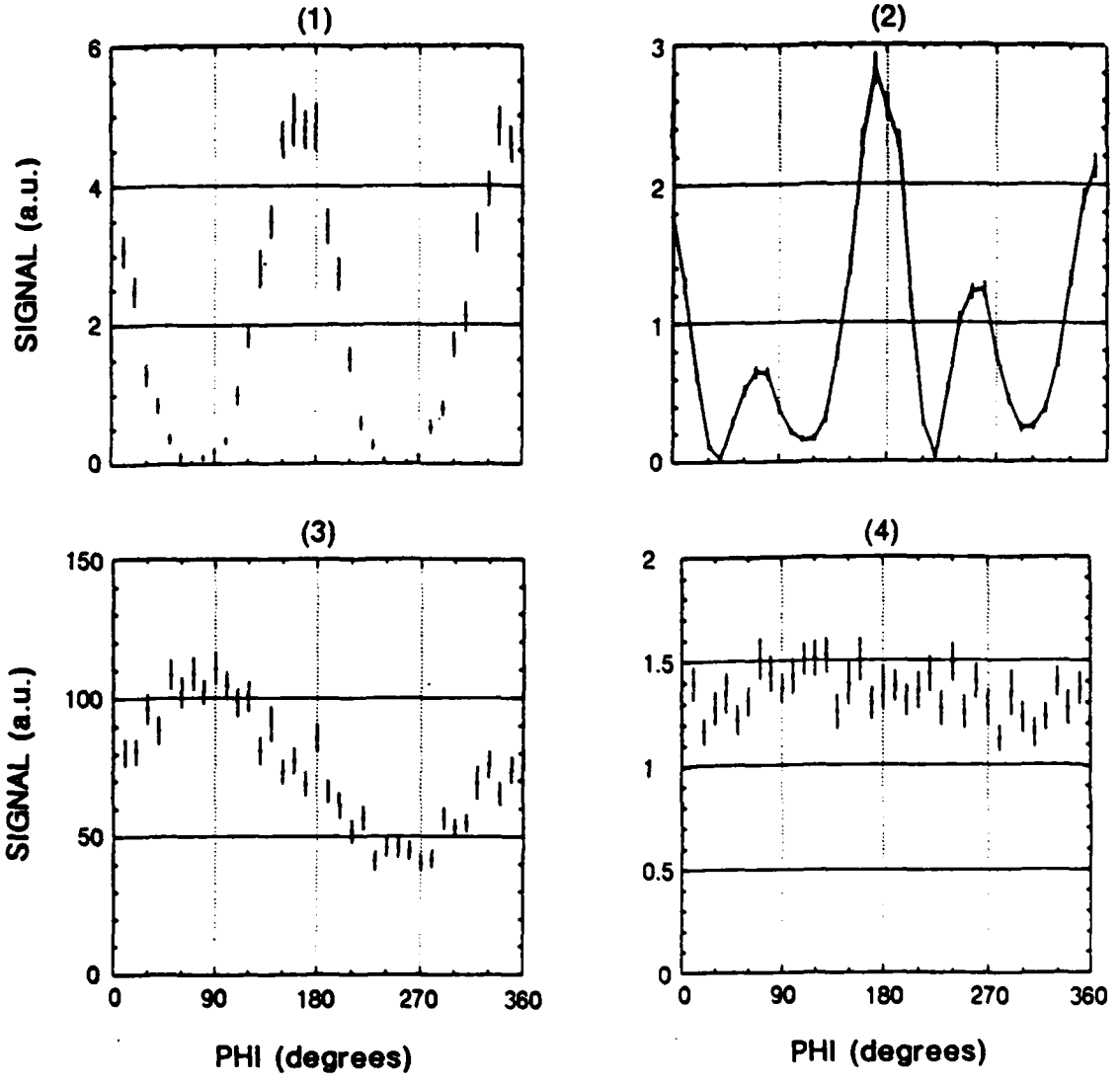


(b)

*Figure 3. (a) SHG measurement geometry; (b) SHG ZnS results: (1) ambient temperature, non-IAD; (2) ambient temperature, IAD; (3) ambient temperature, non-IAD, θ ≠ 0; (4) temperature -36°C, non-IAD, θ ≠ 0.*

*UHV Studies*

Investigations of the nucleation and growth behavior of ZnS films, deposited in ultra-high vacuum (UHV) from a molecular source and from reactive materials, also have been performed.

ZnS films were deposited onto oxidized single-crystal Si under UHV conditions for comparison with conventionally evaporated films. However, the large grain size and high internal stress resulted in high scatter and short lifetimes. Epitaxial films have been deposited onto Si, and investigated by a number of techniques. One such film was mechanically damaged, thus inducing microcracks, and submitted for Brillouin testing, as described in the Task 3 report.

Studies of the nucleation and substrate interaction behavior were undertaken to elucidate the role of cleaning procedures in ZnS growth on Si wafers, and to understand the critical first-layer growth in ALE of ZnS. In particular, the role of exposure of the Si to $H_2S$ during heating, prior to deposition, was of interest. It was found that the presence of $H_2S$ did not significantly affect the temperature at which RHEED spots were first observable, but it did significantly affect the surface impurity concentrations, as observed by XPS. Lower concentrations of both C and O were observed with $H_2S$ treatment.

Depositions of thin Zn layers onto Si substrates prepared with the $H_2S$ treatment gave a strong indication of a preference for a layer-by-layer growth habit, whereas high-aspect ratio islands were observed without the $H_2S$. Angle-resolved XPS data were taken on the ratio of the Zn to substrate (Si) signal, and analyzed according to the Fadley model for the two cases, as shown in Figs. 4a and 4b. For the substrates exposed to $H_2S$ after cleaning and heating, the Zn formed a thin layer over approximately 80% of the substrate surface. The incomplete coverage is attributed to oxygen impurities blocking sulfur bonding at the interface. For the substrates exposed to Zn following attainment of a RHEED pattern, but with no $H_2S$ exposure, the slope of the curve of the Zn:Si ratio versus theta is discontinuous, indicating that there are large aspect ratio islands of Zn forming in preference to continuous layers.

**Plans**

In the coming year, additional work will be performed to determine the structure of cooled ZnS films, using both optical and electron microscopy techniques, and to investigate the simultaneous use of ion bombardment and substrate cooling for production of low-loss, stable ZnS material.

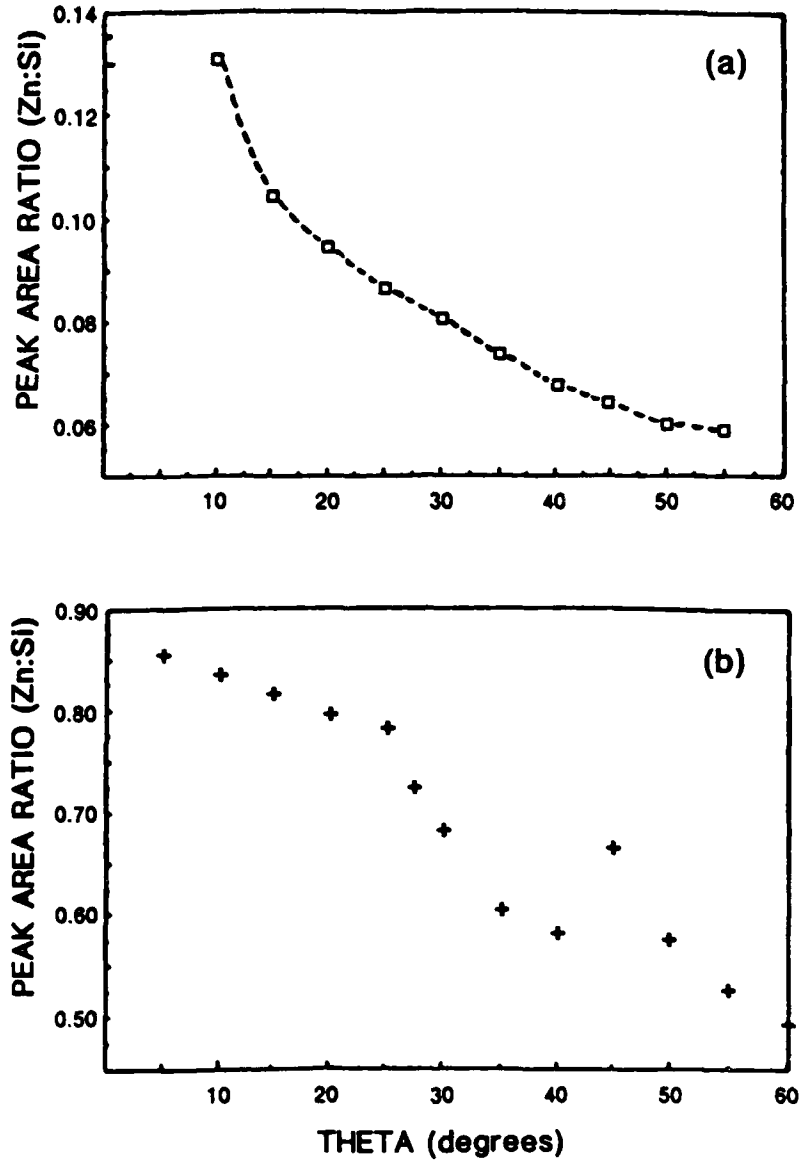


*Figure 4. Zn:Si XPS data: (a) substrate exposed to $H_2S$ - the squares are data points, the dashed line is the Fadley fit for 50% coverage; (b) substrate not exposed to $H_2S$ - the crosses are data points, no Fadley fit possible.*

It is hoped that comparison of these and SHG studies on a material such as $MgF_2$, which evaporates molecularly, can be made to determine the importance of the evaporative dissociation of ZnS in determining its growth patterns.

The nucleation studies will also be pursued to illuminate the formation of subsequent layers in ALE deposition. The treatment chamber will be used for these studies, and the MBE system will be used for thick layers and deposition of other materials.

Experiments are also planned to test some of the theoretical predictions made in the other Tasks regarding the development of columnar structure. In particular, Al films will be studied to test the dependence of column size on deposition rate.

## Personnel

U. Gibson

J. Watanabe

J. Ruffner

B. Williams

F. Suits

## Collaborations

Macleod: XPS analysis of oxynitride films

Leavitt and McIntyre: RBS

Stegeman and Seaton: Brillouin and SHG studies

Lichter: Columnar growth model, chemical potential model

Lindley: Preparation of opal, thin film samples for EM and STM studies

## Publications


1. M. D. Himel, J. A. Ruffner, and U. J. Gibson, "Stress modification and reduced waveguide losses in ZnS thin films," Appl. Opt. 27, 2810 (1988).

2. M. D. Himel, J. A. Ruffner, and U. J. Gibson, "Microstructure effects on light propagation in ZnS waveguides," in 1988 Technical Digest Series, vol. 6 (Optical Society of America, Washington DC, 1988).

3. F. Suits and U. J. Gibson, "Optical response of a composite medium consisting of metal particles in a nonlinear dielectric host," in 1988 Technical Digest Series, vol. 9 (Optical Society of America, Washington DC, 1988).

4. F. Suits and U. J. Gibson, "Optical response of a composite medium consisting of metal particles in a nonlinear dielectric host," submitted to JOSA B.

5. J. K. Watanabe, A. J. Stentz and U. J. Gibson, "XPS and RHEED studies of Si(100) substrate preparation for epitaxial ZnS growth," in preparation.

*Abstracts*

6. M. D. Himel, J. A. Ruffner, and U. J. Gibson, "Modification of structure and waveguide properties of evaporated ZnS films," Opt. News 14, 179 (1988).

7. J. A. Ruffner, M. D. Himel, and U. J. Gibson, "Stress modification in ZnS thin films," Opt. News 14, 207 (1988).

8. J. K. Watanabe, A. J. Stentz, and U. J. Gibson, AUS meeting, Denver, CO.

## References


1. M. D. Himel, J. A. Ruffner, and U. J. Gibson, Proc. SPIE 835, 32 (1987).

2. V. Mizrahi, F. Suits, J. E. Sipe, U. J. Gibson, and G. I. Stegeman, Appl. Phys. Lett. 51(6), 427 (1987).

TASK 2

## ION-ASSISTED DEPOSITION AND MODELING

Principal Investigators: Bertrand G. Bovard and H. Angus Macleod

### Project Goals

Investigate the use of ion-assisted deposition (IAD) for modification of film structure, and determine its utility for improving the performance of optical films.

Develop a model of film growth that includes the range of effects present in an actual coating chamber.

### Work Accomplished

*Ion-Assisted Deposition*

Work on the ion-assisted deposition (IAD) of metals has continued. Some of the results quoted here were reported previously, but are included for the sake of clarity and continuity. Metal films are important in a wide range of optical coatings and the effects of IAD on the optical properties is therefore of some importance.

From the point of view of optical properties, the results of argon IAD of silver are disappointing. The real part of the refractive index rises and the imaginary part falls. This measurement required great precision to be certain of the consistency of the small shifts observed in the constants. Some wide-spectral-range ellipsometry was performed for this Task by Professor Vedam's group at Pennsylvania State University, but the variation of optical constants is small and so a more sensitive technique for a single wavelength, involving the measurement of a surface plasmon resonance, has also been employed. The results show a clear increase in the real part of the refractive index and a reduction in the imaginary part, both of which correlate well with the rate of momentum transferred to the growing film. DC resistivity increases with bombardment, and a change in lattice constant occurs that is consistent with a shift from tensile stress to compressive stress with increasing bombardment. Rutherford backscattering (RBS) shows implanted argon increasing linearly with the bombarding momentum transfer rate. The shifts in refractive index and conductivity are consistent with the effects expected from the implanted argon. Aluminum is affected in a similar way, although the optical constant variation is

much less linear and so, for light bombardment, the optical constants are less affected. The work is summarized in the attached Applied Optics submission.

Some of the implications are clear. Silver is a material often used for high-power infrared coatings, usually with some dielectric overcoats to boost reflectance. Ion assistance to improve adhesion and, after Sainty et al.,[1] to increase chemical resistance would seem a very attractive technique. Our findings suggest that the effects of the ion bombardment are not all beneficial and that the reduction in performance must be taken into account. Improved adhesion without the overall reduction in optical performance may be possible if ion assistance is limited to only the very early stages of film deposition. Work is in progress on that aspect, with some encouraging results.

IAD of Dielectrics. The problems of dielectric deposition with ion assistance are quite different. Here the implantation of the bombarding species appears to be quite benign. Experiments involving high-temperature baking of films indicate that even implanted argon is firmly embedded and shows no tendency to evolve. When the ions are reactive (e.g., oxygen or nitrogen), beneficial chemical effects can result.

The fluorides represent a very important class of thin-film materials, with a much wider transmittance region than other materials, and yet their usefulness in thin-film coatings, especially in the infrared, has been limited, especially by their generally high intrinsic tensile stress. The studies of the effects of ion assistance on the properties of the fluorides of the lanthanide series have continued. Ion-assisted deposition is of great benefit in reducing the tensile stress, but it also damages the films by affecting their stoichiometry. This damage causes optical absorption, but the damage can be limited and also can be partially healed, often by incorporation of oxygen. Recent work has centered on the fluoride of samarium (see Fig. 1) and the nature of the vacancies left by the bombardment.

The usefulness of ion-assisted deposition when the bombarding species is a reactive gas was mentioned above. Oxygen has long been used in the optical coating of refractory oxides. A background of oxygen in the coating chamber improves the degree of oxidation of the films and decreases their optical absorption. Bombardment of growing metal films with oxygen ions can result in very good oxide layers. Nitrogen is another compound-forming gas which lacks sufficient reactivity to have been a useful background gas in deposition. The nitrides have, therefore, never been used successfully in classical evaporation processes, although some success has been reported using sputtering. This research has confirmed that nitrogen ion bombardment during deposition is a viable technique for producing nitrides. Recent

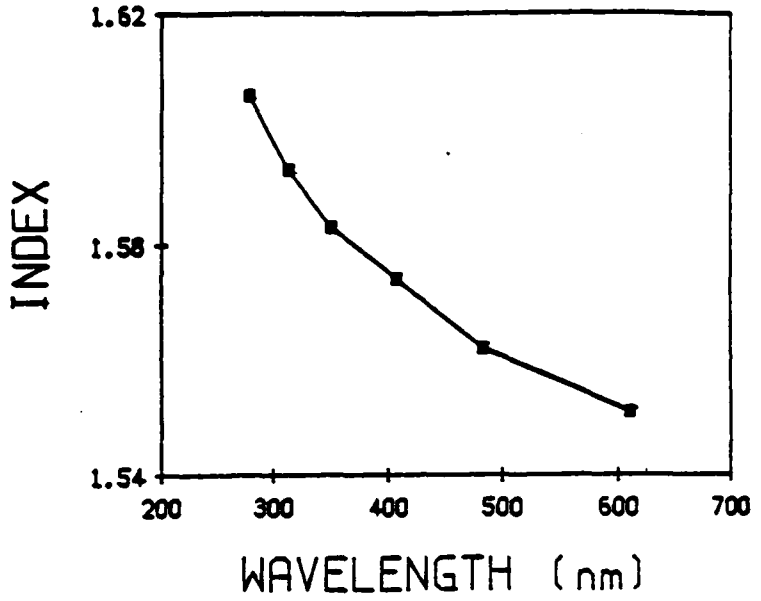


*Figure 1. The measured refractive index of $SmF_3$ in the visible and near UV.*

progress in this area has been in the study of the aluminum-oxygen-nitrogen system. A range of compounds can be produced, with refractive indices from 1.67 (corresponding to pure oxide) to 1.85 (corresponding to the nitride), by evaporating metallic aluminum under various residual atmospheric conditions. The conditions finally chosen for the demonstration, described in the appended manuscript, involve a background gas of oxygen together with nitrogen ion bombardment. This particular arrangement has the benefit of avoiding the corrosive effect of oxygen on the hot cathode of the Kaufman sources, enormously increasing their lifetimes, and also increasing the reactivity of nitrogen so that compounds containing it can be produced. The range of refractive indices as a function of composition is shown both for nitrogen bombardment and bombardment by a nitrogen-oxygen mixture (Figs. 2 and 3). As a test of the process and a demonstration of its potential, a 15-period rugate filter has been constructed. Each period was made up of 10 subperiods so that the entire filter consists of 150 separate layers (Figs. 4 and 5). The variation of properties throughout the entire filter was achieved by varying the background oxygen pressure and keeping the ion-gun conditions and the aluminum evaporation conditions constant. Nitrogen was the bombarding gas. The only variable, therefore, for the complete operation was the background oxygen pressure. The packing density achieved was good because no vacuum-to-air shift was detected. It should be noted that the oxygen partial pressure was manually controlled, which limited the complexity of the coating that could be attempted. More complex and demanding

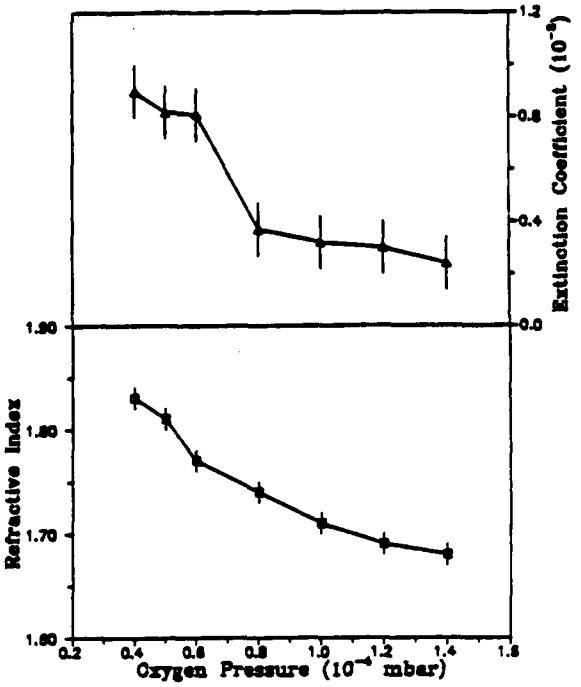


*Figure 2. Variation of refractive index and extinction coefficient of $AlO_xN_y$ thin films at 550 nm. A backfilled oxygen pressure was varied from $0.4\times10^{-4}$ to $1.4\times10^{-4}$ mbar, while a nitrogen ion beam was bombarded on a growing Al film. Ion energy was 1250 eV and current density was 40 $\mu A/cm^2$.*

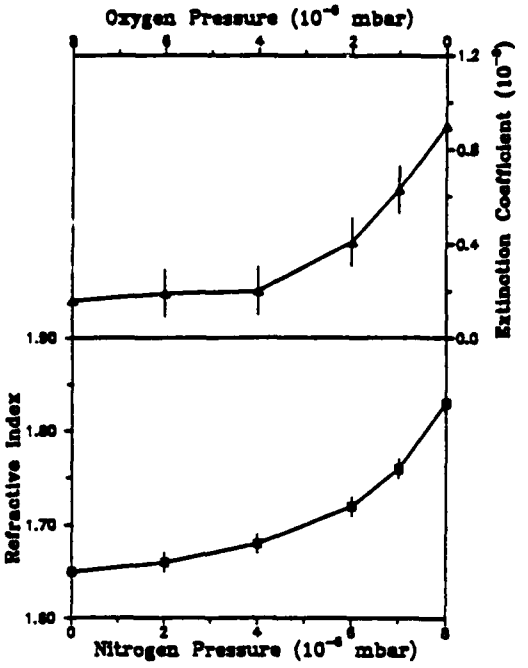


*Figure 3. Variation of refractive index and extinction coefficient of $AlO_xN_y$ thin films at 550 nm. A mixture of nitrogen/oxygen gases was varied $(0/8)\times10^{-5}$ to $(8/0)\times10^{-5}$ mbar. A backfilled oxygen pressure was $1.2\times10^{-4}$ mbar, while the mixed ion beam was bombarded on a growing Al film.*

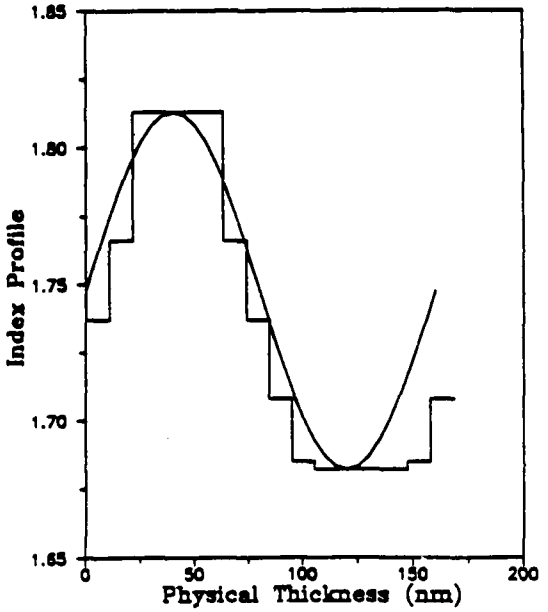


*Figure 4. A step-index profile of $AlO_xN_y$ films obtained from Fig. 1 for a rugate filter. One cycle consists of 10 homogeneous step layers and has a 169 nm physical thickness. A sinusoidal curve is fitted to the step-index profile.*

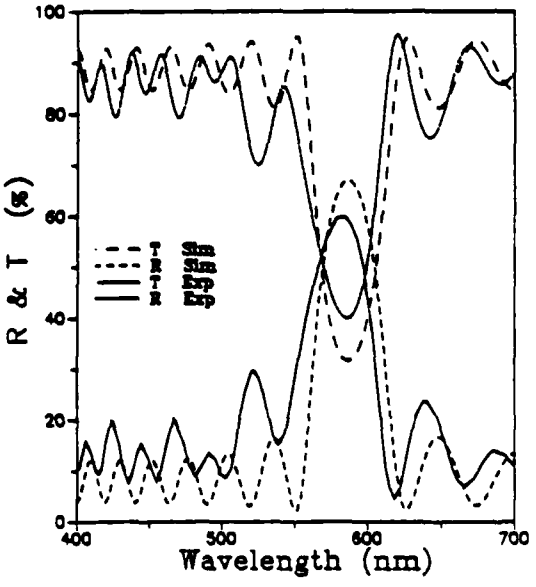


*Figure 5. Reflectance and transmittance of the real and simulated rugate filters. Fifteen cycles were employed.*

coatings may be possible using automatic control techniques. These investigations are now centered on arriving at an understanding of the nature of the aluminum-oxygen-nitrogen material and its properties.

*Modeling*

Thermo-Optical and Nonlinear Effects in Optical Multilayers. The construction of a thermo-optical model began in connection with thermally induced bistability, but the code that has been developed is quite general. It is able to investigate the thermal effects of laser light on the optical properties of optical coatings made of metal or dielectrics. Work on the code has continued under this contract. The code takes into account the electric-field repartition inside the coating to calculate the amount of energy absorbed by the coating. This absorption leads to an increase in temperature, which modifies the refractive indices of the materials involved in the multilayer coating. The coupling of heat-flow equations with optical properties permits the monitoring of the changes in the electric field, the transmittance, and the reflectance during laser irradiation. This simulation has been used to investigate the bistability of laser-irradiated Fabry-Perot etalons made of ZnS or ZnSe.[2] Until that time, the nonlinearity included in the model was only temperature dependent.

A recent paper published in Physical Review Letters[3] triggered interest here in nonlinear effects occurring in structures made of electric-field-dependent nonlinear materials. In the cited work, a multilayer dielectric mirror was subjected to laser irradiation at a wavelength close to its stop band. By allowing the refractive index to vary with the internal electric field, those authors were able to demonstrate the existence of several transmitting states according to the incident power and the degree of nonlinearity.

The existing code used here for thermal simulation was modified to include the nonlinear electric-field dependence of the refractive index, and some very interesting bistability loops have been computed that are in agreement with the referenced paper. This first study demonstrates the possibility of switching a reflecting component to a transmitting state. Rugate filters are mirrors with very narrow stop bands, making them very similar to this example.

An investigation of the consequences of nonlinearities in the refractive indices of the materials involved in a multilayer structure was carried out for the case of a very narrow reflection band mirror. The design chosen for this study is simply a quarterwave stack of formula $(HL)^{200}H$, where H is a quarterwave of material of refractive index 1.51 and L represents a quarterwave of material of refractive index

1.50. The wavelength of investigation was the central wavelength of the stop band of the mirror. This simple design was chosen because the corresponding reflectance properties are close the the properties of a real rugate filter (Fig. 6.)

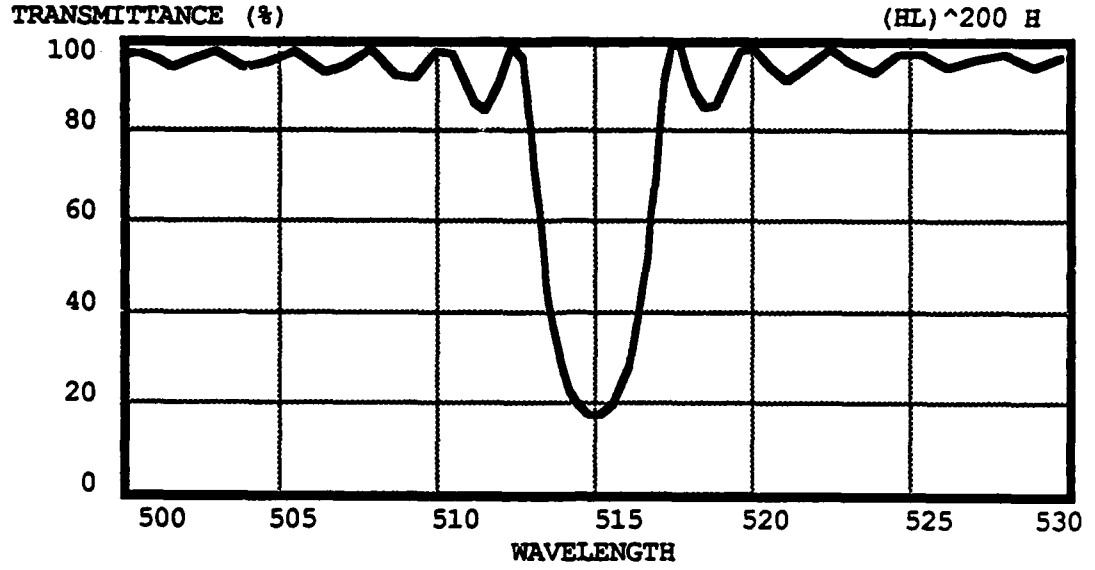


*Figure 6. Transmittance versus wavelength for a $(HL)^{200}H$ mirror.*

In the computations, both materials have an electric-field dependence of the type:

$$\epsilon = \epsilon_0(1 + \lambda_0 E^2) \tag{1}$$

or

$$E = \epsilon_0\left(1 + \frac{\lambda E_n^2}{754}\right) \tag{2}$$

with

$$\lambda = \lambda_0 E_0^2 \, . \tag{3}$$

Equation (2) is used in conjunction with Eq. (3) to integrate both the effect of the nonlinearity of the material and the effect of laser intensity in one parameter.

In these three equations, $\epsilon_0$ is the dielectric permittivity of the material, $\lambda_0$ is the electric-field dependence of the permittivity, E is the electric-field modulus, $E_0$ is the incident electric-field modulus, and $E_n$ is the electric-field modulus normalized to a 1 $W/m^2$ incident power density.

As the power or the nonlinearity is increased, corresponding to an increase in the parameter $\lambda$, the transmittance goes through a hysteresis loop (Fig. 7), allowing the device to become transparent once a threshold value is passed, and to remain transparent as the power is reduced.

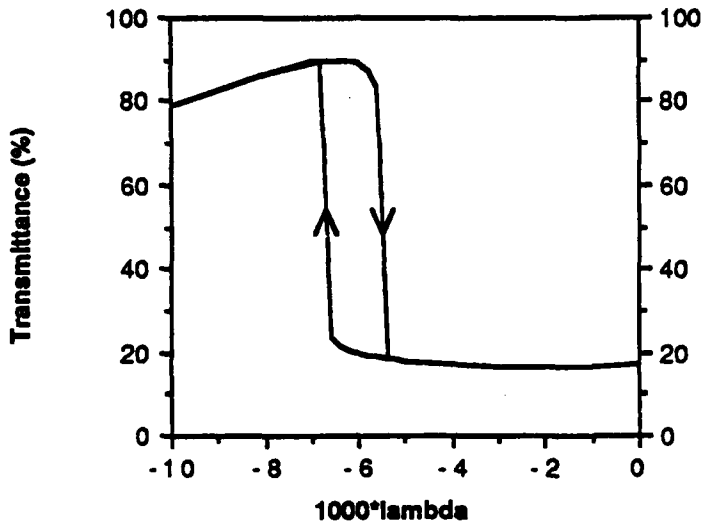


*Figure 7. Bistability of a mirror $(HL)^{200}H$.*

This bistable behavior is very likely to exist in rugate filters if the parameter λ can reach a value higher than the threshold. It is also important to realize that laser irradiation will cause heating by residual absorption and other losses, causing a variation in the refractive index that results from its temperature dependence. Therefore, even if the λ parameter does not reach the threshold value, the influence of the heating may still cause a bistable behavior if the thermal diffusion allows it; this may well be the case in very thick coatings.

It is hoped that this investigation can be pursued by introducing into the code refractive index profiles that are closer to rugate filter designs, to study their behavior under energetic laser fluxes, in terms of both electric-field and temperature effects.

## Personnel

H. A. Macleod
B. G. Bovard
C. K. Hwangbo
M. R. Jacobson
J. Lehan
L. Lingg

## Publications

1. B. G. Bovard and H. A. Macleod, "Nonlinear behavior of optical coatings subjected to intense laser irradiation," J. Mod. Opt. (1988), accepted for publication.

2. J. D. Targove, L. J. Lingg, J. P. Lehan, and H. A. Macleod, "Effect of oxygen incorporation on the structure of ion beam assisted $LaF_3$ thin solid films," Appl. Opt. 27, 213 (1988).

3. J. D. Targove, L. J. Lingg, J. P. Lehan, C. K. Hwangbo, H. A. Macleod, J. A. Leavitt, and L. C. McIntyre, Jr., "Preparation of aluminum nitride and oxynitride thin films by ion assisted deposition," Proc. MRS Symposia 93, 311 (1987).

4. J. D. Targove, L. J. Lingg, J. P. Lehan, and H. A. Macleod, "The effect of oxygen incorporation on the structure of metal fluoride thin films," in *Optical Interference Coatings*, 1988 Technical Digest Series Vol. 6 (Optical Society of America, Washington, D.C., 1988).

5. J. D. Targove, L. J. Lingg, and H. A. Macleod, "Verification of momentum transfer as the dominant densifying mechanism in ion-assisted deposition," in *Optical Interference Coatings*, 1988 Technical Digest Series Vol. 6 (Optical Society of America, Washington, D.C., 1988).

6. C. K. Hwangbo, L. J. Lingg, J. P. Lehan, M. R. Jacobson, and H. A. Macleod, "Ion-assisted deposition of thermally evaporated Ag films," in *Optical Interference Coatings*, 1988 Technical Digest Series Vol. 6 (Optical Society of America, Washington, D.C., 1988).

7. L. J. Lingg, C. K. Hwangbo, B. G. Bovard, J. P. Lehan, and H. A. Macleod, "Effect of ion-assisted deposition on the crystallinity of samarium fluoride films," in *Optical Interference Coatings*, 1988 Technical Digest Series Vol. 6 (Optical Society of America, Washington, D.C., 1988).

8. B. G. Bovard, "Fourier transform technique applied to quarterwave optical coatings," Appl Opt. 27, 3062 (1988).

9. C. K. Hwangbo, L. J. Lingg, J. P. Lehan, H. A. Macleod, and J. L. Makous, "Ion-assisted deposition of thermally evaporated Ag and Al films," submitted to Appl. Opt.

## References


1. W. G. Sainty, R. P. Netterfield, and P. J. Martin, "Protective dielectric coatings produced by ion-assisted deposition," Appl. Opt. 23, 1116 (1984).

2. Bertrand G. Bovard and H. Angus Macleod, "Thermal model of a switching Fabry-Perot etalon," Proc. SPIE 821, 187 (1987).

3. Wei Chen and D. L. Mills, "Gap solitons and the nonlinear optical responses of superlattices," Phys. Rev. Lett. 58, 160 (1987).

Proposal

# IN-SITU STRESS MEASUREMENTS

Principal Investigator: B. G. Bovard

## Introduction

Thin films deposited by thermal evaporation suffer from high levels of stress, which can be tensile or compressive, depending on the materials and the growth process used. For many materials, a high level of stress limits the maximum thickness possible, and is an important cause of mechanical failure.

Stress is usually divided into two components: the intrinsic part, resulting from the growth process itself, and the thermal part, resulting from the differing expansion coefficients of the substrate and film materials.

## Project Goal

Monitoring and controlling stress during deposition are important steps toward understanding the underlying mechanisms that drive stress during film growth. Therefore, we propose to install an in-situ stress monitor in one of our vacuum chambers. The system will be based on the cantilever beam technique, in which the displacement of the end of a thin substrate is measured to calculate the stress.[1]

A number of methods of measuring the displacement are possible (e.g., capacitance measurements). Optical measurement of the displacement using a laser deflection technique is the primary candidate, although other techniques will be considered.

Several materials will then be deposited, including dielectrics such as fluorides, which usually suffer from very high tensile stress, and the process monitored.

## Reference

1. R. W. Hoffman, "Mechanical properties of non-metallic thin films," in *Physics of Non-Metallic Thin Films*, C. H. S. Dupuy and A. Cachard, eds. (Plenum Press, New York, 1974).

TASK 3

## STRUCTURE MODIFICATION BY ION-ASSISTED DEPOSITION (ION BEAM ANALYSIS OF THIN FILMS)

Principal Investigators: J. A. Leavitt and L. C. McIntyre, Jr.

### Project Goals

The goals of this program are threefold: 1) to provide accurate characterization of thin films by MeV ion-beam analysis (IBA) for Thin Film Center scientists and other collaborators; 2) to develop new and improve existing analysis techniques; and 3) to expand the capabilities of the IBA facility itself.

$^4He^+$ analysis ion beams with energies in the 1.5- to 5.0-MeV range from a 6-MV Van de Graaff accelerator are used to determine film thickness, stoichiometry, concentration profiles, and crystalline structure, by means of Rutherford backscattering spectroscopy (RBS), high-energy backscattering, and channeling. A new accelerator source is being developed to depth profile hydrogen in thin films, using $^{15}N^{++}$ analysis beams with energies between 6 and 10 MeV, and utilizing the nuclear reaction $^1H(^{15}N,\alpha\gamma)^{12}C$.

### Summary

During the second year of the project, the IBA facility continued to provide accurate characterization of thin films for Center scientists (215 films analyzed during 11/1/87 to 9/19/88) and other collaborators (239 films analyzed during the same period).

Efforts to improve techniques have included: 1) completion of attempts to use heavier-than-$^4He$ analysis beams to improve mass and depth resolution in backscattering spectrometry; results indicate no major improvements with the heavier beams; 2) the successful depth profiling of P (below the 1% level) in $SiO_2$, using a nuclear-reaction analysis technique involving observation of protons ejected by incident $^4He^{++}$; 3) the acquisition of data to measure non-Rutherford cross sections for $^4He$ incident on light elements (C to Si) in the 1.8- to 5-MeV energy range, so the higher energy beams can be used to reduce the overlap of signals from light elements. Preprints describing all three efforts are available.

Because of unexpected difficulty with extraction of the desired doubly ionized species $N^{++}$ and $He^{++}$, the testing and installation of the new Penning ion source has not proceeded as rapidly as expected. However, usable beams of these species were obtained recently on both 60-Hz and 400-Hz lab test benches; the new source assembly will be installed in the Van de Graaff terminal shortly.

## Work Accomplished

*Film Characterization*

During the period 11/1/87 to 9/19/88, a total of 454 backscattering analyses were provided. Complete analyses (with uncertainties) of the data were reported in most cases; that is, film stoichiometry (< ±1%), thickness in atoms/cm$^2$ (±3%), and impurity profiles were reported. In the majority of analyses, beam energies greater than 3.5 MeV were used to reduce the overlap of signals from different elements;[2,3] frequently, the IBA facility deconvolution programs[5] were applied to separate the remaining overlaps. In particular, for Center scientists, the following analyses were performed:

1) 175 films for the Macleod group. The majority of these films (87) were fluorides of Sm, Gd, Mg, La, Ce, Ca, Lu, Dy, Pr, Tm, and Eu, measured in connection with the use of ion-assisted deposition for modification of film structure.[4,5] Measurements on 37 AlOy and AlOxNy films were provided in a similar study.[6] Other films analyzed were Al (26), Ag (6), TiN/TiW (13), HfOy and SiN (2).

2) Twenty-seven films for the Gibson group. Twelve ZnS films were analyzed for their investigation of atomic layer evaporation deposition; other films analyzed were MgF (6), $ZrO_2$ (5), $TiO_2$ (4).

3) Four Langmuir-Blodgett films for the Stegeman group.

*Technique Improvement*

The following improvements have been undertaken:

1) The investigation into the use of heavier-than-$^4$He analysis beams to improve mass and depth resolution has been completed. The results, with C, N, Ar, and Kr analysis beams, indicate that no major improvements in mass and depth resolution occur with use of these beams,[10] at least, in the analysis beam energy range 1 to 5 MeV.

2) Potassium was successfully depth profiled (below the 1% level) in $SiO_2$, using the nuclear-reaction analysis technique involving observation of ejected protons for an incident $^4$He analysis beam;[11] the method depends on narrow resonances in the

reaction cross section for $^{31}P(^{4}He,p)^{34}S$. This technique was used because the *backscattering* signal from Si overwhelms that from P, so backscattering cannot be used to depth profile P in $SiO_2$.

3) A massive project to measure *non-Rutherford* cross sections for $^{4}He$ incident on light elements (C, N, O, F, Mg, Al, and Si) in the 1.8- to 5.0-MeV energy range has almost been completed. The data from about 500 backscattering runs are being analyzed currently. The He-C data analysis is finished;[12] the result is shown in Fig. 1. This result, and similar results for the elements mentioned above, will allow use of higher energy analysis beams to reduce the overlap of backscattering signals from different light elements. Note that these cross sections *must* be measured; they *cannot* be calculated, as is the case when the cross sections are Rutherford.

*Facility Development*

A new Penning source assembly is being developed for use in the 6-MV Van de Graaff to allow use of the nuclear reaction $^{1}H(^{15}N,\alpha\gamma)^{12}C$ to depth profile hydrogen in thin films. Unfortunately, the isolated resonance in the reaction cross section intended for use occurs for a $^{15}N$ analysis beam energy of 6.35 MeV. Hence, $^{15}N^{++}$ beams must be used to cover the 6 to 9 MeV region necessary to do the depth profiling.

The remainder of the parts (velocity selector and Einzel lens) needed to complete the source assembly were received on 1/19/88. The entire assembly underwent 60-Hz bench tests, and some time was required to extract clean, doubly ionized beams. Eventually it was determined how to tune the assembly for doubly ionized beams. Typical results are shown in Fig. 2; note the presence of usable beams of $N^{++}$ (2.5 $\mu$A) and $He^{++}$ (4.2 $\mu$A).

The support platform has been constructed for insertion of the assembly into the Van de Graaff terminal and 400-Hz bench tests are being run. Results similar to those shown in Fig. 2 have been obtained, except for the presence of an additional beam signal of unknown origin.

The unexpected difficulty with extraction of the doubly ionized beams has caused the testing and installation of the new source to fall behind schedule; however, the new source assembly is expected to be in the terminal shortly.

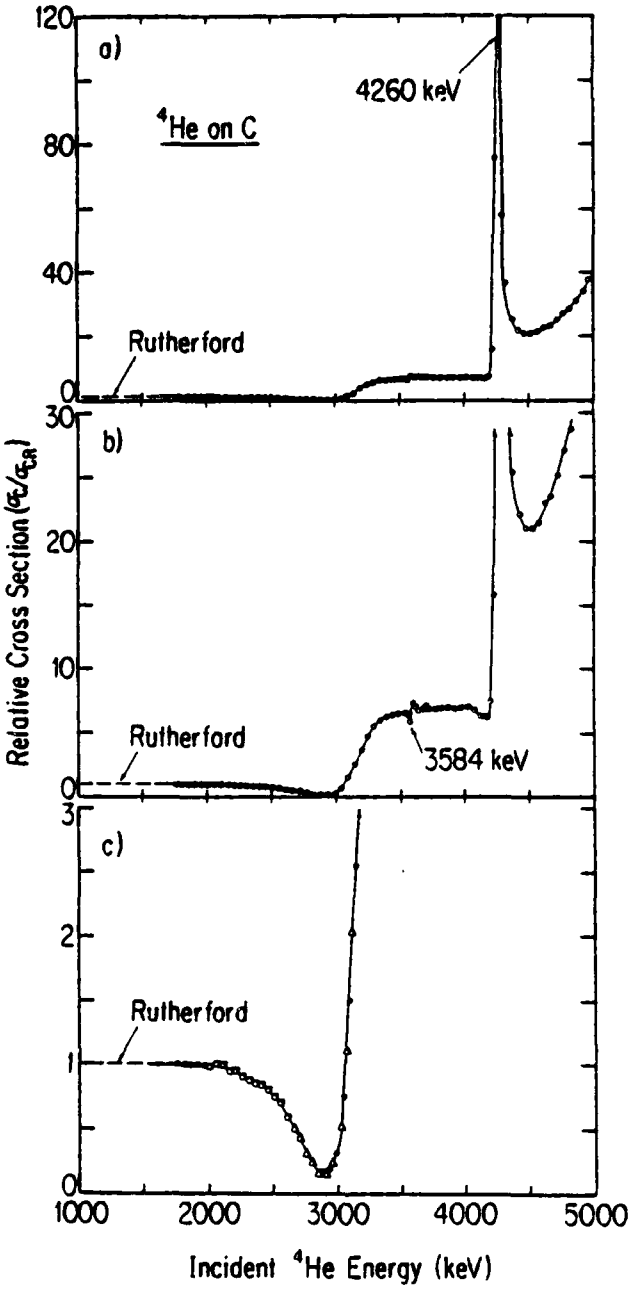


*Figure 1. Measured relative cross sections for 170° backscattering of $^4He^{++}$ ions by carbon nuclei for $^4He^{++}$ incident at energies between 1.5 and 5.0 MeV; for relative cross sections equal to 1.00, the scattering is Rutherford; that is, Coulomb's law holds. These cross sections are non-Rutherford for $^4$He energies above 2 MeV; previous measuurements of $^4$He-C scattering in this energy range are not suitable for use with the backscattering technique. The strong non-Rutherford resonance at 4260 keV is particularly useful for enhancing the sensitivity for depth profiling carbon in heavy-element thin films.*

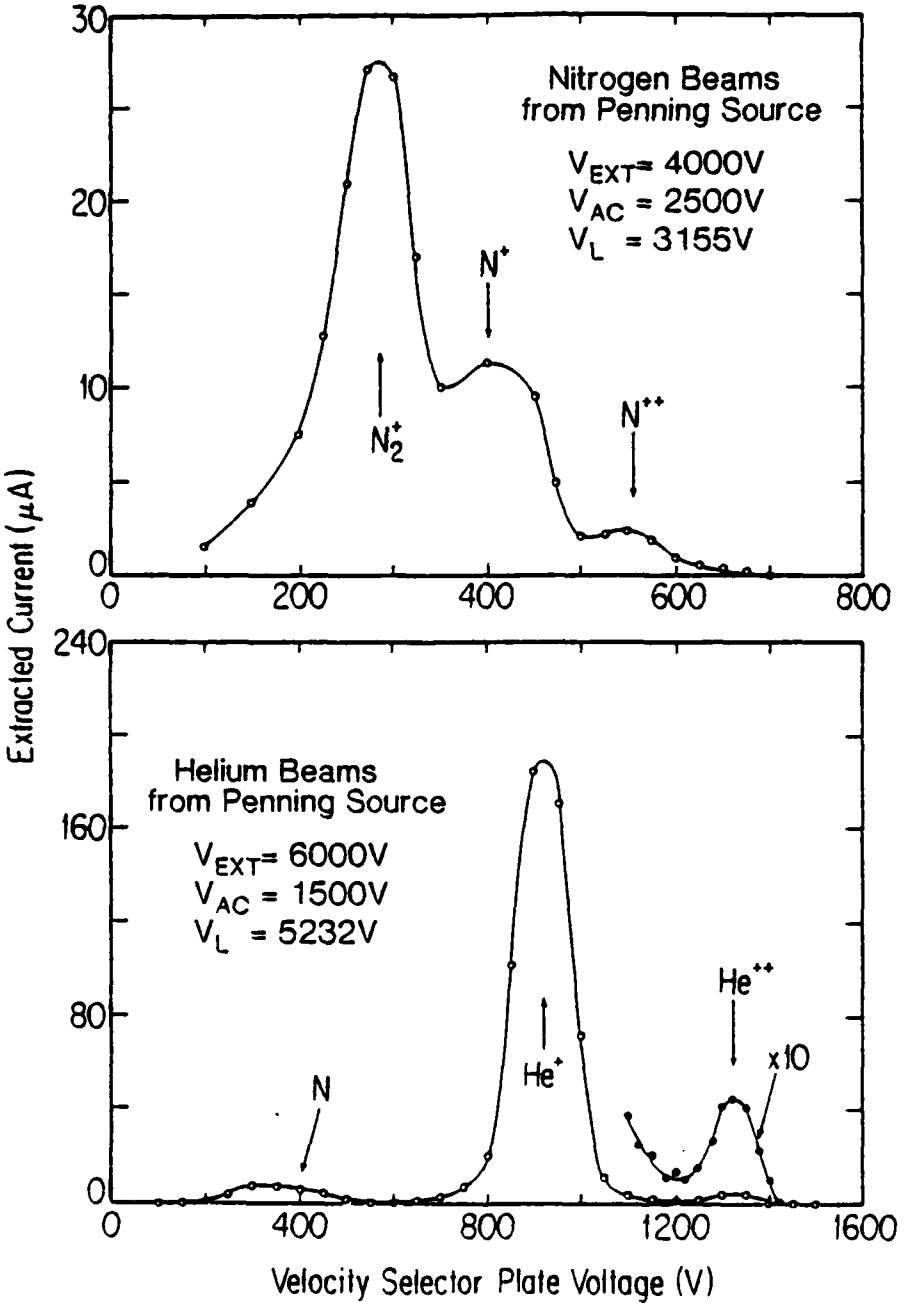


*Figure 2. Ion beams of nitrogen and helium from the new Penning source assembly obtained during bench tests of this source. Note the presence of doubly charged beams: 2.5 μA of $N^{++}$ and 4.2 μA of $He^{++}$. Successful operation of this source in the 6 MV Van de Graaff terminal will provide $He^{++}$ analysis beams for backscattering measurements with energies of at least 10 MeV, and will allow depth profiling of hydrogen in thin films using the nuclear reaction $^1H(^{15}N,\alpha\gamma)^{12}C$.*

*Ion Beam Analysis Seminar*

A 10-hour, no-credit, no-grade seminar on MeV IBA techniques was taught by J. A. Leavitt during the spring semester of 1988. The purpose of the seminar was to teach collaborators how to analyze the backscattering data produced by this group. Seminar attendees were from the UA Departments of Physics, Chemistry, Materials Science, Electrical Engineering, and Optical Sciences, as well as from local industry (IBM). Initial attendance was 28 persons; this dropped to 21 by the end of the seminar.

## Plans

Plans for the next year include: 1) continuing to provide thin film characterization for collaborators; 2) completing the 400-Hz Penning assembly bench test and installing the source assembly in the accelerator; testing the source and making any necessary alterations; depth profiling hydrogen in a test sample (TiH); and commencing routine analysis of H in thin films; 3) analyzing the non-Rutherford cross-section data for He on N, O, F, Mg, Al, and Si in the 1.8- to 5.0-MeV energy region and publish the results; measuring non-Rutherford cross sections for He on light elements in the 5- to 10-MeV energy region.

## Personnel

J. A. Leavitt
L. C. McIntyre, Jr.
P. Stoss (partially supported through Characterization Facility)
M. D. Ashbaugh (10/1/87-4/1/88)
J. G. Oder (4/1/88-present)

## Collaborations

Macleod group (UA Optical Sciences): ion-assisted modification of film structure, fluorides and oxynitrides.
Gibson group (UA Optical Sciences): atomic layer deposition of ZnS.
Stegeman group (UA Optical Sciences): Langmuir-Blodgett films.
Falco group (UA Physics): high $T_c$ superconducting films; MBE superlattices.

## References


1. J. A. Leavitt, "Ion beam analysis with a 6 MV Van de Graaff," Nucl. Instrum. Meth. B 24/25, 717 (1987).

2. J. A. Leavitt, L. C. McIntyre, Jr., M. D. Ashbaugh, B. Dezfouly-Arjomandy, and J. G. Oder, "Characterization of optical coatings with backscattering spectrometry," in *Optical Interference Coatings*, 1988 Technical Digest Series, Vol. 6 (Optical Society of America, Washington, D.C., 1988).

3. L. C. McIntyre, Jr., M. D. Ashbaugh, and J. A. Leavitt, "Limits on the accuracy of stoichiometry determined by Rutherford backscattering using computer peak fitting," Proc. MRS Symposia 93, 401 (1987).

4. J. D. Targrove, M. J. Messerly, J. P. Lehan, C. C. Weng, R. H. Potoff, H. A. Macleod, L. C. McIntyre, Jr., and J. A. Leavitt, "Ion-assisted deposition of fluorides," Proc. SPIE 678, 115 (1986).

5. J. D. Targove, J. P. Lehan, L. J. Lingg, H. A. Macleod, J. A. Leavitt, and L. C. McIntyre, Jr., "The ion-assisted deposition of lanthanum fluoride thin films," Appl. Opt. 26, 3733 (1987).

6. J. D. Targove, L. J. Lingg, B. G. Bovard, J. P. Lehan, H. A. Macleod, J. A. Leavitt, and L. C. McIntyre, Jr., "Preparation of aluminum nitride and oxynitride thin films by ion-assisted deposition," Proc. MRS Symposia 93, 311 (1987).

7. J. L. Makous, J. A. Leavitt, L. C. McIntyre, Jr., L. Maritato, R. Vaglio, A. M. Cucolo, and C. M. Falco, "Superconducting superlattice structures," Proc. MRS Symposia, Boston, MA, Nov. 30-Dec. 4, 1987.

8. J. A. Leavitt and L. C. McIntytre, "MeV ion beam analysis of high $T_c$ superconducting films," submitted to Nucl. Instrum. Meth. B - preprint available.

9. J. P. Cronin, T. J. Gudgel, L. Zanotto, B. Dutta, G. P. Rajendran, G. Dale, E. D. Zanotto, E. V. Uhlmann, J. A. Leavitt, and J. R. Martin, "Wet chemistry-derived barrier layers for ceramic superconductor films," Proc. Amer. Ceramics Soc. (in press) - preprint available.

10. J. A. Leavitt, L. C. McIntyre, Jr., P. Stoss, M. D. Ashbaugh, B. Dezfouly-Arjomandy, M. F. Hinedi, and G. Van Zijll, "Backscattering spectrometry with $^{4}He$, $^{12}C$, $^{14}N$, $^{40}Ar$, and $^{84}Kr$ analysis beams with energies 1.5 to 5.0 MeV," Nucl. Instrum. Meth. B (in press) - preprint available.

11. L. C. McIntyer, Jr., J. A. Leavitt, B. Dezfouly-Arjomandy, and J. Oder, "Depth profiling of phosphorus using resonances in the $^{31}P(\alpha,p)^{34}S$ reaction," Nucl. Instrum. Meth. B (in press) - preprint available.

12. J. A. Leavitt, L. C. McIntyre, Jr., J. G. Oder, P. Stoss, M. D. Ashbaugh, B. Dezfouly-Arjomandy, Z. Lin, and Z.-M. Yang, "Cross sections for 170° backscattering of $^{4}He$ from carbon for $^{4}He$ energies between 1.8 and 5.0 MeV," submitted to Nucl. Instrum. Meth. B - preprint available.

TASK 4

# A NOVEL TECHNIQUE FOR QUANTIFYING THE MECHANICAL PROPERTIES OF THIN FILMS

Principal Investigators: G. I. Stegeman and C. T. Seaton

## Project Goals

The principal objective of this project is to develop Brillouin scattering as a technique for measuring the elastic properties of interesting thin films and interfaces. A secondary objective is to use second harmonic generation (SHG) as a tool for studying thin films. The actual work performed can be subdivided into these two areas:

a) elastic properties of films and their modification;

b) SHG of thin films.

The SHG work was primarily was supported by other sources.

## Work Accomplished

Work with previous collaborators inside and outside URIP was continued. With U. Gibson, the Brillouin spectra of very rough ZnS films were examined and second harmonic generation measured on specially prepared ZnS films. Finally, study of polymerized Langmuir-Blodgett films with J. Swalen of IBM Almaden was successfully concluded.

In addition, two visitors had a large impact on this research, presenting some new opportunites, specifically in the area of Langmuir-Blodgett (L-B) films. These films are fabricated one monolayer at a time in a Langmuir trough, and their range of applications in electronics and optics is increasing dramatically. David Gleed, a graduate student from the University of Exeter, brought a series of L-B films fabricated at Exeter for investigation by Brillouin scattering. Professor Wolfgang Knoll visited for three months, made the L-B trough here operational again, and produced films which were investigated both by Brillouin scattering and SHG.

The program has lost one of its key personnel, namely Dr. B. Hillebrands, who returned to Germany to finish his Habilitation in July. Fortunately, a highly qualified postdoctoral replacement was found, namely John Dutcher from the

University of British Columbia, who was selected from more than fifty applicants. He is expected to arrive about October 15.

*Brillouin Scattering From Rough Surfaces*

Three series of experiments were performed that probed the elastic properties of imperfect surfaces.

ZnS films were deposited by the Gibson group for roughness studies; the Rayleigh wave penetrates less than 1000 Å into the material, and normally has its maximum amplitude right at the surface, hence it is very susceptible to surface quality. In fact, it was found experimentally that the presence of a Rayleigh wave could not be detected by light scattering in a sample with microcracks, indicating this mode to be very heavily damped by the very rough film surface. However, Brillouin scattering was detected from Sezawa modes, which fill the complete volume of the film and thus are less heavily damped by a rough surface. This work will continue to quantify the effects.

The first step in understanding how a "rough" surface affects the acoustic phonon spectrum, and hence the mechanical properties, is to investigate the simplest possible case of a rough surface, namely a periodically corrugated surface. Gratings with periodicites varying from 0.2 to 0.5 $\mu$m were etched into the (001) surface of silicon. Spectra obtained from small-corrugation gratings show evidence for the existence of two Rayleigh modes, one corresponding to that of a flat surface, and the other frequency-renormalized by the presence of the grating. The existence of two modes is not yet understood. Also observed was zone folding at a wavevector corresponding to the grating periodicity, as well as a longitudinal resonance at the zone boundary. The results for deep gratings show strongly frequency-renormalized modes and a large dispersion gap at the zone boundary. Since all of the observed features are not understood, this work will continue.

The last report discussed preliminary Brillouin scattering investigations of the elastic properties of saturated ODF, and unpolymerized and polymerized $\omega$-ODF and ODF:ODM Langmuir-Blodgett films. Because of the laminar film structure, which consists of parallel long molecules, aligned perpendicularly to the interface and tightly bonded to each other, the films are highly anisotropic elastically and generally show an unusual small value of the transverse sound velocity; i.e., $c_{44}$. The elastic constants decreased on polymerization for all of the films except DOF:ODM, which exhibited a small stiffening of $c_{44}$, contrary to widely held opinions in the L-B community. Subsequent electron microscope examinations of the films showed that most of the films showed microcracks which occurred during the polymerization

process. This correlates with the large reductions, as much as 40%, in the measured elastic constants. For the ODF:ODM system, there is negligible film contraction on polymerization, no significant microcrack formation occurs, and the elastic constants do increase on polymerization. These results, which corroborate the ZnS measurements discussed above, show that Brillouin scattering can definitely be used to detect microcrack formation.

*Buffer Layer Effects Measured by Brillouin Scattering*

Brillouin scattering measurements were performed on three different samples of ZnS films on Si substrates to study possible effects of different buffer layers between the substrate and film created by different substrate cleaning procedures.

The three samples used in this project were grown by physical vapor deposition after the Si substrate was cleaned by three different methods. Sample 1 was cleaned by the standard substrate-cleaning procedure with deionized water and a detergent, followed by ion milling for one minute. This sample served as a reference, since it did not have a buffer layer even though its surface may have been damaged by the ion milling. Sample 2 was cleaned by the standard cleaning procedure, but without the ion milling. This one may have a $SiO_2$ buffer layer between the substrate and the film. Sample 3 has been contaminated by pump oil and therefore probably has a thin pump-oil buffer layer. The thicknesses of the ZnS films were 310 Å, 230 Å and 80 Å respectively, as measured with a WYKO Non-Contact Profiler.

The phonon dispersion curves were calculated for both an isotropic ZnS film on a Si substrate, and for an isotropic ZnS film separated from the Si substrate by an isotropic $SiO_2$ film, to search theoretically for any modification resulting from the buffer layer. The calculated curves do not show any changes within the resolution of the Brillouin spectroscopy technique. This was confirmed by the experimental data. Therefore, except for the data from Sample 3, which needs more analysis, no effect was observed on the acoustic phonon spectrum of different cleaning procedures causing a possible buffer layer between the film and the substrate. This result confirmed theory, which predicted no modification of the dispersion curves.

*Brillouin Scattering From Langmuir-Blodgett Films*

Two additional sets of experiments were performed on Langmuir-Blodgett films with the assistance of the visitors. One of the questions addressed was whether the elastic properties of L-B films depend on the conditions of the water surface in the Langmuir trough. A number of films of 22-tricosenoic acid were prepared with increasing water surface pressures, and the Brillouin spectra then were measured.

(22-tricosenoic acid is being developed as a high-resolution photoresist material.) It was found that both the Rayleigh wave and first Sezawa mode velocities increased with increasing surface pressure, indicating a corresponding increase in the shear elastic constant. Differences in the Brillouin spectra were also observed for phonon wavevectors parallel (versus perpendicular) to the film "pulling" direction, revealing in-plane asymmetry in the elastic constants. A detailed analysis of the data for one surface pressure yielded the film elastic constants. Although the values of the longitudinal elastic constants $c_{11}$ and $c_{33}$ were about 60% of the values found previously for CdA, the shear constant $c_{55}$ was about 2.5 times larger. Therefore, although 22-tricosenoic acid has a small $c_{55}/c_{11}$ ratio ($c_{55}/c_{33}$ also) of approximately 1:10, it is not as anomolously small as CdA, which was between 1:20 and 1:40.

A second set of experiments was carried out on films made from GD10 L-B molecules. From symmetries in the Brillouin spectra, it was concluded that the films were indeed hexagonal in structure. In contrast to other L-B films, the c-axis lies in the plane of the film, with the long molecular axis aligned along the dipping direction. By using Brillouin spectroscopy to probe the phonon modes in the a-c and a-b planes, and to identify spectra attributable to longitudinal guided waves, the *complete* set of elastic constants was determined for an L-B film for the first time. As noted for 22-tricosenoic acid, the ratio of the shear to the longitudinal elastic constants was approximately 1:10.

*Surface-Enhanced Brillouin Scattering From Metal Films*

The Brillouin scattered signals from metal surfaces are usually very weak, and hours typically are required to accumulate a spectrum with a good signal-to-noise ratio. By coupling the incident light to surface plasmons, the electromagnetic field at the surface can be enhanced, leading to stronger signals. Further, if the Brillouin scattered light is taken out in the form of surface plasmons, the scattering cross section is enhanced further.

A silver film 500 Å thick was deposited onto the base of a glass prism. The incident light was coupled into a surface plasmon mode (as evidenced by a decrease in the reflected light). The light backscattered into a surface plasmon mode was outcoupled using the same prism and analysed with a tandem interferometer. When the direction of the incident light was angle tuned through the surface plasmon resonance, the Brillouin signals for scattering from the Rayleigh wave and the first Sezawa mode were enhanced by a factor of 350 over the off-resonance case. The observed enhancement versus angle was in excellent agreement with theory.

*Second Harmonic Generation From Thin Films*

This is the first year that URIP has provided some nominal support for this program. In the past SHG has been shown to be a very powerful probe of the anisotropy of thin films.

The anisotropy of ZnS films deposited under varying conditions was probed using SHG. The results are discussed under Task 1 report.

With the aid of Wolfgang Knoll, a new and very powerful application of SHG to monolayer films deposited by the Langmuir-Blodgett technique was demonstrated. Previous SHG studies have derived information about molecular hyper-polarizabilities or orientational properties of single molecules or parts of molecules. It was shown that structural information is also available at the supra-molecular level of single crystallites containing many molecules.

When the cyanine dye S120 is spread and compressed on the water surface of a Langmuir trough, crystalline aggregates (called J or Scheibe aggregates) are formed for pressures above a certain critical pressure. It is generally believed that the aggregates are randomly distributed on the water surface, and that this random distribution is transferred to the substrate. By performing SHG from such a deposited monolayer and rotating the sample about the incident laser beam, it was shown that the symmetry of the aggregates is $C_2$, and that for certain deposition conditions, the aggregates are *not* randomly distributed on the surface. In fact, it was shown that the results depend on the net molecular flow velocity in the region of the trough when the barriers are moved to compensate for loss of material when a monolayer is being deposited. When a tank designed for zero velocity at the deposition point is used, there is well-defined net orientation for the crystallites. On the other hand, when the deposition is performed under conditions in which there is a net flow velocity for the molecules, the orientations of the crystallites, which individually still have $C_2$ symmetry, are random.

**Plans**

Use of Brillouin scattering to quantify and interpret the elastic properties of thin films will continue. In particular, investigation will continue into:

1. the fascinating elastic properties of L-B films;

2. the effects of roughness on surface mechanical properties, including grating structures;

3. the elastic properties of films fabricated by different techniques.

Some new directions are expected that will incorporate the ideas and interests of the new postdoctoral fellow.

In the area of SHG from films, there are many interesting possible experiments, as is typical during the evolution of a new technique. These will be pursued as they become apparent. Study of the properties of thin film deposited under different conditions in order to optimize film properties and study of L-B films will continue.

## Collaborations

U. J. Gibson (UA): adhesion properties of thin films

C. M. Falco (UA): preparation of superlattice samples

J. Swalen (IBM San Jose): preparation of Langmuir-Blodgett films

J. R. Sambles (University of Exeter): preparation of Langmuir-Blodgett films

W. Knoll (Max Planck Mainz): preparation of Langmuir-Blodgett films

## References


1. S. Lee, B. Hillebrands, G. I. Stegeman, H. Cheng, J. E. Potts, and F. Nizzoli, "Elastic properties of epitaxial ZnSe (001) films on GaAs measured by Brillouin spectroscopy," J. Appl. Phys. 63, 1914 (1988).*

2. B. Hillebrands, S. Lee, G. I. Stegeman, H. Cheng, J. E. Potts, and F. Nizzoli, "Observation of a guided longitudinal acoustic phonon in epitaxial ZnSe films on GaAs," Phys. Rev. Lett. 60, 832 (1988).*

3. J. A. Bell, W. R. Bennett, R. Zanoni, G. I. Stegeman, C. M. Falco, and C. T. Seaton, "Brillouin scattering from Love waves in Cu/Nb metallic superlattices," Appl. Phys. Lett. 51, 652 (1987).*

4. J. A. Bell, W. R. Bennett, R. Zanoni, G. I. Stegeman, C. M. Falco, and C. T. Seaton, "Elastic constants of, and Stonely waves in, molybdenum films measured by Brillouin scattering," Appl. Phys. Lett. 52, 610 (1988).*

5. J. A. Bell, W. R. Bennett, R. Zanoni, G. I. Stegeman, C. M. Falco, and C. T. Seaton, "Elastic constants of Cu/Nb superlattices," Solid State Comm. 64, 1339 (1988).*

6. P. Baumgart, B. Hillebrands, R. Mock, G. Güntherodt, A. Boufelfel, and C. M. Falco, Phys. Rev. B 34, 9004 (1986).*

7. B. Hillebrands, P. Baumgart, and G. Güntherodt, Phys. Rev. B 36, 2450 (1987).*

8. B. Hillebrands, A. Boufelfel, C. M. Falco, P. Baumgart, G. Güntherodt, E. Zirngiebl, and J. D. Thompson, J. Appl. Phys. 63, 3880 (1988).*

9. C. M. Falco, J. L. Makous, J. A. Bell, W. R. Bennett, R. Zanoni, G. I. Stegeman, and C. T. Seaton, "Competing interactions in metallic superlattices," in *Proceedings of CMS Workshop*, R. LeSar, A. Bishop, and R. Heffner, eds. (Springer-Verlag, Berlin, 1988).

10. A. Boufelfel, B. Hillebrands, G. I. Stegeman, and C. M. Falco, "Fe/Pd second-order superlattices," submitted to Solid State Commun.

11. S. Lee, B. Hillebrands, G. I. Stegeman, L. A. Laxhuber, and J. D. Swalen, "Elastic properties of unpolymerized and polymerized ODF and ODM Langmuir-Blodgett films determined by Brillouin scattering," submitted to J. Chem. Phys.

12. D. G. Gleed, B. Hillebrands, S. Lee, G. I. Stegeman, and J. R. Sambles, "The angular dependence of surface-enhanced Brillouin scattering from silver (double resonance effect)," submitted to Solid State Commun.

13. D. G. Gleed, B. Hillebrands, S. Lee, G. I. Stegeman, J. R. Sambles, and N. J. Geddes, "Brillouin spectra from Langmuir-Blodgett films of 22-tricosenoic acid," submitted to J. Phys. C: Solid State Phys.

14. F. Nizzoli, S. Lee, W. Knoll, and G. I. Stegeman, "Determination of the whole set of elastic constants of a Langmuir-Blodgett film by Brillouin spectroscopy," submitted to Phys. Rev. B.

15. V. Mizrahi, G. I. Stegeman, and W. Knoll, "Anisotropic orientation distribution in polycrystalline Langmuir-Blodgett monolayers as revealed by second harmonic generation," submitted to Phys. Rev. Lett.

16. V. Mizrahi, G. I. Stegeman, and W. Knoll, "Microstructure of J-band forming cyanine dye monolayer probed by second harmonic generation," submitted to Phys. Rev. B.

17. V. Mizrahi, G. I. Stegeman, and W. Knoll, "Second-harmonic generation as a probe of thin film and monolayer microstructure," in Proceedings of Trends in Quantum Electronics '88, in press.

* - referred to in the previous report

TASK 5

## A CONTINUUM MODEL FOR THE MORPHOLOGY OF THIN FILMS

Principal Investigator: Seth Lichter

### Project Goal

While some features of film morphology are correlated to substrate temperature by the structure zone model of Movchan and Demchishin, the ability to predict film properties (such as film density, rate of growth, and column size) from deposition conditions is an actively pursued goal for both its theoretical interest and practical importance. The purpose of this research is to analyze how deposition parameters affect film morphology. This is done by first identifying the physical mechanisms which control adatom motion on the film. Then, a mathematical model including these effects is formulated.

### Work Accomplished

To date, the work accomplished may be summarized as follows: 1) the equations describing the evolution of a growing film have been formulated, and 2) the behavior of the equations in some limiting cases has been determined. A more extensive description of how the film responds under a variety of deposition conditions is forthcoming, pending completion of the numerical coding necessary to determine some of the parameters which appear in the equations. These results will be available in a preprint later this month.

The large-scale properties of a thin film are obtained by averaging over an ensemble of individual particles passing through a control volume on the surface. The local analysis is performed in a coordinate-independent fashion. The local balance then yields deposition equations in general coordinates that have the advantage of being fully nonlinear for the macroscopic scales. A simple ballistic argument yields a scattering cross section that determines the number of adatoms added to the surface layer and their velocity along the surface.

The basic assumption is that the incident adatoms hit the substrate and a portion of them join a loosely bound surface layer. The adatoms in this surface layer then eventually stick, leading to accretion of the deposited film.

The formulation incorporates the effects of incoming momentum, adatom motion, including convection and diffusion, and sticking. The incoming beam is assumed to be unidirectional and uniform. The flux rate onto a particular portion of the surface is then dependent upon the orientation of the surface. Incident particles will hit the surface and many will re-evaporate. A simple ballistic argument determines the portion of the beam flux which is not re-evaporated. Adatoms move by convection and surface diffusion until they stick. Bulk diffusion is ignored. Finally, it is assumed that adherence to the surface is a Poisson process and that, consequently, the deposition rate is proportional to the adatom concentration.

Consider a control volume on the surface whose location is given by $\vec{p}$. In the control volume, the concentration of adatoms, c, will be augmented by a portion of the incoming flux through the top control surface. On the lower control surface, a certain proportion of the adatoms, $\alpha$, stick per unit time. Adatoms also leave through the sides of the control volume because of their non-zero velocity.

A particle that is deflected along the surface will travel with a fixed velocity, V, until it strikes some other particle. It is assumed that the probability of the particle being deflected a second time is a Poisson process with time scale $1/\gamma$. The average length of a deflection is then given by $V/\gamma$. It is assumed that both of these scales are small compared to the characteristic scales of the surface; that is,

$$\frac{1}{\gamma} \, , \, \frac{V}{\gamma} \ll 1 \, . \tag{1}$$

The density of coherent adatoms, c, can now be written in terms of the ballistic cross section by integrating the contributions from the incident flux in the neighborhood of a particular point, $\vec{p}$, on the surface,

$$c(\vec{p}, t) = \int_0^{2\pi} d\psi \int_0^{\infty} dr \, \frac{1}{V} \, J_{\psi}(\vec{p} - r\hat{\psi}, t - t')e^{-\gamma t'} \, , \tag{2}$$

where the local polar coordinates $(r, \psi)$ have been introduced on the surface. The flux $J_{\psi}$ has to be normalized by the velocity V to give a particle density per unit length. The exponential term is the probability density that a particle remains undeflected after a time t', where t' is the transit time from the location where the particle strikes $\vec{p} - r\hat{\psi}$ to the location $\vec{p}$, or

$$t' = \frac{r}{V} \, . \tag{3}$$

The integral Eq. (2) can be simplified:

$$c(\vec{p}, t) = \frac{1}{\gamma} J_n - \frac{1}{\gamma^2} (J_n)_t - \frac{1}{\gamma^2} \nabla_s \cdot \left[ \vec{V}_a J_n \right] . \tag{4}$$

Two local properties of the ballistic cross section are defined here; first, the total incident flux, $J_n$:

$$J_n = \int_0^{2\pi} J_\psi d\psi , \tag{5}$$

and second, the average velocity of an incident particle:

$$\vec{V}_a = V \frac{\int_0^{2\pi} d\psi J_\psi \hat{\psi}}{J_n} . \tag{6}$$

The subscript s on the vector operators indicates that they are acting along the surface defined by $\vec{p}$. Using the condition in Eq. (1), it is clear that the leading-order solution to the concentration is

$$c(\vec{p}, t) = \frac{1}{\gamma} J_n , \tag{7}$$

which can be interpreted physically as the incident flux multiplied by the average time to deflection of an adatom. The first-order corrections to Eq. (7) can now be written in terms of c instead of $J_n$:

$$c = \frac{1}{\gamma} J_n - \frac{1}{\gamma} c_t - \frac{1}{\gamma} \nabla \cdot \left[ \vec{V}_a c \right] , \tag{8}$$

where the last two terms in Eq. (8) are the leading-order corrections for the temporal fluctuation and the mean advection of adatom concentration.

Equation (8) describes the evolution of c attributable to the coherent motion of particles caused by ballistic scattering. In addition to this motion, a contribution from the motion of the particles caused by random scattering on the surface can be included. It is assumed that if a particle in the surface layer is deflected, the orientation of its velocity will be determined randomly. Consequently, the motion of the particle can be modeled as a diffusive process.

The rate at which particles leave the coherent adatom concentration is given by $\gamma c$. It is assumed that adatoms become part of an incoherent adatom density, d. Adatoms are removed from the incoherent state by sticking to the surface; this is again assumed to be a Poisson process with a mean lifetime of $q/\gamma'$. The equation of motion for d is then given by

$$d_t = \gamma c - \gamma' d + \nu \nabla_s^2 d \ , \tag{9}$$

where $\nu$ is a diffusion constant which can be thought of as the product of the mean speed and the mean free path.

As adatoms are deposited, the surface grows outward along its normal in proportion to the rate of deposition; that is,

$$\vec{p}_t = \gamma' d \hat{n} \ . \tag{10}$$

This equation, together with Eqs. (8) and (9), specifies the evolution of the surface. To summarize, the equations governing the growth of the interface are

$$c_t = J_n - \gamma c - \nabla_s \cdot \left[ \vec{V}_a c \right] ,$$

$$d_t = \gamma c - \gamma' d + \nu \nabla_s^2 d \ ,$$

$$\vec{p}_t = \gamma' d \hat{n} \ ,$$

where

- $\vec{p}$ = location of the surface,
- $\hat{n}$ = surface normal,
- c = coherent adatom volume density,
- d = incoherent adatom volume density,
- $J_n$ = adsorbed adatom flux,
- $\vec{V}_a$ = average adsorbed adatom velocity,
- $1/\gamma$ = coherent adatom deflection rate,
- $1/\gamma'$ = incoherent adatom sticking rate,
- $\nu$ = incoherent adatom diffusion.

Results from the above formulation will be contained in the attached preprint of an article to be submitted to Physical Review B.

Checking some of the more refined results of the model with experiments being performed by J. Ruffner and U. Gibson in the Optical Sciences Center was intended,

but there was not sufficient time. However, in the preprint, the results are compared with previous experimental data.

**Personnel**

S. Lichter

**Collaboration**

A. J. Bernoff, Department of Mathematics, University of Arizona

U. J. Gibson: Experimental confirmation of model results

TASK 6

# STUDIES OF SURFACE ROUGHNESS HEALING

Principal Investigator: C. M. Falco

## Project Goal

The goal of this task is to develop techniques for determining, and reducing, the roughness of substrate surfaces. Scanning tunneling microscopy (STM) and optical interferometry techniques will be developed to study the roughness of surfaces on length scales ranging from angstroms to millimeters. In combination with these studies, sputtering and molecular beam epitaxy (MBE) techniques will be developed to deposit "buffer layers" to reduce the roughness.

## Summary

The roughness at the interfaces within multilayer coatings has a negative effect on most of the desirable physical properties of such coatings. Multilayers currently being produced for some purposes have layer thicknesses on the order of 1 nm or less. In such structures, even sub-nanometer roughness can have a large effect. As a result, it has become a fairly common practice to pre-deposit an initial thick layer of some material on a substrate in hope of healing the roughness, before beginning deposition of the actual thin film. However, systematic studies of the effects of these "buffer layers" have yet to be conducted. Of great interest is understanding of the precise mechanism (presumably involving preferential surface migration and nucleation in the microscopic "valleys") that results in healing of the roughness. Study of the effect of such buffer layers on surface roughness, as well as the effect of other substrate pre-treatments, has begun.

## Work Accomplished

*Substrate Preparation*

Si films have been deposited by sputtering on a variety of substrates, and the effect of the films on surface roughness characterized with the techniques described below. The substrates studied to date include diamond-turned aluminum, float glass,

and polished semiconductor-grade Si wafers. These substrate materials are important for future thin-film work in the visible and XUV optics, electronics, and magnetism fields. Si wafers and float glass were treated with three commonly used cleaning procedures to determine their effects on roughness. Simple detergent cleaning, a three-step acid cleaning procedure and a 22-step acid cleaning procedure were used to prepare Si wafers for growth of films by MBE.

*Characterization of Surface Roughness*

Substrate surfaces were characterized with a scanning tunneling microscope (STM) and a WYKO phase-shifting interferometer, both before and after the deposition of Si films by sputtering. The STM used for this initial work was made available through a collaboration with Dr. Dereniak's group.

The STM and the WYKO interferometer have comparable vertical resolutions: 1 Å for the former instrument and 3 Å for the latter. However, their horizontal resolutions differ by a factor of $10^4$; that is, approximately 1 Å for the STM and 2 $\mu$m for the WYKO. Thus, the WYKO measurement determines the "waviness" of the surface, while the STM, with its atomic scale resolution, measures roughness over spatial dimensions that have large effects on the physical properties of many thin films and multilayers.

The STM measurements made to date were complicated slightly by the fact that the instrument used operates in air, and by the instrument not always being immediately available for use. Since this technique requires a conductive surface, a thin layer of Ag (100 Å) was deposited over the Si buffer layer to prevent the growth of an insulating oxide layer prior to the STM measurement. This also was necessary for the float glass, in order to create a conductive surface.

STM surface profiles of a diamond-turned aluminum flat were found to show a small periodic ripple in the surface before deposition, presumably an artifact of the diamond-turning process. However, measurements of the auto-correlation function of the surface after deposition of the buffer layer showed the surface to have become much more random. Analyzing many such measurements leads to the conclusion that the Si buffer layer succeeds in randomizing the diamond-turned surface, but has little effect on the root-mean-square (RMS) roughness. Thus, in the case of diamond-turned aluminum, there may be some advantage to depositing a Si buffer layer, since a random surface can have a more predictable effect on the properties of a coating than one with periodic fluctuations. For the other two substrate materials studied, polished Si and float glass, the deposition of an Si buffer layer did not improve either the RMS roughness or the randomness of the surface. However, this

preliminary conclusion should be re-examined after further measurements are made on Si buffer layers deposited under other conditions.

WYKO measurements also were performed on the substrates before and after the various cleaning procedures. The three-step acid etch was found to leave a clean but otherwise unmodified surface. The detergent method left rough patches, while the 22-step acid procedure increased the roughness of the polished wafers over the entire area sampled.

## Plans

One major goal of this work is to develop techniques to determine the auto-correlation of surface roughness over length scales continuously spanning the range of approximately 1 Å to 1 mm. Initial results toward this goal have been highly encouraging. The continuation of these roughness-healing studies will make use of improved STM hardware and software to bridge the gap in horizontal resolution between the STM and the WYKO measurements. During the coming year, a Nanoscope II STM will be used to make measurements over much larger areas than was possible previously, and then averaging software will be used to produce an accurate picture of the roughness over a variety of intermediate horizontal-length scales.

A systematic study of roughness as a function of surface pretreatment and sputter-deposition parameters will be performed. A search will be made for an improved MBE substrate-cleaning procedure that can remove chemically bonded impurities, such as carbon, without increasing the roughness of the polished surface.

## Personnel

C. M. Falco
Z. Milanovic
J. M. Slaughter

## Collaborations

Dereniak: STM studies of substrates
Gibson: STM studies of surfaces
Leavitt: RBS analysis of films

## References


1. Z. Milanovic, M. A. Voelker, M. F. Kelley, K. D. Powers, and C. M. Falco, "Surface roughness healing of substrates for XUV multilayer coatings," Proc. SPIE, in press.

2. P. A. Kearney, J. M. Slaughter, K. D. Powers, and C. M. Falco, "Soft x-ray multilayers produced by sputtering and molecular beam epitaxy (MBE): substrate and interfacial roughness," Proc. SPIE, in press.

TASK 7

## CHARACTERIZATION FACILITY

Principal Investigator: U. J. Gibson

### Project Goal

Set up a central facility for characterization of thin films, surfaces, and substrates.

### Work Accomplished

The Characterization Facility became fully operational in the last year, with construction of a dedicated site, installation of the electron microscopes, acquisition of sample preparation and other equipment, and mastery of their operation. The facility is seeing increased use from a variety of the URI participants.

*Equipment*

TEM: JEOL 2000FX, with 1.2 Å resolution and micro-diffraction capability.
SEM: JEOL JSM-U3; should be replaced with new instrument by mid-December.
WYKO interferometric profilometer
OLYMPUS analytical microscope with phase contrast and TV monitor
NANOSCOPE I scanning tunneling microscope (STM)
Sample preparation equipment for SEM and TEM
Scatterometer/scanning microscope from Task 8

*Experiments in Progress*

Use of crystalline Si, $SiO_2$, and opal for polishing damage studies
STM imaging of polished and coated substrates
Development of microtome techniques for thin-film samples

## Plans

Acquire and install scanning coils and a TV for the TEM

Acquire and install a cold stage for the ion thinner

Upgrade the STM for digital data acquisition

## Personnel

U. J. Gibson

V. Lindley

M. Kelley

TASK 8

## MICRO-SCANNING SCATTEROMETER AND POLISHING STUDIES

Principal Investigator: R. Parks

### Project Goal

Design and implemention of a surface-scattering measurement instrument, with good lateral resolution and a greater sensitivity to surface rather than volume defects, was the major goal of this Task. Comparative studies of polishing procedures were also performed.

### Summary

An instrument has been constructed that measures scattered light through a small aperture as a sample is scanned. The instrument and its software are functional, and the instrument was evaluated by W. Wolfe, whose assessment points out that the instrument is too unlike conventional scatterometers to be calibrated against them. It is, however, more sensitive to local variations in scattering efficiency than other techniques such as BRDF.

In tests against a WYKO interferometer, the instrument appeared less sensitive to surface-height variations than the WYKO and lateral resolution was comparable.

It is not yet clear that the instrument has merits above existing techniques for characterizing bare surfaces. A study to determine if it can be used to characterize thin films by means of light scattered out of a waveguide may be undertaken.

### Work Accomplished

*Scatterometer*

During the past year, the micro-scanning scatterometer was completed as a stand-alone device, and software for its control and image processing was written and documented. Following a period of check out and calibration, the device was turned over to W. Wolfe's group for calibration against sample of known BRDF characteristics; his report appears as an appendix later in this document.

Currently, the instrument is fitted with a sample holder that accepts 1-in. diameter by 0.125-in. samples. A calibration sample is used to center the scan and

set the laser illuminator and photometer to a constant level before scanning actual samples. Samples may be scanned over areas 1 $cm^2$ or smaller, in user-defined steps down to 1 $\mu m$. Sample resolution at the detector is currently 7 $\mu m$. This could be reduced by a factor of three before the illumination level would be too weak to be practical.

During the check out and calibration phase, a 10-$\mu m$ slit etched in chrome was used to determine the instrument profile. Both sides of the slit were clearly visible to the scatterometer and there was no evidence of stray light giving a false or ghost image of a second slit. The instrument was also checked for fixed pattern noise caused by speckle from the laser illumination system. Again, there was no evidence of fixed pattern noise.

Measurement of a Lambertian surface (as determined by BRDF with a 2-cm spot size), revealed intensity variations point-to-point with a 5:1 ratio. This is the result of the small aperture and large collection angle of the new scatterometer, which measures short distance variations in the surface.

*Polishing Studies*

Several surfaces with different degrees of roughness and damage were produced for the Thin Film Center and to support development of the scatterometer.

A polishing procedure was established that generates a surface on a fused-silica substrate with a roughness of about 0.2-nm rms. (This is the measurement limit of the WYKO profilometer.) Crystals of silicon and quartz were polished; a surface roughness of 0.8-nm rms was produced on silicon substrates, and surfaces on quartz substrates with a roughness of about 0.3-nm rms were produced.

A comparison of Silvernail polishing compounds is underway using fused-silica substrates. Preliminary results show that these compounds can produce very smooth surfaces, but the results are limited by the measurement capability of the profilometer.

Some experiments were conducted with electroless nickel to obtain metal substrates for further polishing studies.

**Personnel**

R. E. Parks
R. Sumner
J. Sasian
C. Kittrell

Development Proposal

# SPECTRAL ELLIPSOMETRY

Principal Investigator: R. Zanoni

## Project Goal

Funding is requested for development of a research-grade spectroscopic ellipsometer. This instrument will be based on a new design that combines multiple angle-of-incidence measurements with a spectroscopic phase-modulation ellipsometer (MA-SPME). The accuracy of commercial-grade ellipsometers is at least an order of magnitude smaller than that of a PME operating at one wavelength. With the multiple wavelength and multiple angle-of-incidence capabilities, this new instrument will have increased accuracy and additional measurement capabilities. The MA-SPME will be able to measure the refractive index of optical surfaces and films, film thickness, inhomogeneous films, spectral absorption, birefringence, crystal symmetry, and surface roughness.

## Introduction

The research programs funded by URIP require basic characterization of the linear optical properties of thin films such as refractive index, absorption, dispersion, thickness, and birefringence over a wide range of optical wavelengths. These programs include:

* Brillouin spectroscopy
* Thin-film growth and characterization
* Nonlinear optics of thin films:
    - Organic film characterization
    - Semiconductor characterization
    - Second harmonic generation
* Surface studies:
    - Roughness
    - Optical constants
    - Effects of surface polishing

For example, Brillouin spectroscopy requires information about thin-film optical symmetries, refractive index, and thickness for films as thin as several Langmuir-Blodgett monolayers (1 monolayer ≅ 3 nm). Second harmonic generation requires the measurement of index of refraction and thickness for films over a wavelength range of 0.5 to 2.0 $\mu$m. Since investigation of new materials is becoming an increasingly important area in optics, the ability to characterize these new materials quickly and accurately is crucial in order to utilize these materials within existing optics programs. A variety of methods are used currently to make these measurements, but a single work station that can routinely characterize new thin-film materials would be an invaluable addition to the Center.

## Ellipsometry

Invented nearly 100 years ago, ellipsometry provides a convenient method for obtaining optical properties by measuring the intensity of polarized light reflected from an optical surface. The interpretation of ellipsometric data is not a simple task, and thus the development of ellipsometry has paralleled the development of computers. Within the past 25 years, new variations of ellipsometry have been implemented and tested. It is now possible, with the appropriate instrumentation, to make measurements on bulk or thin-film samples that may be anisotropic, inhomogeneous, microscopically rough, covered with adsorbed layers, or have finite interface widths.

Conventional null ellipsometry (CNE) used nulling methods to find the polarization states that, on reflection from a sample, extinguish the light incident on a detector. The quadratic dependence of the intensity on instrument settings near null, and the necessity of operating the detector at very low light levels, limit null instruments to intense spectral line sources. Optical characterization requires accurate spectral data, and this is the domain of spectral ellipsometry (SE). Spectral ellipsometry is dominated by photometric instruments in which one of the elements is rotated or modulated to vary systematically the flux reaching the detector. In addition to being easily automated, these instruments operate at high optical efficiency and are well suited for use with weak continuum sources.

There are three classes of spectral ellipsometer: rotating analyzer (RAE), rotating polarizer (RPE), and phase modulated (PME). The RAE and RPE have the advantage of simplicity, since the only wavelength-dependent element is the sample itself. Systematic errors are less likely with the RAE than with the RPE because polarization-insensitive detectors are available, while polarization-free sources are not.

The PME is not affected by source-polarization or detector-polarization sensitivity, is capable of high-speed operation, and has no mechanically moving parts. So, the spectroscopic PME is the instrument of choice for characterizing thin-film materials.

*Ellipsometric Accuracy*

Ellipsometers measure the complex reflectivity $\rho = R_p/R_s = \tan\psi e^{i\delta\Delta}$ of a reflecting sample, where $R_p$ and $R_s$ are the p- and s-polarized light reflectivities. The ellipsometric angles, $\psi$ and $\Delta$, are related to the polarizer angle and the analyzer angle in CNE. These ellipsometric angles, together with the angle of incidence, $\phi$, determine the ultimate accuracy for film thickness and refractive index in a given ellipsometric measurement. The accuracy of a thickness measurement made by ellipsometry as a function of wavelength is shown in Fig. 1. The accuracy of the instrument increases to 1% for short wavelengths ($\cong$ 250 nm), provided that the ellipsometric angles $\psi$, $\Delta$, and $\phi$ are accurate to $\pm 0.001^0$. The accuracies of thickness and refractive index measurements at $\lambda = 0.6328$ $\mu$m for a commercial-grade instrument versus the proposed research instrument are listed in Table 1. (The accuracies of the ellipsometric angles for the commercial instrument are: $\psi = \pm 0.04^0$, $\Delta = \pm 0.08^0$, and $\phi = \pm 1/60^0$. These values were obtained from the literature for a commercial instrument made by SOPRA (ESG-2).)

**Table 1.** Measurement accuracy at $\lambda = 0.6328$ $\mu$m for research and commercial ellipsometers.

| Film Thickness (nm) | Research-grade instrument ($\pm 0.001^0$) | | Commercial-grade instrument (SOPRA) | |
|---|---|---|---|---|
| | $\%(\delta t_{rms}/t)$ | $\%(\delta n_{rms}/n)$ | $\%(\delta t_{rms}/t)$ | $\%(\delta n_{rms}/n)$ |
| 2.5 | 17.0 | 0.89 | 460.0 | 24.0 |
| 5.0 | 4.3 | 0.29 | 120.0 | 6.0 |
| 10.0 | 1.1 | 0.20 | 30.0 | 1.5 |
| 50.0 | 0.72 | 0.19 | 2.1 | 0.08 |
| 100.0 | 0.015 | 0.19 | 0.75 | 0.08 |

The film model assumed in this case is a polymer film (n = 1.55) on a fused-silica substrate (n = 1.46). The research-grade instrument is clearly at least an order of magnitude better than the commercial ellipsometer. Further, the errors shown can be reduced an order of magnitude by decreasing the wavelength, as shown in Fig. 1.

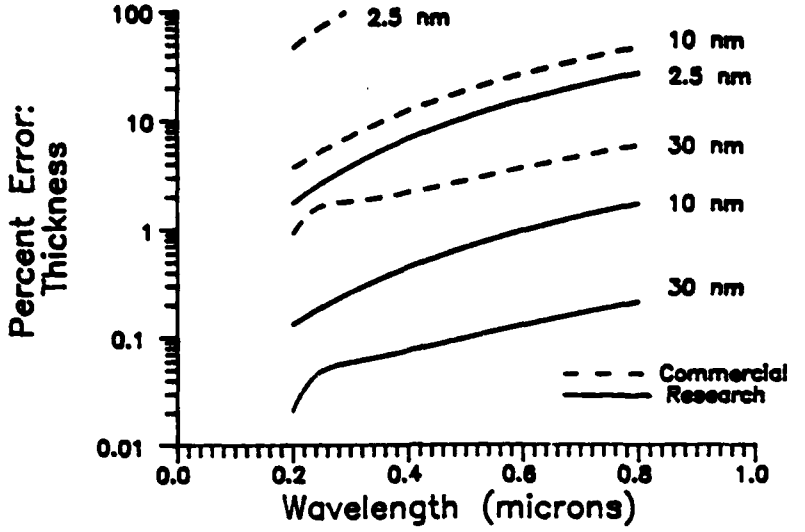


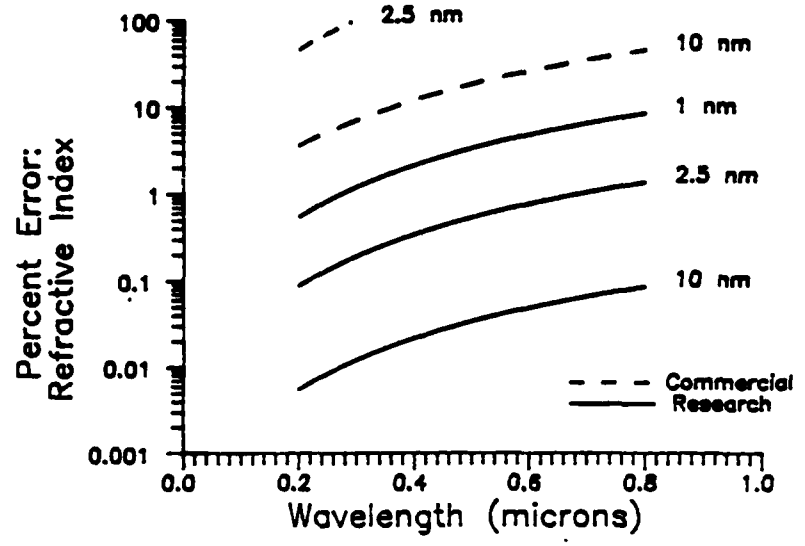


*Figure 1. Ellipsometric accuracy for an ellipsometer with $\delta\phi = \delta\Delta = \delta\psi = \pm 0.001^0$: (a) percent error in thickness ($\delta t/t$) versus wavelength; (b) percent error in refractive index ($\delta n/n$) versus wavelength.*

**Program Description**

Construction of a research-grade, automated spectroscopic ellipsometer is proposed. The instrument design will be based on a phase-modulated ellipsometer. However, unlike a commercial instrument, the polarizer position and analyzer angle will be fixed. The incident polarization will be modulated by an acoustic shear wave transducer. The accuracy of the ellipsometric angles can be expected to be

± 0.001°. The instrument will be mounted on a computer-controlled goniometer to allow multiple angle-of-incidence ellipsometric measurements. This will improve the overall accuracy of the ellipsometric measurements, as well as providing additional information to obtain birefringence data. A tungsten-halogen light source will be used, together with a monochromator, to scan a range of wavelengths from 200 to 800 nm. Provision for IR wavelengths from 800 to 2000 nm will be added later.

The program will procceed in two phases:

1) In the first year, the basic ellipsometer, without spectral capability, will be made operational. A multi-line, HeNe source will be used to simplify the development of the ellipsometer; in a parallel effort, the spectral source and monochromator will be assembled.

2) The goniometer and spectral capability will be added in the second year, completing the MA-SPME.

Development of this instrument will allow single-station characterization of thin films at the Center, as well as providing insight into the ultimate accuracy of MA-SPME instruments.

# APPENDIX A

# XPS and RHEED studies of Si(100) Substrate Preparation for Epitaxial ZnS Growth

Joy K. Watanabe
Andrew J. Stentz
Ursula J. Gibson

Optical Sciences Center
University of Arizona
Tucson, AZ 85721

## Abstract

We report on angle resolved photoemission of Si (100) substrates prepared for growth of ZnS by atomic layer or molecular beam epitaxy. In particular, we investigate the growth habit of the first monolayer of zinc, and find qualitative differences in the behavior as a function of substrate cleaning procedure, and pretreatment with $H_2S$ gas. RHEED studies did not indicate a significant lowering of the temperature required to remove $SiO_2$ from the Si wafer.

## INTRODUCTION

A great deal of attention has been paid in recent years to the deposition of epitaxial thin films of zinc chalcogenides. These compounds have already found significant application as electroluminescent displays, and their large direct bangap has led to their pursuit for short wavelength light emitting diodes and lasers.[1-2]

Several reports have been made of epitaxial growth of ZnS on Si(100), by MBE,[3-4] from compound source materials. By contrast, in ALE, once growth of ZnS is established, sequential pulses of Zn and S, or of compounds containing these elements, are brought to the substrate with a time lag between them.[5] This allows a layer by layer growth of the material, and has been reported to assist in the exclusion of some impurities.[6] The formation of the first layer of ZnS is obviously critical for epitaxial growth, whether from an elemental or compound source material. A recent report on MBE growth of ZnS on Si suggested that an $H_2S$ treatment of the wafer, prior to deposition of ZnS, enhanced the resulting film quality.[4] This work was initiated to clarify the effect of $H_2S$ exposure on a Si wafer, and to determine its effect on the growth habit of initial layers of Zn deposited onto the surface.

## EXPERIMENTAL

Silicon (100) substrates were cleaned using a Pirhana/RCA-1/RCA-2/$H_2O$/HF/$H_2O$ procedure.[4] The final $H_2O$ rinse lasted 3 or 5 minutes, allowing formation of an oxide on the silicon surface. The wafer pieces were then mounted with gallium onto stainless steel one inch Perkin-Elmer (PE) XPS sample stubs, and transferred to the growth chamber via a PE sample introduction rod.

The $H_2S$ exposures and Zn depositions were performed in a UHV chamber (shown in Fig. 1) pumped by a combination of a turbopump and Ti sublimation pump. A liquid nitrogen cooled source shroud contained the Zn effusion cell, and the $H_2S$ was bled in through a needle valve, and a nozzle that directed the gas stream toward the substrate. Base pressures were typically $5\times10^{-10}$ Torr prior to heating of the stub and introduction of the $H_2S$ gas. The samples were heated by electron bombardment to a maximum temperature of 700-770°C. Sample temperatures were measured approximately using a thermocouple mounted on the manipulator stage and calibrated against the stub temperature. In each experiment, the substrate was heated until a RHEED pattern was observed.

Experiments were performed to determine whether the RHEED pattern was observable at lower temperatures in the presence of $H_2S$, and to measure surface impurites after cleaning and heating with and without $H_2S$, and to determine the growth habit of thin Zn layers deposited on substrates prepared these two ways.

For the RHEED pattern onset studies, the sample was loaded onto the manipulator, and the stub temperature was raised in 50°C increments. At each temperature, the manipulator was adjusted in search of a pattern. This procedure was followed both with and without a backpressure of $1\times10^{-7}$ Torr of $H_2S$ gas. The procedure for the depositions was as follows: After cleaning and loading, the samples were heated to 700°C for approximately 30 minutes. The samples were then cooled to 300°C, which required approximately 30 minutes. If $H_2S$ was used, it was admitted to a pressure of $1\times10^{-7}$ Torr for 30 minutes, with the substrate held at 300°C. These substrates will be referred to as Si(A). If no $H_2S$ was admitted (Si(B) sample), the substrate was held at 300°C to keep heating times equal. The samples were then either transferred in an unpumped vacuum vessel to the PHI 5100 for XPS analysis, or after pumping out the $H_2S$, deposited upon with Zn at the rate of 1 Å per second, to a thickness of 100 Å indicated on the quartz crystal monitor.

The difference in temperature between the crystal (22°) and the substrate (300°C) led to an expected deposit thickness of 10-20 Å.

## RESULTS & DISCUSSION

The onset temperature for the RHEED patterns was not measurably affected by the presence of $H_2S$ during heating, however, both the quantity and bonding of carbon and oxygen impurities showed the influence of the $H_2S$ treatment. The strongest effect was seen in the growth habit of the Zn layers after treatment, where $H_2S$ was seen to promote layer-like growth. The presence of an interfacial layer of S is believed to be responsible for this behavior.

The angle resolved data were analyzed using the model of C. S. Fadley[7] for the formation of thin layers on a substrate. In his model, the ratio of the film to substrate signals is described by

$$R = K\gamma \frac{1 - \exp(-t/\Lambda(E^i)\sin\theta)}{(1 - \gamma) + \gamma\exp(-t/\Lambda(E^k)\sin\theta)},$$

where

R = ratio of film to substrate signal,
K = geometrical factor,
$\gamma$ = percentage of the covered substrate,
t = film thickness,
$\Lambda(E^i)$ = mean free path of an electron with kinetic energy $E^i$,
$\theta$ = electron take off angle.

This model results in a smoothly decreasing ratio of the film to substrate signal ratio as the detector is moved from a glancing angle geometry to 90° with respect to the substrate plane. For the case of thin layers, the coverage of the substrate and film thickness may be determined by performing a fit to the experimentally observed data.

XPS survey and angle resolved analysis, seen in Fig. 2, after chemically cleaning the silicon substrate indicated that there were 3-4 monolayers (ML) of oxygen and 2-3 ML of carbon contamination. Increasing the length of each of the second $H_2O$ rinses from 3 to 5 minutes affected the quantity and bonding of the impurities: the amount of oxygen doubled, the carbon increased slightly, and the C-O (286 eV)[8] bonding was favored over O-Si (533 eV),[8] C-Si (283 eV),[9-10] C-C, and C-H (284 eV)[10] bonds.

After heating the wafer at 700°C for 30 minutes, dissociation of C-O bonds and formation of C-Si bonds were observed (shown in Fig. 3). A decrease of oxygen and carbon impurities occurred for Si(A) wafers exposed to $H_2S$, but not for Si(B) wafers which did not undergo the $H_2S$ treatment. Also, a larger percentage of the total oxygen bonded to Si(B) than to Si(A).

The graphs in Fig. 4 show the XPS Zn(A) signal was significantly weaker than that from Zn(B), indicating more zinc condensed onto the Si(B) wafers. Figure 5 shows graphs of relative intensities Zn(A)/Si(A) and Zn(B)/Si(B) vs. take off angle. The first, Zn(A)/Si(A) smoothly decreases which is characteristic of a thin layer with approximately 50 coverage and 8 Å thickness. The second curve, Zn(B)/Si(B) does not decrease smoothly. A high zinc aspect ratio, (i.e. three-dimensional growth), could account for the rapid decrease in substrate signal at lower angles.

In summary, we have observed that $H_2S$ pretreatment of Si wafers affects the surface impurities, and modifies the growth of thin Zn layers. Removal of O and C contamination is believed to be responsible for an improved interface. Bonding of S to the surface of the wafers encourages two-dimensional growth in thin Zn layers, and may be a useful technique for quenching antisite defects in ZnS grown from a molecular source.

## REFERENCES


1. M. Yamaguchi, A. Yamamoto, and K. Kondo, J. Appl. Phys. 48, 196 (1977).
2. L. G. Walker and G. W. Pratt, Jr., J. Appl. Phys. 47, 2129 (1976).
3. Meiso Yokoyama, Ko-ichi Kashiro, and Shin-ichi Ohta, Appl. Phys. 60, 3508 (1986).
4. Yang Yongnian, Carolyn F. Hickey, and Ursula J. Gibson, Thin Solid Films 151, 207 (1987).
5. T. Suntola and J. Anston, U.S. Patent No. 4058430 (1977).
6. M. Pessa and Goodman, unpublished.
7. Charles S. Fadley, Prog. Solid State Chem. 11, 265 (1976).
8. C. D. Wagner, W. M. Riggs, L. E. Davis, J. F. Moulder, and G. E. Muilenberg, *Handbook of X-Ray Photoelectron Spectroscopy,* (Perkin-Elmer Corp., Eden Prarie, MN, 1979) pp. 38-43.
9. B. R. Weinberger, G. G. Peterson, T. C. Eschrich, and H. A. Krasinski, J. Appl. Phys. 60, 3232 (1986).
10. Wen-Yaung Lee, J. Appl. Phys. 51, 3365 (1980).

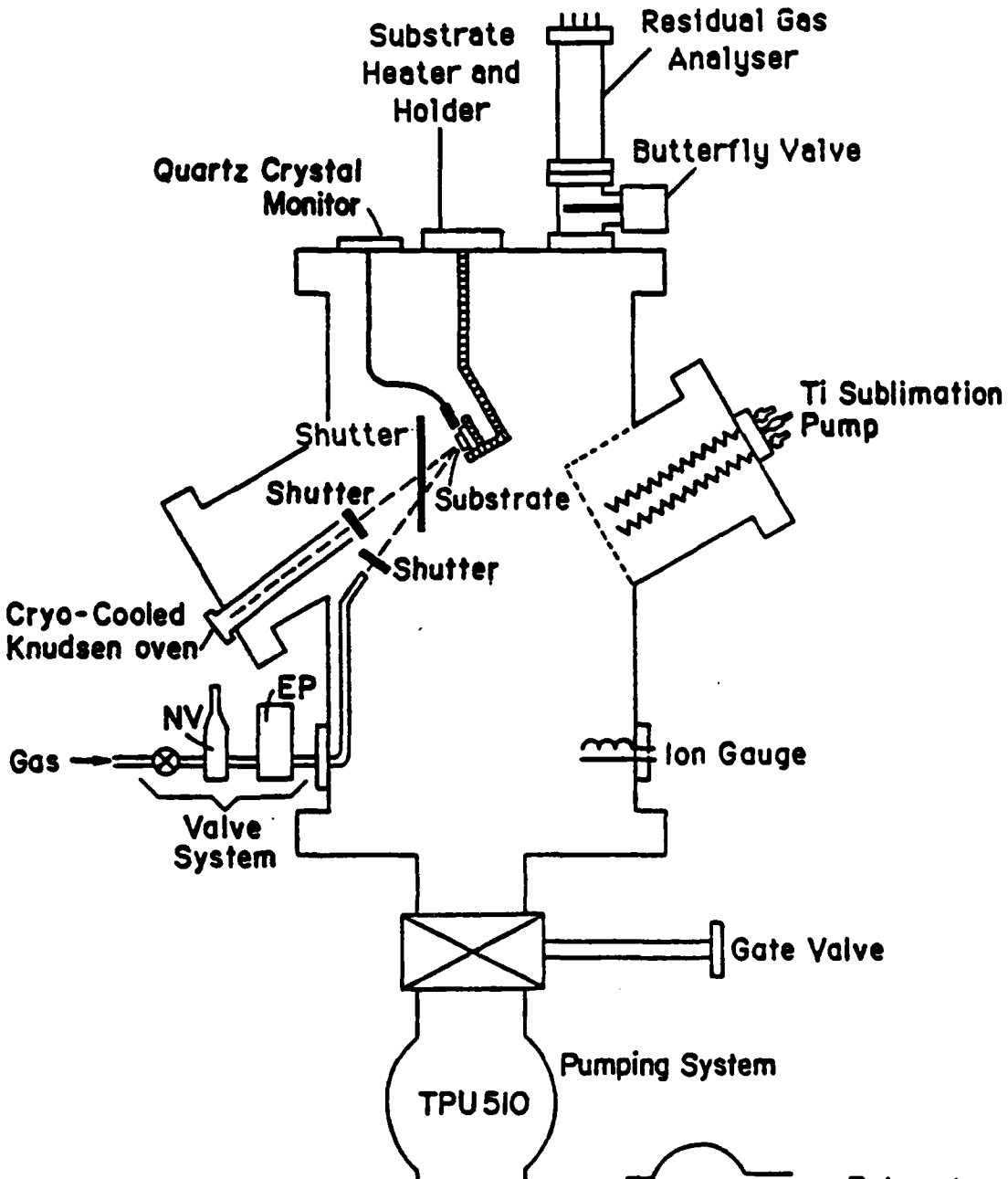


Fig. 1 Vacuum system for MBE and ALE experiments

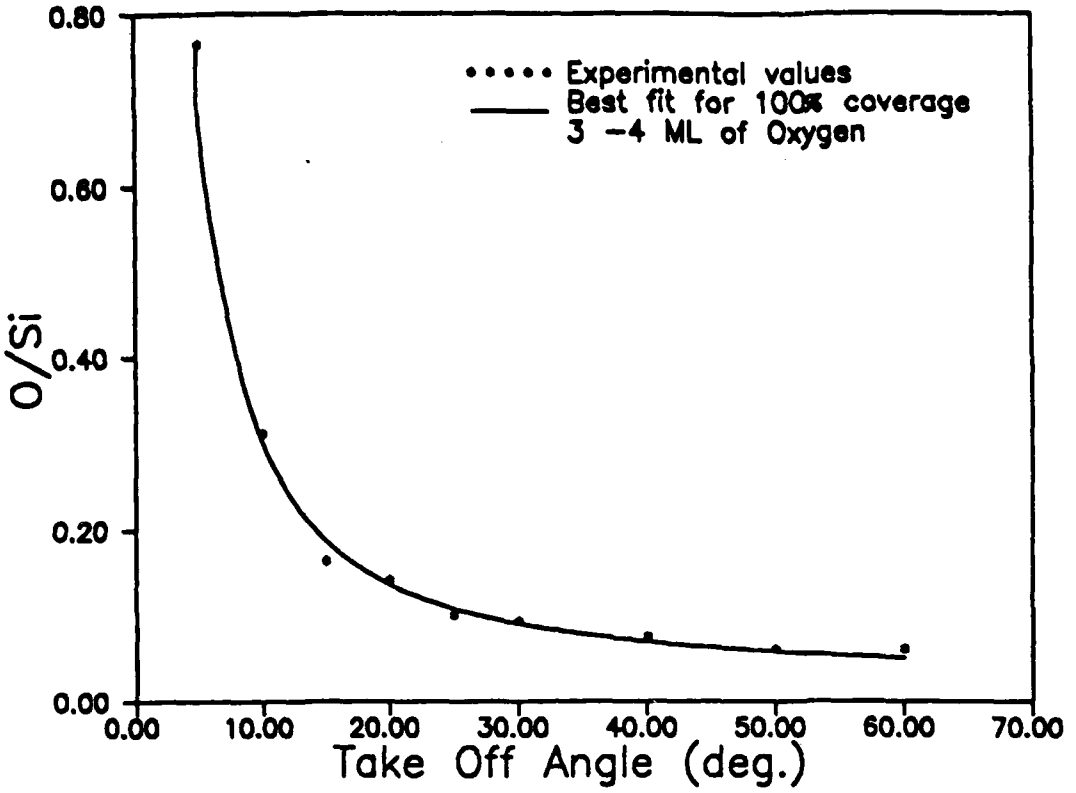


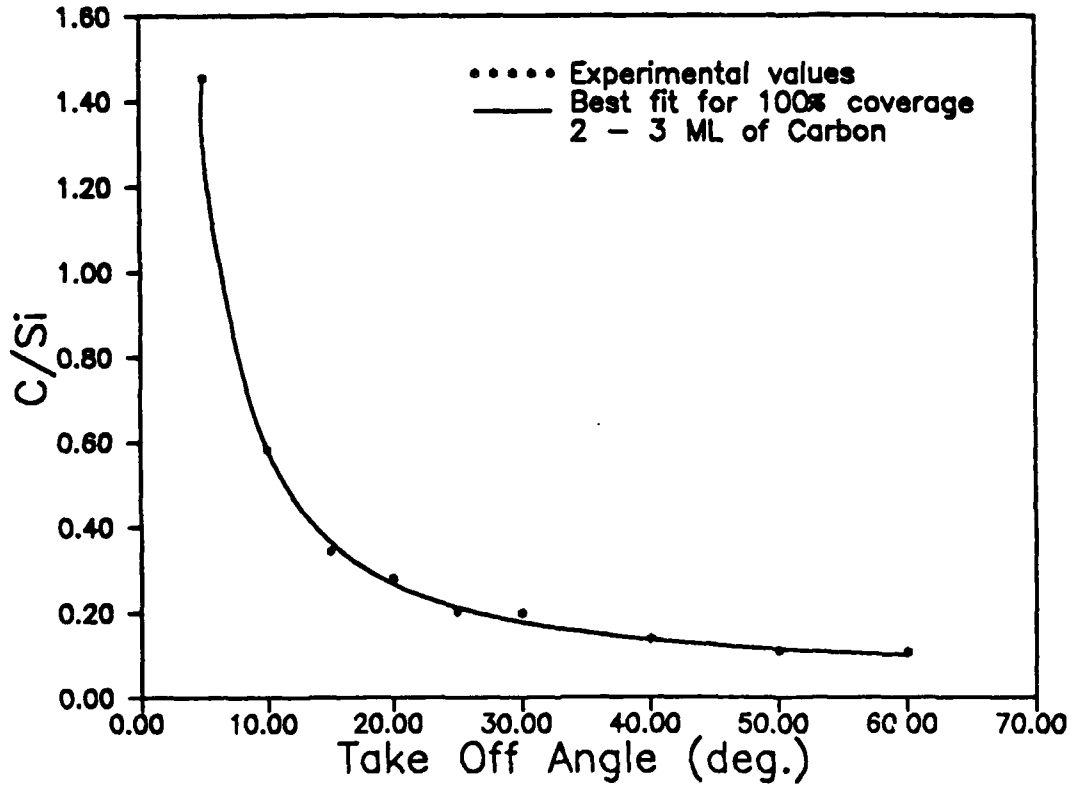


Fig. 2 Impurities on Si(100) after chemical cleaning.

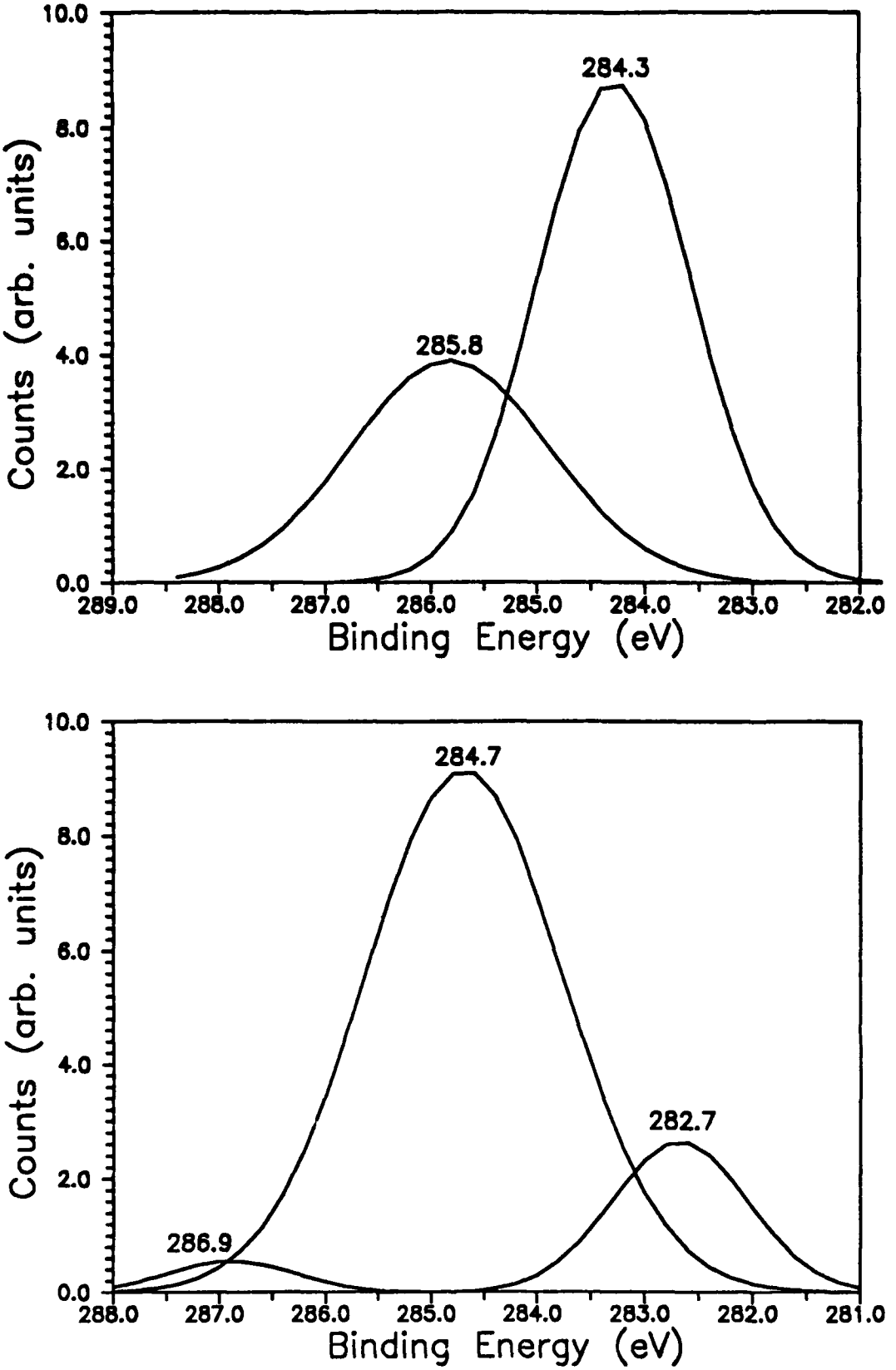


Fig. 3 Carbon bonding after a)chemical cleaning and b)heating.

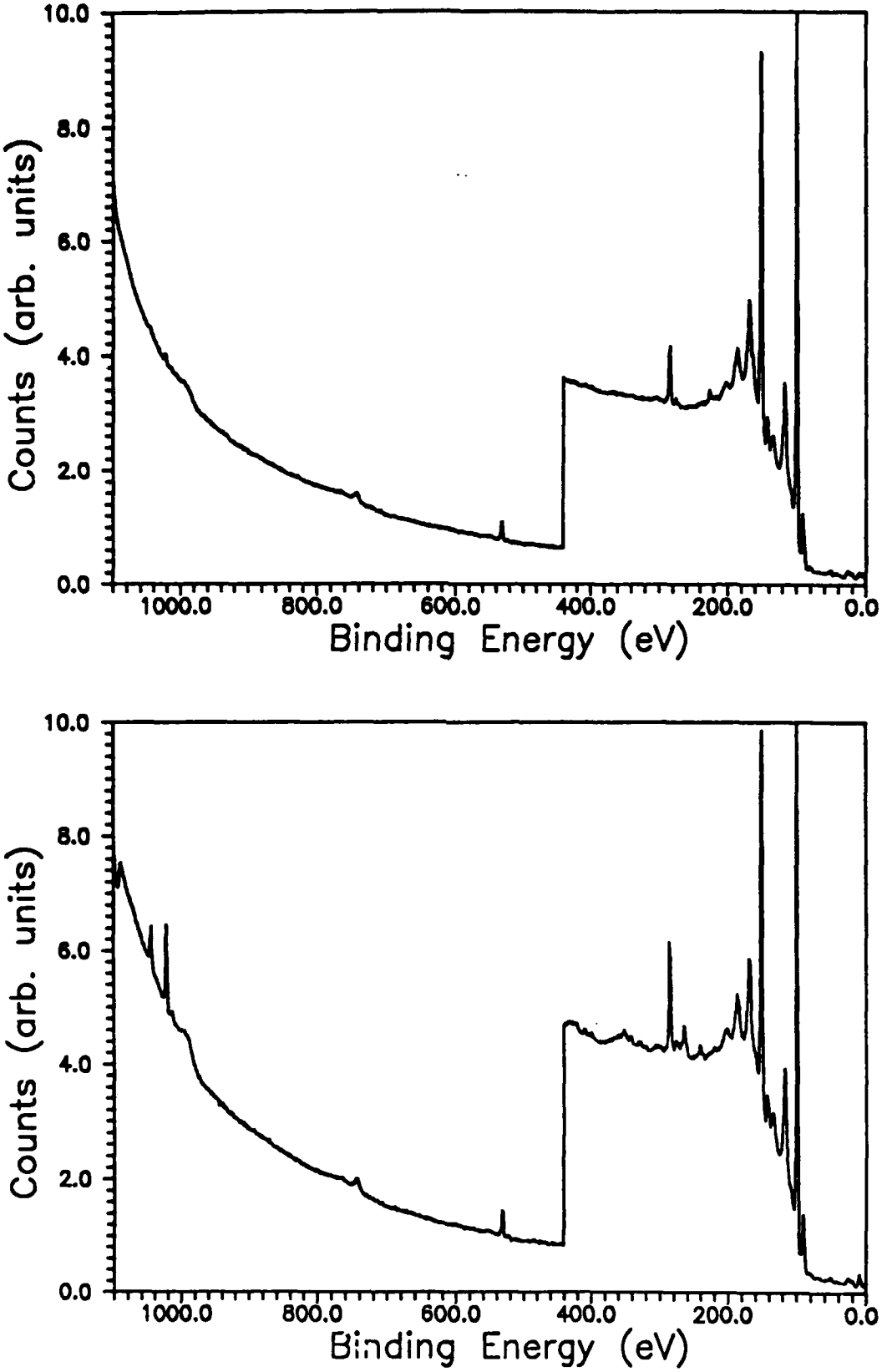


Fig. 4 XPS survey of Zn film on a)Si(A) and b)Si(B).

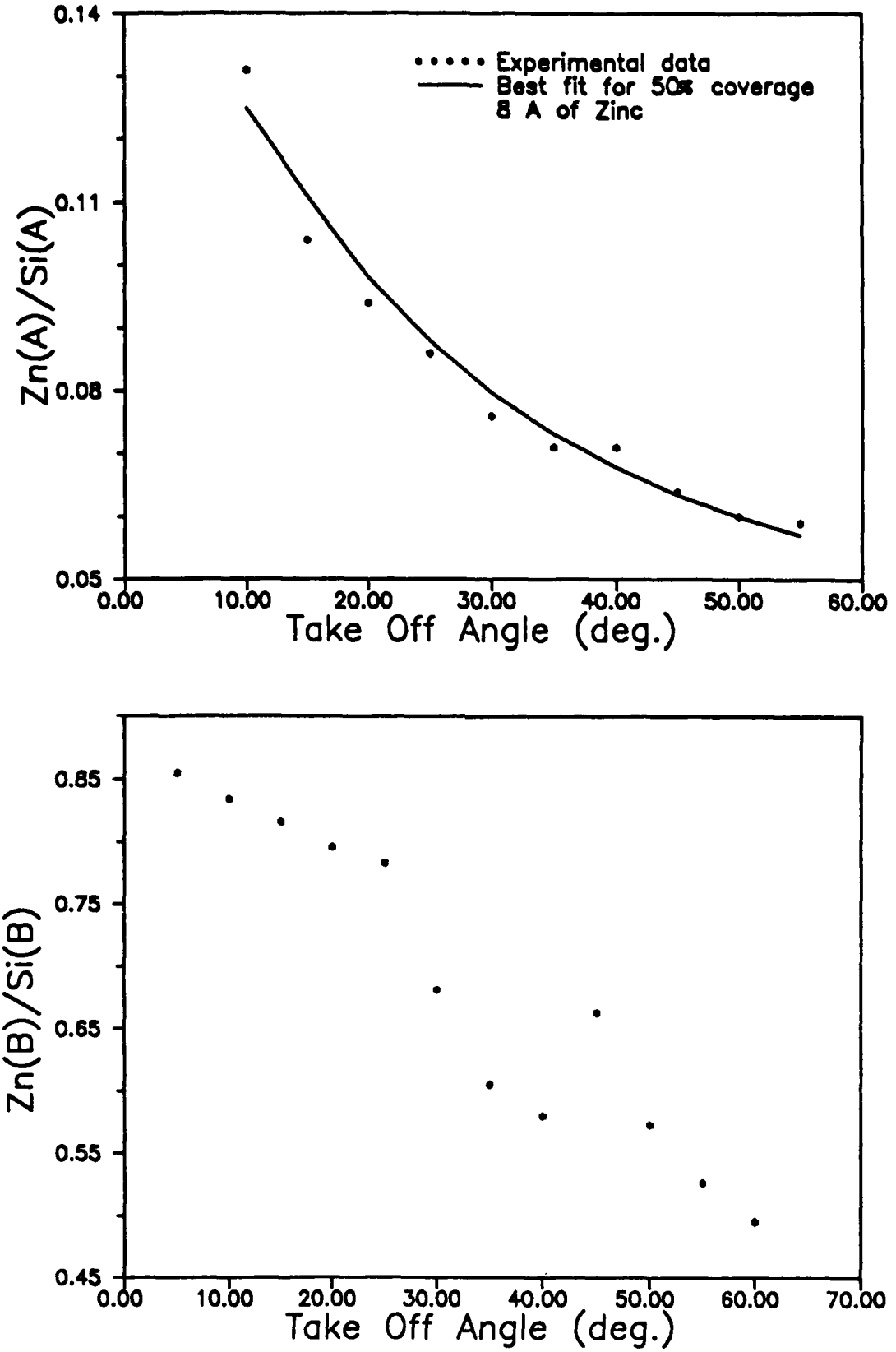


Fig. 5 Zn/Si vs. Take off angle for cases A and B.

# APPENDIX B

# Ion-Assisted Deposition of Thermally Evaporated Ag and Al Films

Chang Kwon Hwangbo, Linda J. Lingg, John. P. Lehan, H. Angus Macleod

Optical Sciences Center

John L. Makous

Department of Physics

University of Arizona

Tucson, AZ 85721

Sang Yeol Kim

Materials Research Laboratory

Pennsylvania State University

University Park, PA 16802

## Abstract

Optical, electrical, and microstructural effects of Ar ion bombardment and Ar incorporation on thermally evaporated Ag and Al thin films are investigated. The results show that as the momentum supplied to the growing films by the bombarding ions per arriving metal atom increases, refractive index at 632.8 nm increases and extinction coefficient decreases, lattice spacing expands, grain size increases, electrical resistivity increases, and trapped Ar increases slightly. In Ag films, stress reverses from tensile to compressive and in Al films compressive stress increases. In the Al films the change in optical constants is due to the presence of voids. The reversal of

stress from tensile to compressive in Ag films requires a threshold level momentum. The increase in electrical resistivity is related to the decrease in grain size and increase in trapped Ar in both types of films. Many of these properties correlate well with the momentum transferred, suggesting that the momentum is an important physical parameter in describing the influence of ion beams on growing thin films and determining the characteristics of IAD thin metal films.

# Ion-Assisted Deposition of Thermally Evaporated Ag and Al Films

Chang Kwon Hwangbo, Linda J. Lingg, John P. Lehan, H. Angus Macleod, John. L. Makous, and Sang Yeol Kim

John. L. Makous is with University of Arizona, Department of Physics, Tucson, AZ 85721; Sang Yeol Kim is with Pennsylvania State University, Materials Research Laboratory, University Park, PA 16802; the other authors are with University of Arizona, Optical Sciences Center, Tucson, AZ 85721.

## I. Introduction

Ion-assisted deposition (IAD) is known to produce thin films with characteristics that conventionally deposited thin films do not have.[1,2,3] For instance, the IAD of dielectric thin films has shown that it increases the packing density and refractive index, reduces the moisture adsorption, and improves the adhesion under certain material dependent conditions.[4,5,6,7,8,9] IAD can also alter the stoichiometry and crystallinity of dielectric thin films.[10,11] For metal thin films, IAD enhanced adhesion in Au, Ag and Al films on glass substrates.[12,13,14,15] IAD of Cr thin films resulted in an increase in reflectance and reversal of stress from tensile to compressive when the ion flux exceeded a critical value.[16] In addition, the non-bulklike optical density, reduction of optical scatter, and control of microstructure in Cu films under ion bombardment were reported.[17,18,19]

The correlation of optical properties and microstructure of IAD thin films with ion beam parameters is very important because it provides insights for understanding and producing these films. It is known that the ion energy and current density are two ion beam parameters which alter the microstructure of naturally growing thin films and their optical properties. It is not clear, however, what physical parameter (energy, momentum or some function of the two) of the ion beam affects growth of thin films.[1] Parmigiani et al.[20] related the normalized energy, defined as the energy delivered by the bombarding ions per arriving metal atom, to the optical, electrical, and microstructural changes of metal films in dual ion beam sputtering.[21] On the other hand, Windischmann[22] derived a model, based on the linear cascade theory of forward scattering, such that the intrinsic stress of ion beam sputtered films depends on the imparted momentum rather than energy.

In this paper, we investigate the optical, electrical, and microstructural effects of Ar ion bombardment and Ar incorporation on thermally evaporated Ag and Al thin films. These effects and incorporated Ar are presented in terms of the momentum supplied to the growing thin film by the bombarding ions per arriving metal atom. We define the momentum (P) normalized by the Ar mass as $\gamma\sqrt{E}$, where $\gamma$ is the (Ar ion)-to-(metal atom) arrival rate at the substrate and E is the Ar ion energy.

## II. Deposition Conditions

Ag was evaporated from a Mo boat and Al was e-beam evaporated from an intermetallic crucible in a Balzers 760 box coater, as shown in Fig. 1. The base pressure was $1 \times 10^{-6}$ mbar. The chamber temperature was ambient and its variation during a single layer deposition was less than $5^{0}$ C. The deposition rates of Ag and Al films were 0.5 nm/sec and 1.0 nm/sec, respectively, as measured by a quartz crystal oscillator. Prisms, glass slides and graphite slabs were used as substrates for the

various post-deposition measurements. Just prior to deposition, substrates were sputter-cleaned *in vacuo* by the Ar ion beam for 5 to 60 seconds, depending upon the type of substrates used.

We employed a 3-cm aperture Kaufman hot-cathode ion source with Ar gas as the bombarding species. Ar gas was admitted through the ion gun until a pressure of $8 \times 10^{-5}$ mbar in the chamber was obtained. The Ar ion energies investigated were 200, 300, and 500 eV while the Ar ion current density was varied from 0 to 20 $\mu A/cm^2$. These parameters resulted in the mass normalized momentum (P) being varied from 0 to 0.48 $\sqrt{eV}$ for Ag films and 0 to 0.46 $\sqrt{eV}$ for Al films, respectively. The non-IAD (conventional) thin film has zero P by definition.

## III. Optical Measurements

### A. Surface Plasmon Resonance

Optical constants at 632.8 nm wavelength and thickness of Ag and Al films were obtained using the surface plasmon resonance (SPR) technique.[23] In the Kretschmann configuration of the SPR, a thin metal film is deposited on the hypotenuse of a right angle prism.[24] When the angle of incidence of a TM wave inside the prism is larger than the critical angle, the incident wave is totally reflected and an evanescent wave is absorbed by the metal film. At a certain incidence angle and film thickness, the component of the wave vector of the electric field parallel to the film plane equals to that of surface plasmon propagating along the metal-air interface and is thus coupled to this surface plasmon mode. When this occurs, the energy of the incident wave is absorbed by the surface plasmon and no wave is reflected by the metal film. This results in the reflectance showing a sharp resonant minimum as the incidence angle

varies above the critical angle. The resonance angle and thickness which yields zero reflectance depend on the optical constants of the metal film.[25] Optimization software employing admittance matching between the incident medium and metal film was used to calculate the resonance angle and thickness.[26] Optimum thicknesses of about 50 nm and 15 nm were chosen for Ag and Al films, respectively. From the measured reflectance with respect to the incident angle, the optical constants and thickness were calculated using a non-linear least squares method.[27] Reflectance calculated from the optical constants and thickness found by the program was in good agreement with the experimental reflectance profile. Measurements were performed within 5 hours after the films were taken out of the vacuum chamber because the SPR technique is sensitive to the oxidation of the metal-air interface.[28]

Refractive index (n) and extinction coefficient (k) of Ag films at 632.8 nm are plotted in Fig. 2 in terms of P. As P increases, n increases and k decreases. Reflectance of 100 nm thickness Ag films at normal incidence is calculated from these optical constants and listed in Table 1. At the highest P (.48 $\sqrt{eV}$), reflectance drops by 2.5 % compared to the non-IAD film. In other words, IAD Ag films become lossy when bombarded with Ar ions.

The n and k of Al films at 632.8 nm shown in Fig. 3 are scattered from a line. Reflectance of Al films of 100 nm thickness at normal incidence is also listed in Table 1. When P is small, reflectance does not change much from that of non-IAD film. However, when P exceeds .23 $\sqrt{eV}$, reflectance of IAD films decreases.

## B. Spectroscopic Ellipsometry

Recently, spectroscopic ellipsometry (SE) has been used as a nondestructive tool to depth-profile multilayer structures and void fractions in thin films, in addition to its traditional role, measuring the optical constants, dispersion, and thickness of thin

films. The void fraction in Au and amorphous IAD Ge thin films and depth-profiling Si, ZnS, MgO, and $ThF_4$ thin films have recently been studied.[29,30,31,32,33] In this work SE was used to measure the optical constants, dispersion, and thickness of metal thin films on glass substrates at an angle of incidence of 70° in the spectral range 1.5-4.5 eV in steps of .05 eV. The void fraction in Al films and its oxide layer thickness were calculated by applying the Bruggeman effective medium approximation and linear regressional analysis to the SE data.[34,35]

Pseudo-refractive index ($n_p$) and pseudo-extinction coefficient ($k_p$), the refractive index and extinction coefficient of the film-substrate assembly, for some Ag films are plotted in Fig. 4 (a) and (b) in terms of photon energy. $n_p$ of the IAD Ag films is larger than that of the non-IAD Ag film below the plasma frequency near 3.8 eV (at which $n_p$ equals to $k_p$).[36] But in the 2.5-3.0 eV spectral region, $n_p$ of the IAD films is almost the same as the non-IAD film. In the interband transitions above the plasma frequency, $n_p$ of the IAD films is lower than that of the non-IAD film. $k_p$ of the IAD Ag films is smaller than that of the non-IAD film except in the vicinity of the plasma frequency. Also, the high P film shows larger $n_p$ and smaller $k_p$ than the low P film, which is consistent with the SPR results. Reflectance of Ag films at normal incidence is calculated from $n_p$ and $k_p$ and plotted in Fig. 5. Reflectance of these IAD films drops by about 1 % in the intraband transitions, while it drops by about 3% in the interband transitions. Around the plasma frequency, surprisingly, the reflectance (interband absorption) increases (decreases) by about 3% for IAD films.

$n_p$ and $k_p$ of Al films are plotted in Fig. 6 (a) and (b). Near the 1.5 eV interband absorption, $n_p$ of the IAD Al films is smaller than that of the non-IAD Al film. In the rest of the measured spectral region (from about 1.8 eV to 4.5 eV), the high P film shows larger $n_p$ than the non-IAD film while the small P film behaves like the non-IAD film. $k_p$ of the IAD films is smaller than that of the non-IAD

film in the whole measured spectral region. Reflectance calculated from $n_p$ and $k_p$ at normal incidence for 100 nm thick films is plotted in Fig. 7. Reflectance of the IAD films drops by about 2 % except at the 1.5eV interband absorption.

Optical properties of metal thin films in the spectral range of intraband transitions can be described phenomenologically by the Drude free-electron model.[39] At near IR frequencies ($\omega >> 1/\tau$)[36], the real and imaginary parts of complex dielectric constants can be written as follows:

$$\epsilon_1 \cong \epsilon_0 - \omega_p^2/\omega^2 = \epsilon_0 - E_p^2/E^2 \quad (1)$$

and

$$\epsilon_2 \cong \omega_p^2/(\omega^3\tau), \quad (2)$$

where $\epsilon_0$ represents core interband transitions, $\omega_p$ is the plasma angular frequency for intraband transitions, $\tau$ is the intraband relaxation time, and $\omega$ is the angular frequency of the light. $E_p$ and E are the energies of the plasma frequency and the incident wave, respectively. The intraband plasma frequency of the conduction electrons, $\omega_p$, is given by

$$\omega_p = \sqrt{4\pi Ne^2/m}, \quad (3)$$

where N is the effective number density of electrons participating in the intraband transitions, and m and e are the free-electron mass and charge, respectively. Also, the d.c. conductivity ($\sigma$) in the Drude free-electron model is expressed by

$$\sigma = \omega_p^2\tau/4\pi. \quad (4)$$

Using eq. (1), we can determine $\omega_p$ of a metal film from the slope of a plot of $-\epsilon_1$ vs $(1/E^2)$. From $\omega_p$ and eq. (3), N can be obtained.

The plots of $-\epsilon_1$ vs $(1/E^2)$ calculated from the pseudo-dielectric constants for Ag and Al films in the intraband transitions are shown in Fig. 8 (a) and (b), respectively. $E_p$ of the IAD Ag film at P = .48 $\sqrt{eV}$ is 7.6 eV, while that of the non-IAD film is 7.7 eV. For the Al films, $E_p$ drops from 10.7 eV of the non-IAD film

to 10.1 eV of the IAD film at $P = .46\sqrt{eV}$. The slope for the IAD films decreases as P increases. The decrease of $E_p$ means a reduction in N, which has to do with the change of microstructure of the metal film.[20,29] The fraction of voids in the Al films is calculated by using the effective medium approximation and linear regressional analysis[34,35] and the results are shown in Table 2. Because the Al films had been exposed to the atmosphere for a few months before the SE measurement was performed, a thin $Al_2O_3$ layer on top of the Al film was taken into account.[40] Since the 100 nm thickness of Al film is much larger than the skin depth of Al (about 10 nm), the incident wave does not see the glass substrate. Hence, bulk Al plus voids is assumed as the substrate. In Fig. 9, the measured dielectric constants of the non-IAD Al film are in good agreement with those calculated from the data modeled in Table 2. The fraction of voids increases as P increases, while the thickness of the oxide layer does not seem to correlate with P.

Analogous to the reduction of interband absorption in the IAD Ag films, the 1.5 eV interband absorption of the IAD Al films decreases. Interestingly, the 1.5 eV interband absorption in the Al films tends to disappear as P increases. Similar observations for Al films on cold substrates were reported by Bernland.[37] In his work, as the substrate temperature decreased from 198 K to 25 K, the 1.5 eV interband absorption decreased and finally disappeared at 25 K. Possible explanations were a lack of (200) translational symmetry at 25 K and an intermediate state between a crystalline and an amorphous state in the Al film on the cold substrate.[37,38] When we investigated our Al films with X-ray diffraction (XRD), we did not observe a (200) orientation for both non-IAD and IAD Al films. So these explanations do not seem applicable to our films. If we assume the reflectance drop for the intraband transitions due to the fraction of voids is extended to the interband transitions, the reduction of the 1.5 eV interband absorption in the IAD Al films should also be due to these voids. Generally, the presence of voids in a thin film means that the charac-

teristics of the film deviate from the bulk.[29,34] Since the 1.5 eV interband absorption is a characteristic of the bulk, the presence of voids may influence it in such a way that the 1.5 eV interband absorption decreases as the void fraction increases.

Given that the fraction of voids correlates well with P, we believe that the presence of voids in the film induced by Ar ions is an important factor which affects the effective number density of electrons in the intraband transitions and thus the optical constants.

## IV. X-Ray Diffraction Analysis

A Bragg-Brentano X-ray diffractometer (XRD) was used to investigate the microstructure of polycrystalline Ag and Al films such as the preferred orientation, lattice spacing and grain size. In addition, the strain and average stress in the film plane were calculated from the change in lattice spacing.

For Ag films, the [111] diffraction profile showed the strongest preferred orientation. The intensity of [200] orientation is about 1/7 of the intensity of the [111] orientation. Thus we will consider only the [111] orientation.

The situation for Al films was more complicated. Thin Al films (15 nm, the same thickness at which the optical constants of Al films were measured using the SPR technique) showed no diffraction peaks. Since these thin Al films had been exposed to the atmosphere for a while before the XRD measurements, an oxide layer comprising an average of 20 to 30 atomic % of the film (as measured by the Rutherford Backscattering Spectrometry) formed at the air-film interface. We believe that the thin oxide layer disturbed the structure of very thin Al films and resulted in no diffraction profiles. For 100 nm thick Al films, the oxide layer comprised only an average of 2 to 3 atomic % of the film and so a diffraction profile was observed, but

only the [111] orientation.

Lattice spacing ($d_{111}$) perpendicular to the film surface was calculated by the Bragg diffraction formula. The variation of $d_{111}$ for Ag films is shown in Table 3 in terms of P. When P is small, $d_{111}$ does not change significantly from that of the non-IAD Ag film. When P exceeds .2 $\sqrt{eV}$, however, $d_{111}$ increases and levels off at 2.360 Å which is slightly larger than the value for Ag powder given by JCPDS[41] (2.359 Å). The results for Al films are shown in Table 4. In contrast to Ag films, $d_{111}$ of IAD Al films keeps expanding slightly as P increases.

The change in lattice spacing is related to the strain ($\epsilon_z$) perpendicular to the film plane as follows:[42]

$$\epsilon_z = (d-d_0)/d_0,$$

where d and $d_0$ are the strained and unstrained lattice spacings, respectively.
If we assume that the film plane is elastically isotropic and follow the developments of Vook and Witt[43] and Huang et al.[44], the average stress ($\sigma_{av}$) and the strain ($\epsilon_s$) in the film plane can be written by

$$\sigma_{av} = \epsilon_z/(2S_{31}')$$

and

$$\epsilon_s = \sigma_{av}(S_{11}' + S_{12}'),$$

where $S_{11}'$, $S_{12}'$, and $S_{31}'$ are the elastic constants in the [111] orientation calculated by rotating the elastic constants for the [001] orientation.[45] The resulting $\epsilon_z$ and $\epsilon_s$ for Ag and Al films are listed in Tables 3 and 4, respectively. The average stress in the film plane is plotted in Fig. 10 as a function of P. Non-IAD and lightly bombarded IAD Ag films exhibit tensile stress, while IAD Ag films above P = .2 $\sqrt{eV}$ show a constant compressive stress value independent of P. Similar stress reversal has been reported in IAD Nb films,[46] dual ion beam sputtered Ag films,[44] and in other sputtered metal films.[47,48] In contrast to Ag films, the stress of IAD Al films is compressive throughout the entire P range and increases slightly with P.

It appears that the compressive stress of IAD Al films correlates well with P while the stress reversal from tensile to compressive for IAD Ag films requires a threshold value of P. Recently, Windischmann[22] proposed a simple scaling law which relates the compressive stress for polycrystalline thin films prepared by ion beam sputtering with the momentum. Also, Hoffman and Gaerttner[16] demonstrated that the important parameter for reversal of stress from tensile to compressive is related to the momentum transfer rather than energy by investigating evaporated Cr films bombarded with inert gases. Our results for stress analyses of IAD Ag and Al films appear to support Windischmann's scaling law and be in good agreement with Hoffman and Gaerttner' results.

In addition to strain and stress, XRD allows us to examine the grain size in our films. Grain size ($L_{111}$) is given by the Scherrer equation,[42]

$$L_{111} = \kappa\lambda/\beta\cos\theta,$$

where $\kappa$ is a constant (taken to be 1), $\lambda$ is 0.1542 nm (Cu K$\alpha$ radiation), $\theta$ is the Bragg diffraction angle, and $\beta$ is the angular width of the pure diffraction profile on $2\theta$ scale. We corrected for instrumental broadening by assuming Gaussian profiles and applying the John's correction method.[42] As shown in Fig. 11, $L_{111}$ of IAD Ag films is smaller than that of the non-IAD film and it does not change significantly within the experimental error as P increases. On the other hand, $L_{111}$ of IAD Al films decreases monotonically as P increases and at $P = .46\ \sqrt{eV}$ $L_{111}$ of the IAD Al film was only about 67 % of that of the non-IAD film.

## V. Electrical Resistivity Measurement

The electrical resistivity ($\rho$) of Ag and Al films at ambient temperature was measured by the van der Pauw four-point method.[49] With the appropriate correction

factors, $\rho$ of a flat metal film of arbitrary shape can be measured if the four contacts are at the circumference of the homogeneous film. Resistivity for Ag and Al films are shown in Fig. 12 as a function of P. $\rho$ of IAD films increases as P increases.

It is known that the electrical resistivity of a thin metal film is larger than that of the bulk and decreases as the thickness of the film increases. Fuchs developed a free-electron model to explain this phenomenon by considering the size effects of a thin film.[51] In his theory, the thin film is assumed to be a homogeneous slab and electrons are scattered not only in the bulk, but also by the smooth film surfaces. Real polycrystalline films, however, have different structures from the corresponding bulk. Modified models, based on Fuchs' theory and taking into account surface roughness[52], grain boundaries[53], and charge carriers localization[54], were later proposed. These also are not complete because the polycrystalline films studied have defects, dislocations, and impurities. With this in mind, Sambles[55] pointed out that extreme care must be taken in analyzing and interpreting the data of resistivity measurement.

Since Ar ion bombardment on the growing Ag and Al films introduces microstructural changes, the pure Fuchs' theory is not valid for our films. The RMS surface roughness of our films was about 1 nm as measured by a non-contact surface profiler (WYKO TOPO 2D) and no significant difference in the surface roughness between non-IAD and IAD films was observed. We can thus exclude surface roughness as a factor in the differences in $\rho$ between IAD and non-IAD films. Also, surface scattering due to the film thickness effects is relatively negligible because the grain size of Ag and Al films is smaller than the thicknesses ( about 50 nm and 100 nm for Ag and Al films, respectively) and so volume scattering dominates.

When Parmigiani et al.[20] applied Mayadas'[53] grain boundary scattering model to ion bombarded Ag films prepared by dual ion beam sputtering, it was found that the reflection coefficient ($R_g$) at the grain boundary depended on the deposition condi-

tions. Since Mayadas' model assumes a constant $R_g$ for films of the same metal, the different $R_g$ for each film was attributed to the different potential barrier at the grain boundaries due to the structural changes.

In this paper, we applied Vancea's model[54] that the reduced effective number density of electrons (N) participating in the d.c. conductivity is a cause for the increase of resistivity of metal thin films. Vancea's model seems to be a more important factor for the increase of $\rho$ of our films than grain boundary scattering because we observed the reduction of N in the analysis of the real part of complex dielectric constants which is related to the decrease of the d.c. conductivity in the free-electron model by equation (4). Also, in Vancea's model, each grain acts as a potential well with the boundaries as barriers. Free electrons which pass through the potential barrier contribute to the d.c. conductivity. As the grain size decreases, the number of barriers increases, more electrons are trapped at grain boundaries, and the number of effective electrons participating in the d.c. conductivity decreases. This model thus relates the reduction of N and decrease in grain size to the increase of $\rho$. Since the reduction of N implies an increase in void fraction as discussed in the SE section, the presence of a larger fraction of voids in IAD films seems to contribute to the increase of electric resistivity via Vancea's model.

## VI. Rutherford Backscattering Spectrometry Analysis

The stoichiometry of our films was measured by Rutherford Backscattering Spectrometry (RBS). Incident singly ionized helium ($^4He^+$) ions with 1.892 MeV energy are backscattered by a thin film sample. The number of scattered ions per unit solid angle per incident ion is measured and compared with the known Rutherford scattering cross section. A simple calculation then yields the absolute number per unit area

of each atomic species in the film.[56] The film stoichiometry thus can be measured very accurately. Graphite substrates were used because the Si and O peaks in a glass substrate would overlap the Al and O peaks in the films and thus reduce the accuracy.

The atomic % of Ar in Ag and Al films is plotted in Fig. 13 in terms of P. Even though the amount of trapped Ar is less than 2 atomic %, it responds well to P in both Ag and Al films. The average atomic % of oxygen in Ag films is less than .1% and therefore negligible. Al films, on the other hand, have most of their oxygen at the surface with the variation of average atomic % of oxygen from run to run being less than .2 %. Therefore, it seems that Ar ion bombardment on Al films does not influence the natural oxidation of the Al surface as discussed in modeling of Al films in the SE section.

It is known that the trapped Ar atoms in films under ion bombardment reside at grain boundaries.[20] According to Vancea's model, Ar atoms trapped at grain boundaries increase the height of potential barriers, more electrons are localized at grain boundaries, and the electrical resistivity increases. However, we can speculate that since Ar atoms in films are forced into the film by the ion gun, they all do not necessarily reside at grain boundaries and some may reside within grains. If this hypothesis is correct, the small amount of Ar in grains cannot be neglected as a factor in the change of electrical resistivity and stress. Therefore, in either case, the inclusion of Ar in films seems to affect electrical and structural properties. Since the electrical resistivity and Ar concentration increase as P increases, we can expect the electrical resistivity to increase with Ar concentration.

## VII. Conclusions

The following are observed in IAD Ag and Al films as the momentum transferred to the growing film by the Ar ion beam per arriving metal atom increases:

(1) In the intraband transitions, the refractive index increases and extinction coefficient decreases, resulting in a decrease in reflectance. The interband absorption (reflectance), however, decreases (increases). The changes in optical constants are due to the reduction of the effective number density of free electrons in the intraband transitions and the increase in the void fraction of the films.

(2) The lattice spacing perpendicular to the film surface expands. The stress changes from tensile to compressive for Ag films. The compressive stress of Al films increases slightly. The grain size decreases for both types of films. The dependence of stress on P supports Windischmann's scaling law which relates stress to the momentum.

(3) The electrical resistivity increases. This is attributable to the reduced effective number density of free electrons rather than to grain boundary scattering. The decrease of grain size increases the number of potential barriers which results in the decrease of effective number density of free electrons. This is in good agreement with the observed reduction of the effective number density of free electrons in the intraband transitions resulting from an increase in the fraction of voids.

(4) The amount of trapped Ar increases slightly. Whether Ar atoms are at grain boundaries, in grains, or in voids, they cannot be neglected as a factor which affects the optical, electrical, and structural properties.

From the results of this study, IAD is likely to make Ag and Al metal thin films less-bulklike by changing their microstructure. Also, many of their optical, electrical, and microstructural properties correlate well with the momentum transferred to the growing film by the Ar ions per arriving metal atom, suggesting that the momentum is an important physical parameter in describing the influence of ion beams on growing thin films and determining the characteristics of IAD thin metal films.

The authors are extremely grateful to the University Research Initiative Program of the Air Force Office of Scientific Research for financial support. We wish to thank Prof. C. M. Falco of the University of Arizona Physics Department and Optical Sciences Center for allowing us to use the X-Ray diffractometer; Prof. J. A. Leavitt of the University of Arizona Physics Department for RBS measurements; and Prof. K. Vedam of the Pennsylvania State University Materials Research Laboratory for the SE measurements. Also, we would like to thank Dr. M. R. Jacobson for helpful discussions and M. R. Potoff and S. I. Rana for technical support.

## References

1. J. M. E. Harper, J. J. Cuomo, R. J. Gambino, and H. R. Kaufman, "Modification of Thin Film Properties by Ion Bombardment during Deposition," in *Ion Bombardment Modification of Surfaces*, O. Auciello and R. Kelly, Eds. (Elsevier, Amsterdam, 1984).

2. P. J. Martin, "Ion-based Methods for Optical Thin Film Deposition," J. Mat. Sci. 21, 1 (1986).

3. U. J. Gibson, "Ion Beam Processing of Optical Thin Films," in *Physics of Thin Films* 13, M. H. Francombe and J. L. Vossen Eds. (Academic Press, San Diego, 1987).

4. P. J. Martin, H. A. Macleod, R. P. Netterfield, C. G. Pacey, and W. G. Sainty, "Ion-beam-assisted Deposition of Thin Films," Appl. Opt. 22, 178 (1983).

5. R. P. Netterfield, W. G. Sainty, P. J. Martin, and S. H. Sie, "Properties of $CeO_2$ Thin Films Prepared by Oxygen-ion-assisted Deposition," Appl. Opt. 24, 2267 (1985).

6. S. G. Saxe, M. J. Messerly, B. Bovard, L. DeSandre, F. J. Van Milligen, and H. A. Macleod, "Ion Bombardment-induced Retarded Moisture Adsorption in Optical Thin Films," Appl. Opt. 23, 3633 (1984).

7. T. Allen, "Properties of Ion Assisted Deposited Silica and Titania Films," Proc. Soc. Photo-Opt. Instrum. Eng. 325, 93 (1982).

8. E. H. Hirsch and I. K. Varga, "The Effects of Ion Radiation on the Adhesion of Germanium Films," Thin Solid Films 26, 445 (1978).

9. C. M. Kennemore III and U. J. Gibson, "Ion Beam Processing for Coating $MgF_2$ onto Ambient Temperature Substrates", Appl. Opt. 23, 3608 (1984).

10. P. J. Martin, R. P. Netterfield and W. J. Sainty, "Modification of the Optical and Structural Properties of Dielectric $ZrO_2$ films by Ion-assisted Deposition," J.

Appl. Phys. 55, 235 (1984).

11. J. D. Targove, J. P. Lehan, L. J. Lingg, H. A. Macleod, J. A. Leavitt, and L. C. McIntyre, Jr., "Ion-assisted Deposition of Lanthanum Fluoride Thin Films," Appl. Opt. 26, 3733 (1987).

12. S. S. Nandra, F. G. Wilson and C. D. Desforges, "Modification of Gold Coatings by Ion Bombardment during Deposition", Thin Solid Films 107,335 (1983).

13. W. C. Herman,Jr and J. R. McNeil, "Ion Beam Application for Optical Coating," Proc. Soc. Photo-Opt. Instrum. Eng. 325, 101 (1982).

14. P. J. Martin, W. G. Sainty, and R. P. Netterfield, "Enhanced Gold Film Bonding by Ion-assisted Deposition," Appl. Opt. 23, 2688 (1984).

15. M. Laugier, "The Effect of Ion Beam Bombardment on Stress and Adhesion in Thin Films of Silver and Aluminum", Thin Solid Films 81, 61 (1981).

16. D. W. Hoffman and M. R. Gaerttner, Modification of evaporated chromium by concurrent ion bombardment, J. Vac. Sci. Technol. A 17, 425 (1980).

17. F. Parmigiani, E. Kay, T. C. Huang, and J. D. Swalen, "Interpretation of the Nonbulklike Optical Density of Thin Copper Films Grown under Ion Bombardment," Appl. Opt. 24, 3335 (1985).

18. G. A. Al-Jumaily, J. J. McNally, and J. R. McNeil, "Effect of Ion Assisted Deposition on Optical Scatter and Surface Microstructure of Thin Films," J. Vac. Sci. Technol. A, 3, 651 (1985).

19. R. A. Roy, J. J. Cuomo, and Y. S. Yee, "Control of Microstructure and Properties of Copper-films using Ion-assisted Deposition," J. Vac. Sci. Technol. A 6, 1621 (1988).

20. F. Parmigiani, E. Kay, T. C. Huang, J. Perrin, M. Jurich, and J. D. Swalen, "Optical and Electrical Properties of Thin Silver Films Grown under Ion Bombardment," Phys. Rev. B 33, 879 (1985).

21. E. Kay, F. Parmigiani, and W. Parrish, "Effect of Energetic Neutralized Noble

Gas Ions on the Structure of Ion Beam Sputtered Thin Metal Films", J. Vac. Sci. Technol. A 5, 44 (1987).

22. H. Windischmann, "An Intrinsic Stress Scaling Law for Polycrystalline Thin Films Prepared by Ion Beam Sputtering," J. Appl. Phys. 62, 1800 (1987).

23. W. P. Chen and J. M. Chen, "Use of Surface Plasma Waves for Determination of the Thickness and Optical Constants of Thin Metallic Films," J. Opt. Soc. Am. 71, 189 (1981).

24. F. Abeles and T. Lopez-Rios, "Surface Polaritons at Metal Surfaces and Interfaces," in *Surface Polaritons*, V. M. Agranovich and D. L. Mills, Eds. (North-Holland, Amsterdam, 1982).

25. R. D. Olney and R. J. Romagnoli, "Optical Effects of Surface Plasma Waves with Damping in Metallic Thin Films," Appl. Opt. 26, 2279 (1987).

26. H. A. Macleod, "Surface Plasmon Resonance Effects and the Admittance Diagram," Proc. Soc. Photo-Opt. Instrum. Eng. 777, 300 (1987).

27. G. V. Reklaitis, A. Ravindran, and K. M. Ragsdell, *Engineering Optimization Methods and Applications*, (Wiley, New York, 1983).

28. F. S. Zhang, R. W. Wang, H. A. Macleod, R. E. Parks, and M. R. Jacobson, "Surface Plasmon Detection of Surface Contamination of Metallic Film Surfaces," Proc. Soc. Photo-Opt. Instrum. Eng. 777, 162 (1986).

29. D. E. Aspnes, E. Kinsbron, and D. D. Bacon, "Optical Properties of Au: Sample Effects," Phys. Rev. B 21, 3290 (1980).

30. J. E. Yehoda, B. Yang, K. Vedam, and R. Messier, "Investigation of the Void Structure in Amorphous Germanium Thin Films as a Function of Low-energy Ion Bombardment," J. Vac. Sci. Technol. A 6, 1631 (1988).

31. K. Vedam and P. J. McMarr, "Nondestructive Depth Profiling by Spectroscopic Ellipsometry," Appl. Phys. Lett. 47, 339 (1985).

32. K. Vedam, S. Y. Kim, and L. D'Aries, "Nondestructive Depth Profiling of ZnS

and MgO Films by Spectroscopic Ellipsometry," Opt. Lett. 12, 456 (1987).

33. S. Y. Kim and K. Vedam, "Simultaneous Determination of Dispersion Relation and Depth Profile of Thorium Fluoride Thin Films by Spectroscopic Ellipsometry," (to be published in Thin Solid Films).

34. D. E. Aspnes, "Microstructural Information from Optical Properties in Semiconductor Technology," Proc. Soc. Photo-Opt. Instrum. Eng. 276, 188 (1981); see also references listed therein.

35. S. Y. Kim and K. Vedam, "Proper Choice of the Error Function in Modeling Spectroellipsometric Data," Appl. Opt. 25, 2013 (1986).

36. P. B. Johnson and R. W. Christy, "Optical Constants of Nobel Metals," Phys. Rev. B 6, 4370 (1972).

37. L. G. Bernland, O. Hundrei, and H. P. Myers, "Optical Absorption in Vapor-Quenched Aluminum," Phys. Rev. Lett. 31, 363 (1973).

38. D. Y. Smith, E. Shiles and M. Inokuti, " The Optical Properties of Metallic Aluminum," in *Handbook of Optical Constants of Solids*, E. D. Paulik, ed. (Academic Press, Orlando, 1985).

39. J. M. Ziman, *Principles of Theory of Solids*, 2nd Ed. (Cambridge University Press, 1972).

40. R. W. Fane and W. E. J. Neal, "Optical Constants of Aluminum Films Related to the Vacuum Environment," J. Opt. Soc. Am. 60, 790 (1970).

41. Joint Committee on Powder Diffraction Standards, 1601 Park Lane, Swarthmore, PA (1969).

42. H. P. Klug and L. E. Alexander, *X-Ray Diffraction Procedures*, 2nd ed. ( Wiley, New York, 1974).

43. R. W. Vook and F. Witt, "Thermally Induced Strains in Evaporated Films," J. Appl. Phys. 36, 2169 (1965).

44. T. C. Huang, G. Lim, F. Parmigiani, and E. Kay, "Effect of Ion Bombardment

during Deposition on the X-Ray Microstructure of Thin Silver Films," J. Vac. Sci. Technol. A 3, 2161(1985).

45. *American Institute of Physics Handbook*, 3rd Ed. (McGraw-Hill, New York, 1972).

46. J. J. Cuomo, J. M. E. Harper, C. R. Guarnieri, D. S. Yee, L. J. Attanasio, J. Angilello, C. T. Wu, and R. H. Hammond, "Modification of Niobium Film Stress by Low-energy Ion Bombardment during Deposition," J. Vac. Sci. Technol. A 20, 349 (1982).

47. D. W. Hoffman and J. A. Thornton, "Internal Stresses in Sputtered Chromium," Thin Solid Films 40, 355 (1977).

48. J. A. Thornton, J. Tabock, and D. W. Hoffman, "Internal Stresses in Metallic Films Deposited by Cylindrical Magnetron Sputtering," Thin Solid Films 64, 111 (1979).

49. L. J. van der Pauw, "A Method of Measuring Specific Resistivity and Hall Effect of Discs of Arbitrary Shape," Phil. Res. Rep. 13, 1 (1958).

50. R. Chwang, B. J. Smith, and C. R. Crowell, "Contact Size Effects on the van der Pauw Method for Resistivity and Hall Coefficient Measurement," Solid-State Electronics 17, 1217 (1974).

51. K. L. Chopra, *Thin Film Phenomena* (McGraw-Hill, New York, 1969).

52. S. B. Soffer, "Statistical Model for the Size Effect in Electrical Conduction," J. Appl. Phys. 38, 1710 (1967).

53. A. F. Mayadas and M. Shatzkes, "Electrical-Resistivity Model for Polycrystalline Films: the Case of Arbitrary Reflection at External Surfaces," Phys. Rev. B 1, 1382 (1970).

54. J. Vancea and H. Hoffmann, "Reduced Density of Effective Electrons in Metal Films," Thin Solid Films 92, 219 (1982).

55. J. R. Sambles, "The Resistivity of Thin Films-Some Critical Remarks," Thin Solid Films 106, 321 (1983).

56. W. K. Chu, J. W. Mayer and M. A. Nicolet, *Backscattering Spectrometry* (Academic Press, New York, 1978).

Table 1. Reflectance of Ag and Al films of 100 nm thickness at 632.8 nm at normal incidence is calculated from the optical constants obtained from the SPR measurements.

| Ag films | | Al films | |
|---|---|---|---|
| P ($\sqrt{eV}$) | R (%) | P ($\sqrt{eV}$) | R (%) |
| 0 | 98.3 | 0 | 88.8 |
| 0.18 | 97.1 | 0.06 | 88.7 |
| 0.22 | 97.0 | 0.23 | 88.6 |
| 0.29 | 96.7 | 0.36 | 87.2 |
| 0.30 | 96.7 | 0.46 | 84.6 |
| 0.37 | 96.5 | | |
| 0.48 | 95.8 | | |

Table 2. The thickness (t) of an aluminum oxide layer and the fraction (f) of voids in Al films are simulated. The thickness of film is 100 nm.

| P ($\sqrt{eV}$) | t (nm) | f (%) |
|---|---|---|
| 0 | 3.32 | 12.4 |
| 0.12 | 3.47 | 18.2 |
| 0.46 | 2.44 | 20.7 |

Table 3. The lattice spacing ($d_{111}$), strain ($\epsilon_z$) perpendicular the film surface, and strain ($\epsilon_s$) in the film plane are listed. The thickness of Ag films is 50 nm.

Ag films

| $P$ ($\sqrt{eV}$) | $d_{111}$ (Å) | $\epsilon_z$ ($10^{-3}$) | $\epsilon_s$ ($10^{-3}$) |
|---|---|---|---|
| 0 | 2.354 | -2.1200 | 2.40 |
| 0.18 | 2.354 | -2.1200 | 2.40 |
| 0.22 | 2.358 | -0.4240 | 0.48 |
| 0.29 | 2.360 | 0.4239 | -4.80 |
| 0.30 | 2.360 | 0.4239 | -4.80 |
| 0.37 | 2.360 | 0.4239 | -4.80 |
| 0.48 | 2.360 | 0.4239 | -4.80 |
| Powder | 2.359 | | |

Table 4. The lattice spacing ($d_{111}$), strain ($\epsilon_z$) perpendicular the film surface, and strain ($\epsilon_s$) in the film plane are listed. The thickness of Al films is 100 nm.

Al films

| P ($\sqrt{eV}$) | $d_{111}$ (Å) | $\epsilon_z$ ($10^{-3}$) | $\epsilon_s$ ($10^{-3}$) |
|---|---|---|---|
| 0 | 2.343 | 2.14 | 2.01 |
| 0.06 | 2.344 | 2.57 | 2.42 |
| 0.12 | 2.344 | 2.57 | 2.42 |
| 0.29 | 2.345 | 2.99 | 2.82 |
| 0.46 | 2.346 | 3.42 | 3.22 |
| Powder | 2.338 | | |

Fig. 1. The experimental configuration of a Balzers 760 coating plant.

Fig. 2. Refractive index and extinction coefficient at 632.8 nm of Ag films measured by the SPR plotted as a function of P.

Fig. 3. Refractive index and extinction coefficient at 632.8 nm of Al films measured by the SPR plotted as a function of P.

Fig. 4. (a) Pseudo-refractive index and (b) pseudo-extinction coefficient of Ag films measured by the SE plotted as a function of incident photon energy.

Fig. 5. Reflectance of Ag films calculated from the pseudo-refractive index and pseudo-extinction coefficient.

Fig. 6. (a) Pseudo-refractive index and (b) pseudo-extinction coefficient of Al films measured by the SE plotted as a function of incident photon energy.

Fig. 7. Reflectance of Al films calculated from the pseudo-refractive index and pseudo-extinction coefficient.

Fig. 8. $-\epsilon_1$ plotted as a function of $(1/E^2)$ for (a) Ag films and (b) Al films.

Fig. 9. Measured pseudo-refractive index and pseudo-extinction coefficient compared with those calculated from the model in Table 2.

Fig. 10. Stress of Ag and Al films as a function of P.

Fig. 11. Grain size of Ag and Al films as a function of P.

Fig. 12. Resistivity of Ag and Al films as a function of P.

Fig. 13. Ar concentration in Ag and Al films as a function of P.

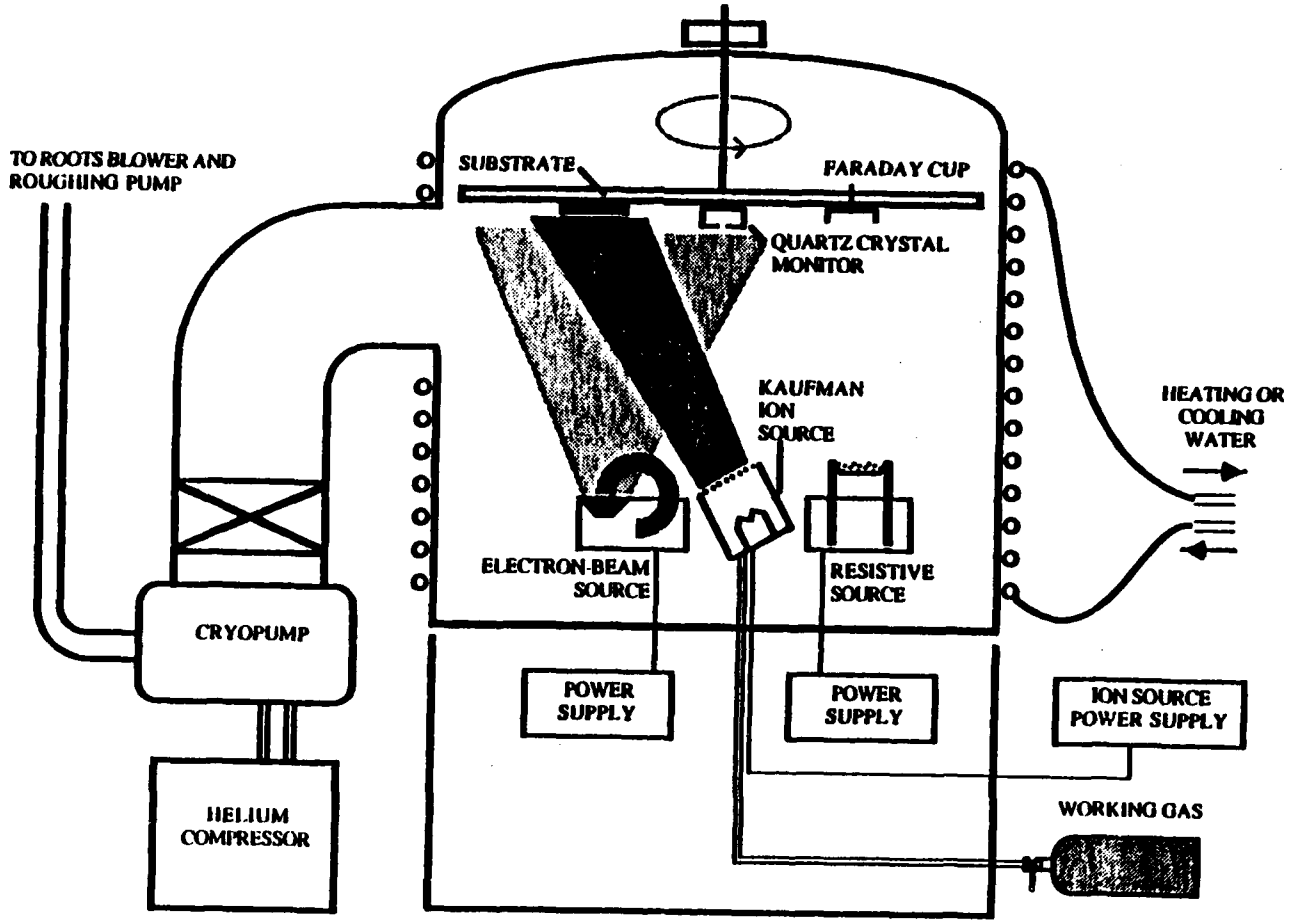
TO ROOTS BLOWER AND ROUGHING PUMP
SUBSTRATE
FARADAY CUP
QUARTZ CRYSTAL MONITOR
KAUFMAN ION SOURCE
HEATING OR COOLING WATER
ELECTRON-BEAM SOURCE
RESISTIVE SOURCE
CRYOPUMP
POWER SUPPLY
POWER SUPPLY
ION SOURCE POWER SUPPLY
HELIUM COMPRESSOR
WORKING GAS

Fig. 1.

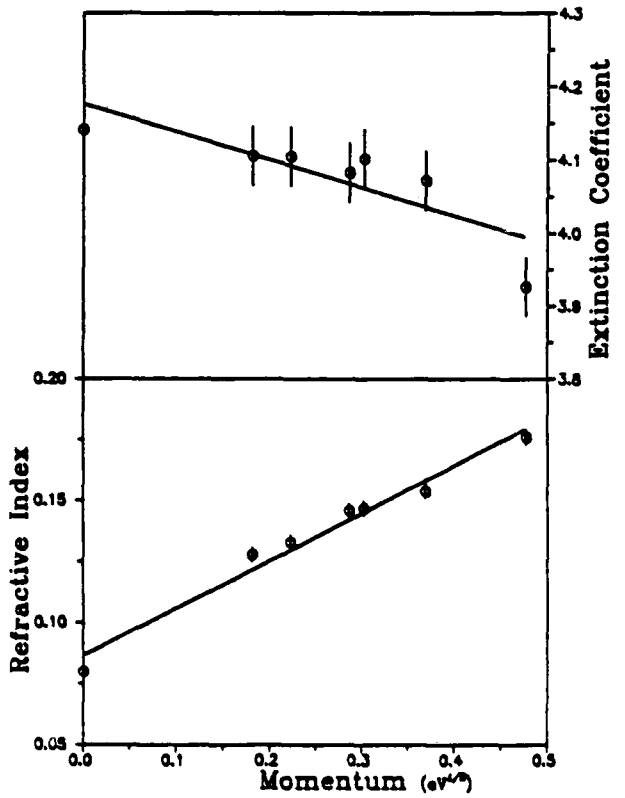


FIG. 2

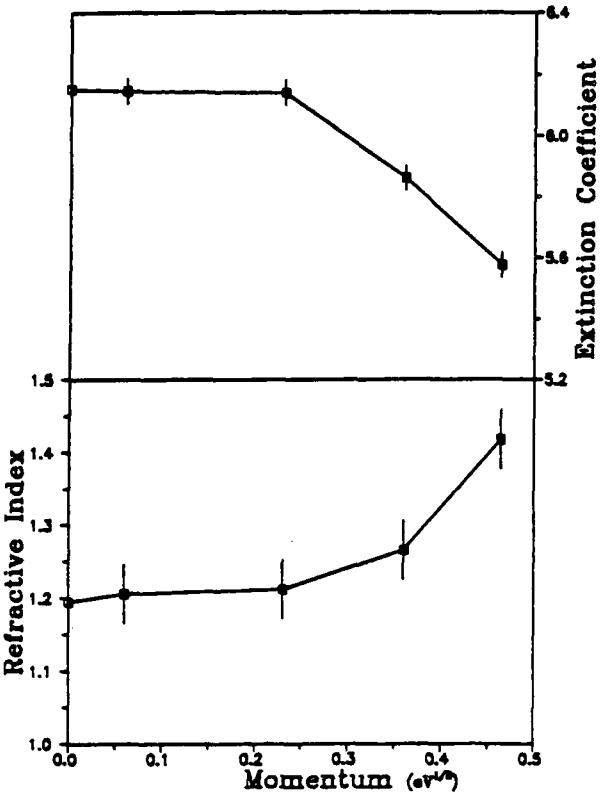


FIG. 3

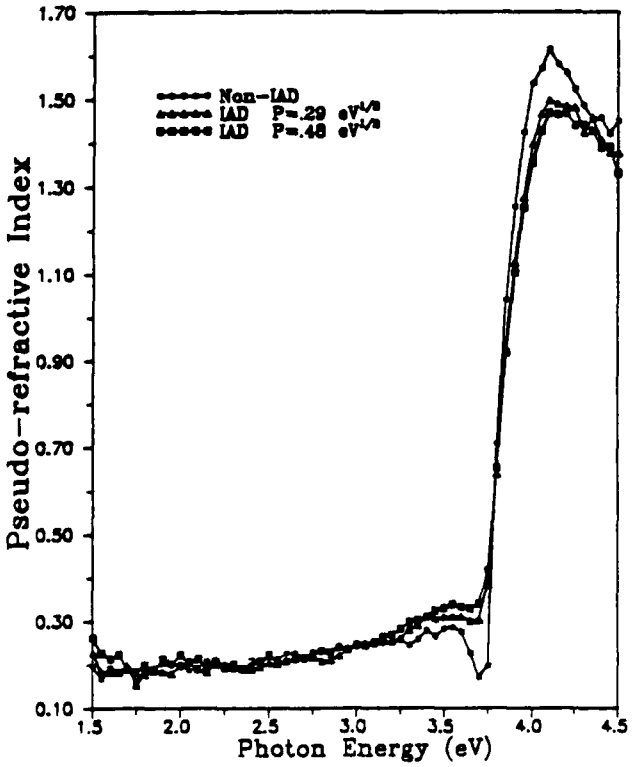


FIG. 4a

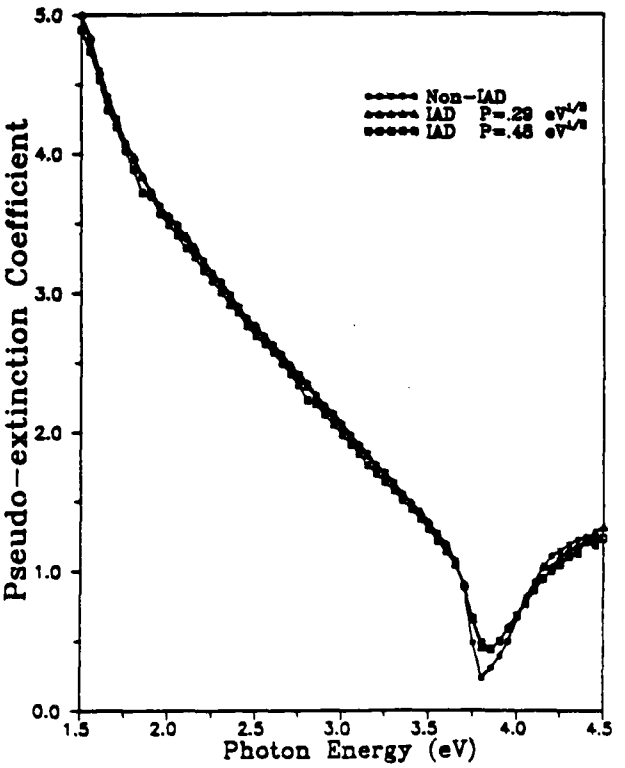


FIG. 4b

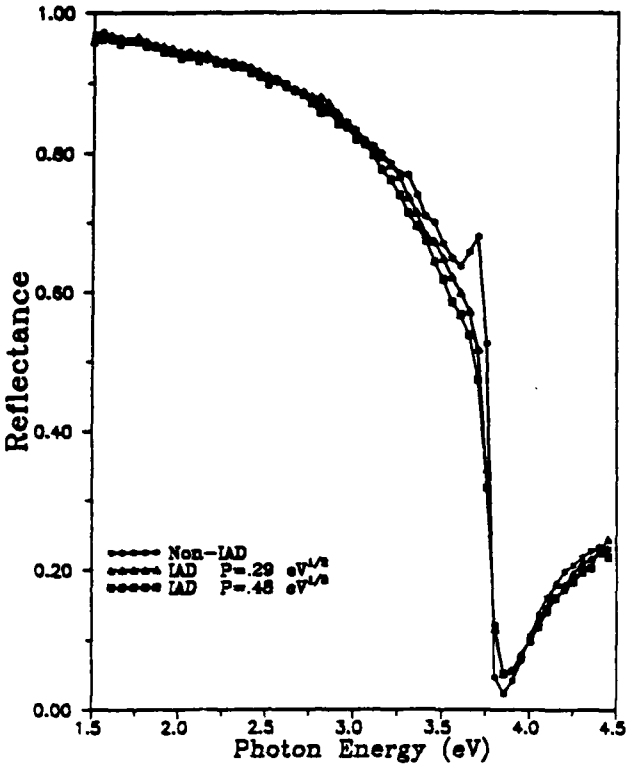


FIG. 5

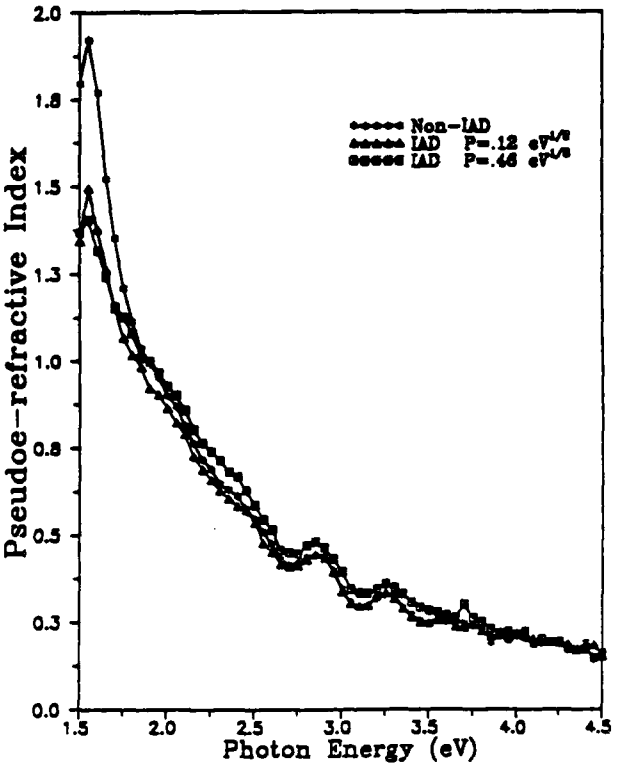


FIG. 6a

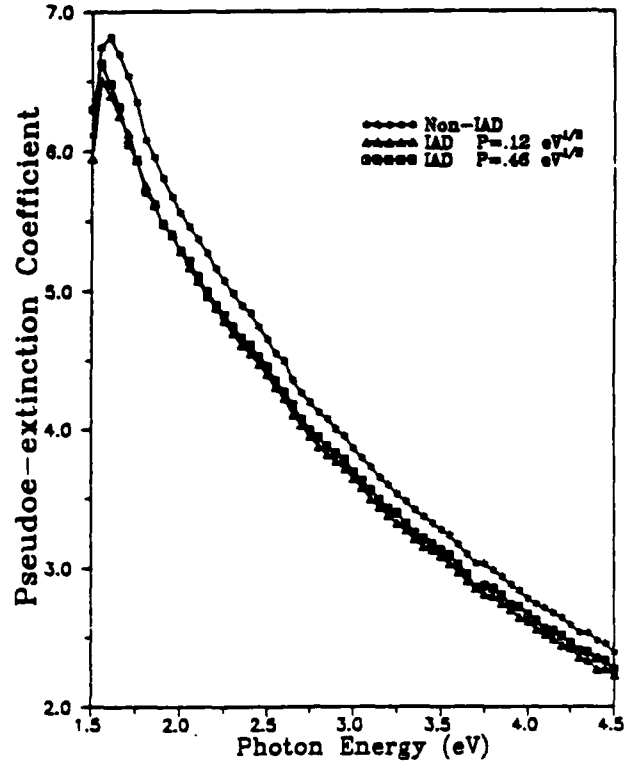


FIG. 6b

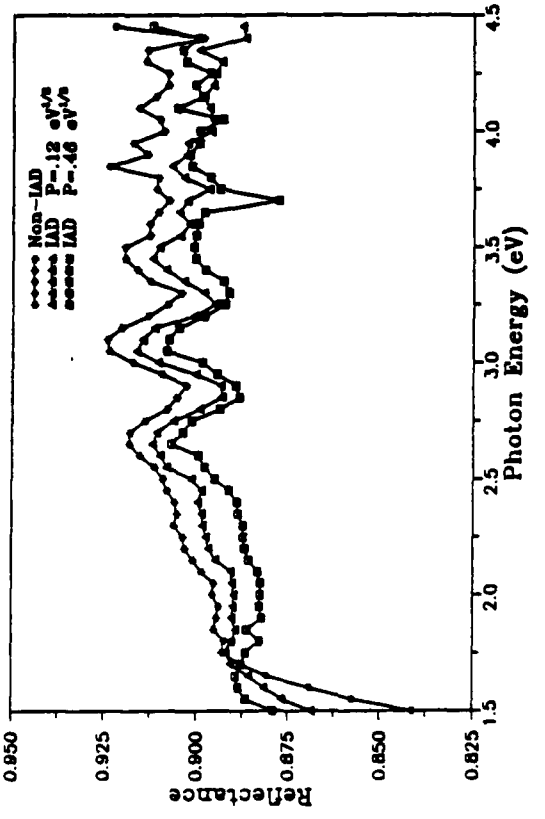


FIG. 7

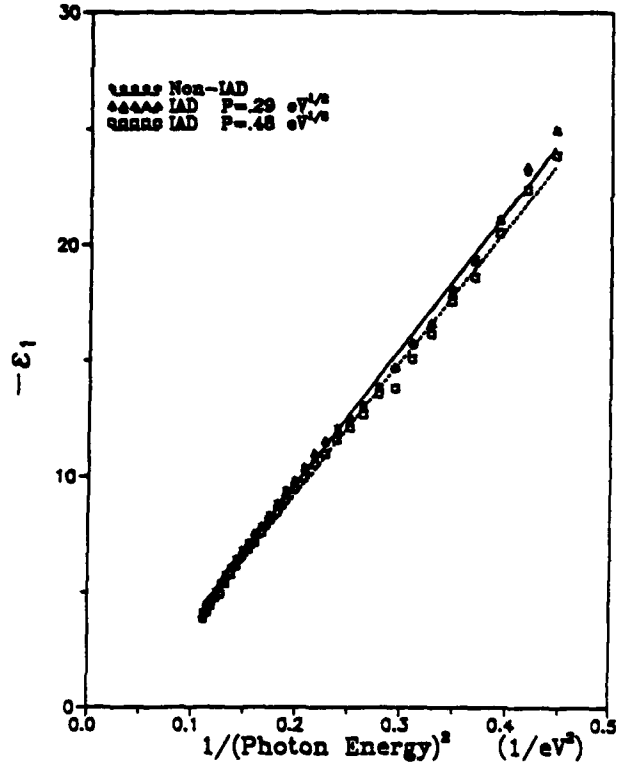


FIG. 8a

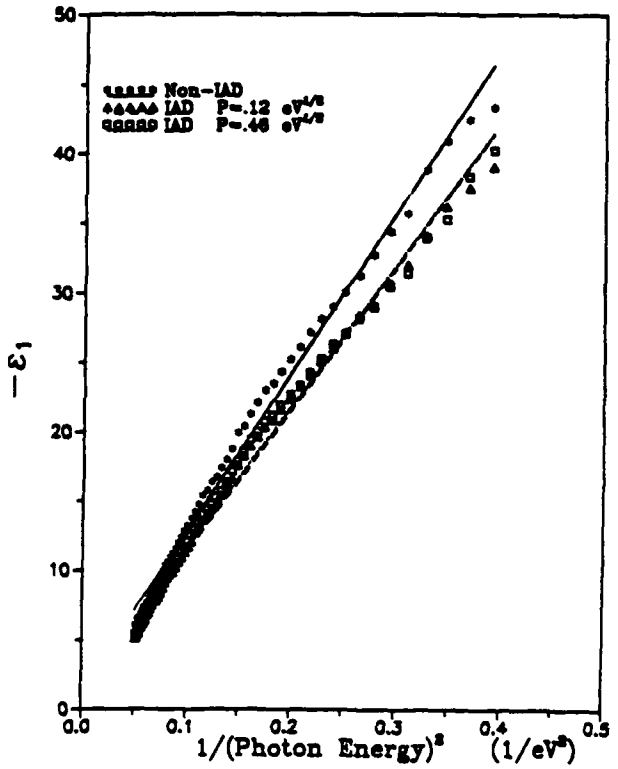


FIG. 8b

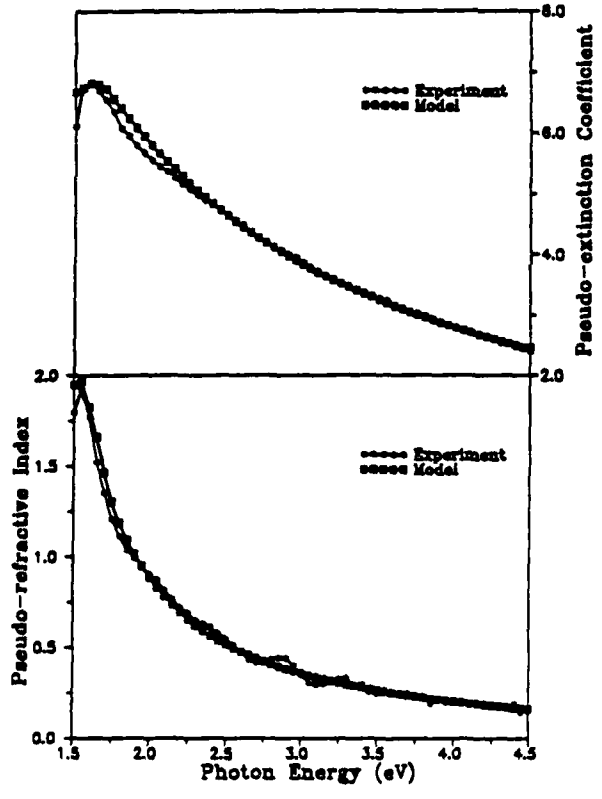


FIG. 9

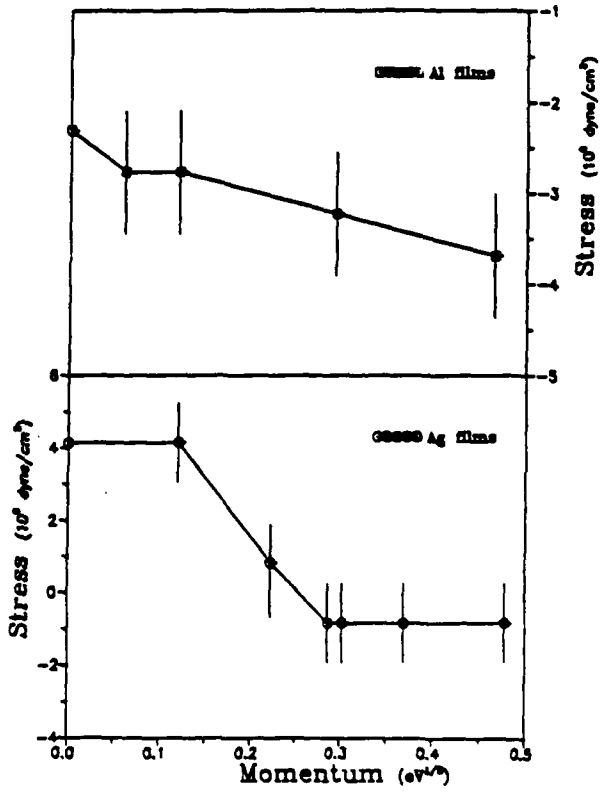


FIG. 10

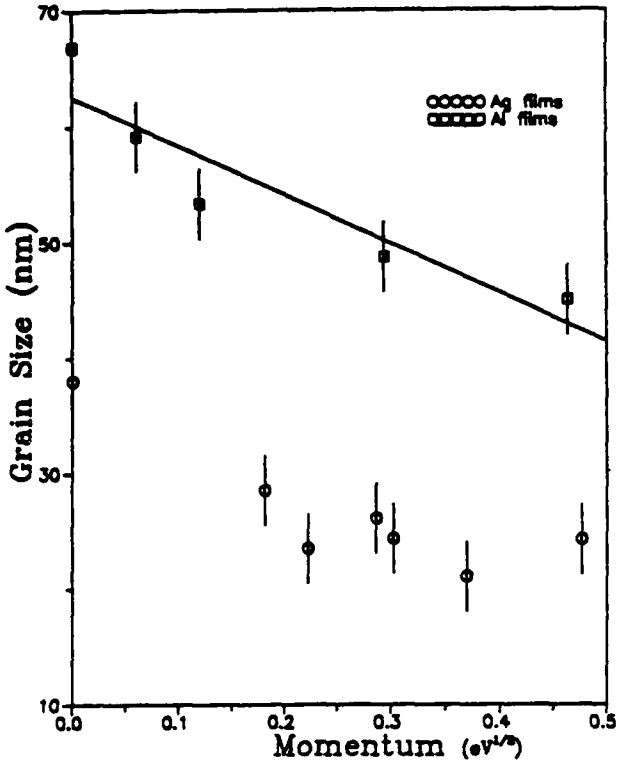


FIG. 11

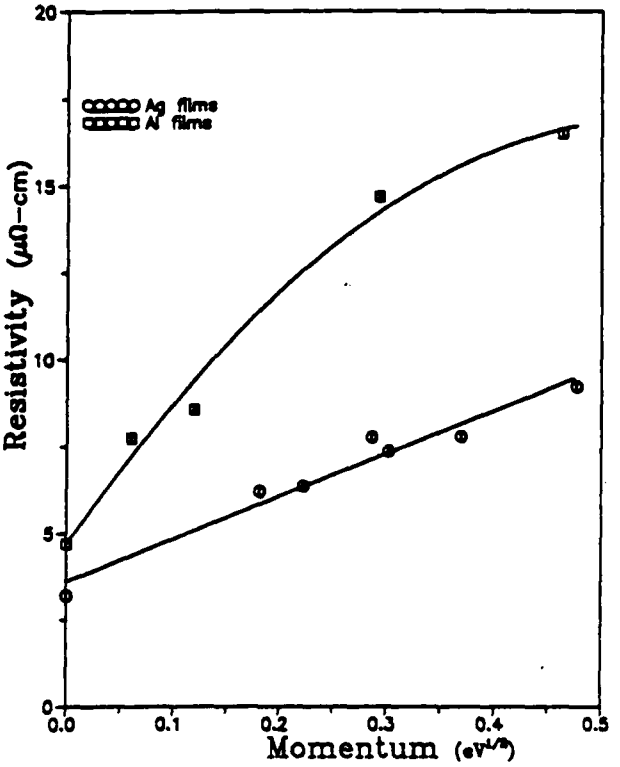


FIG. 12

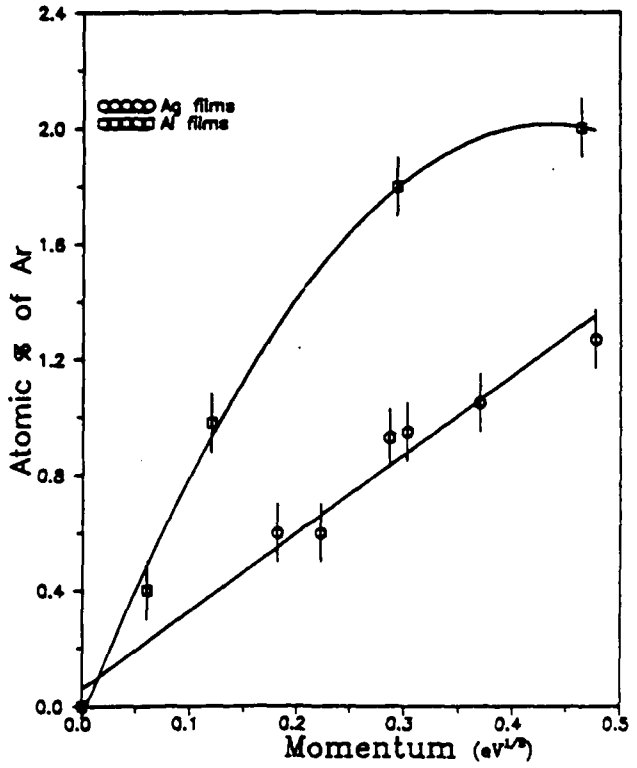


FIG. 13

# APPENDIX C

# Characterization of optical coatings with backscattering spectrometry

J. A. Leavitt, L. C. McIntyre, Jr., M. D. Ashbaugh, B. Dezfouly-Arjomandy, and J. G. Oder

We present three examples to illustrate the use of backscattering spectrometry (utilizing helium analysis beams in the 1.5-5.0 MeV energy range) to determine film stoichiometry, areal density, and impurity levels in optical coatings: 1) a magnesium fluoride coating, 2) a tungsten/silicon multilayer soft x-ray mirror, and 3) a tri-layer optical data-storage film.

---

The authors are with University of Arizona, Department of Physics, Tucson, AZ 85721.

Backscattering spectrometry,[1] utilizing analysis beams of $^4$He ions in the energy range 1.5-5.0 MeV, is an underused technique for determining film thickness, stoichiometry, and impurity levels. The basic technique is illustrated in Fig. 1. Analysis ions rebound from struck target (film) ions to impinge on the detector (subtends solid angle $\Omega$) with energy characteristic of the mass of the struck particle; further, the He ions lose energy passing into and out of the film material. Energy analysis of the backscattered He ions from a film of uniform composition yields a nearly flat-topped "peak" for each element present in the film. The film elements may be identified by the energies ($E_{IC}$, $E_{IB}$) of the high-energy sides of the peaks. Areal density, $(Nt)_i$, in atoms/cm$^2$, may be determined for each element from knowledge of solid angle $\Omega$, cross section $\sigma_i$, and integrated peak count $A_i$ for Q incident analysis ions. Concentration variations appear as variations in the "flatness" of the peak tops. Note that the average stoichiometric ratio, $N_c/N_b$, depends only on the ratio of integrated peak counts, $A_C/A_B$, and knowledge of the scattering cross section ratio, $\sigma_B/\sigma_C$. Cross sections for scattering of 2 MeV $^4$He on all elements are nearly Rutherford (Coulomb's law holds), so Rutherford backscattering (RBS) is an absolute method that does not require the use of standards. Average stoichiometric ratios may be determined as accurately as 0.1% by acquisition of sufficient data, while areal densities are uncertain by about 3%. Conversion of areal density (in atoms/cm$^2$) to physical film thickness (in Å) requires knowledge of film density. Conversely, if the physical thickness is known, areal density measurement will provide film density. Low-mass substrates (such as carbon) are preferred so that the substrate signal does not interfer with the film signals.

We present three examples to illustrate the power of the technique. All backscattering data were acquired at the Ion Beam Analysis Facility[2] at the University of Arizona; a 6 MV Van de Graaff accelerator was the source

of the $^4$He beams.

The first example is a single layer of $MgF_2$, with impurities, laid down with Ar ion-assisted deposition (IAD), as part of a study[3] of the effect of IAD on film packing density and moisture resistance. The RBS data are shown in Fig. 2; stoichiometry and elemental areal densities are given in Table 1. Note the high accuracy of the average stoichiometry, the incorporation of Ar in the film and the replacement of F by the ever-present O. No other impurities are present in signficant amounts. Measurement of physical film thickness (in Å) was made with a WYKO optical profiler and combined with the RBS areal density measurement to produce the film density. The study showed that Ar IAD does produce $MgF_2$ coatings with increased packing density and moisture resistance.

The second example is a tungsten/silicon multilayer soft x-ray mirror[4] consisting of seven layers (56 Å each) of Si alternating with eight layers (28.5 Å each) of W deposited on a carbon substrate by magnetically confined dc sputtering with Ar. The sputtering rates had previously been calibrated by depositing films of sufficient thickness (3000-6000 Å) so that their physical thickness could be accurately measured with a Mirau optical interferometer. The RBS spectrum is shown in Fig. 3. Since the RBS depth resolution is ~100 Å, signals from the individual W and Si layers are not resolved. The film may be treated as a compound film of uniform composition for analysis of W, Si, and Ar; the stoichiometry and elemental areal densities are given in Table 2. Division of the areal density (per layer) by the above physical thicknesses yields film densities of 2.1 g/cm$^3$ for Si and 17.3 g/cm$^3$ for W. The Si density is in the range for amorphous Si, while the W density is 10% below that for bulk. The oxygen impurity in the film is confined to a surface layer less than 100 Å thick; if $WO_3$ of bulk density is assumed, then the $WO_3$ layer is 29 Å thick. More detailed characterization of similar W/Si

multilayers has involved utilization of low-angle x-ray diffraction data with the RBS data in an iterative procedure to determine layer thicknesses, layer densities, and interface roughness for a normal-incidence reflector of ~200 Å radiation.[4,5]

The third example is a tri-layer optical data-storage film composed of a 900 Å magneto-optical rare-earth transition-metal (RE-TM) alloy film sandwiched between passivating layers (3300 Å, 1100 Å) of $Al_2O_3$. Backscattering spectra for incident $^4He$ analysis beams of energies 1.9 and 3.8 MeV are shown in Fig. 4; areal densities and stoichiometries for the three layers as determined from the 3.8 MeV data are given in Table 3. Note that accurate determination of stoichiometry and areal densities from the 1.9 MeV data is probably not possible due to extensive overlap of signals from different elements and different layers. The complexity of this spectrum gives an indication of why ordinary 2 MeV $^4He$ RBS has not been extensively applied to analysis of these multilayers. The 3.8 MeV data of Fig. 4 show non-overlapping signals from all elements in all three layers except the Ar signal in the tail of the TM signal (this overlap is eliminated in 4.7 MeV data, not shown). It is, of course, not necessary to completely eliminate overlapping signals from different elements in different layers. In certain simple cases,[7] reliable results can be obtained by using least-squares-fits to deconvolute the overlapping signals. Use of $^4He$ analysis beams in the high energy (2-5 MeV) region does require use of measured[6] cross sections for scattering of $^4He$ by light elements such as C, N, O, etc., since these cross sections are not Rutherford in this energy region. The uncertainties listed in Table 3 are typical; the accuracy of the average stoichiometric ratio could be improved somewhat by taking more data. This example illustrates the utility of the higher energy $^4He$ analysis beams.

In summary, we have presented three examples that illustrate the use of backscattering spectrometry for determining areal density, stoichiometry, and impurity levels in optical coatings.

This work is supported by the Air Force Office of Scientific Research through the University Research Initiative Program and by the Optical Data Storage Center at the University of Arizona. We are grateful to P. Stoss for providing the $^4$He beams, G. Van Zijll, and Z.-M. Yang for assistance with acquisition and analysis of data, and to C. Falco, F. Fernández, A. Macleod, and M. Messerly for providing samples and stimulating discussions.

References

1. W.-K. Chu, J. W. Mayer, and M.-A. Nicolet, Backscattering Spectrometry (Academic Press, New York, 1978).

2. J. A. Leavitt, Nucl. Instrum. & Methods B24/25, 717 (1987).

3. J. D. Targove, M. J. Messerly, J. P. Lehan, C. C. Weng, R. H. Potoff, H. A. Macleod, L. C. McIntyre, and J. A. Leavitt, Proc. SPIE 678, 115 (1986).

4. C. M. Falco, F. E. Fernández, P. Dhez, A. Khandar-Shahabad, L. Névot, B. Pardo, and J. Corno, Proc. SPIE 733, 343 (1986).

5. F. E. Fernández, C. M. Falco, P. Dhez, A. Khandar-Shahabad, L. Névot, B. Pardo, J. Corno, and B. Vidal, Appl. Phys. Lett. 51, 880 (1987).

6. J. A. Leavitt, P. Stoss, D. B. Cooper, J. L. Seerveld, L. C. McIntyre, Jr., R. E. Davis, S. Gutierrez, and T. M. Reith, Nucl. Instrum. & Methods B15, 296 (1986).

7. L. C. McIntyre, Jr., M. D. Ashbaugh, and J. A. Leavitt, Mat. Res. Soc. Symp. Proc. 93, 401 (1987).

**Table 1. Results of RBS Analysis of the $MgF_2$ Optical Coating.**

| Element | Nt* | Atomic % |
|---|---|---|
| Mg | 17.8 ± 0.6 | 34.1 ± 0.4 |
| F | 31.2 ± 1.0 | 59.9 ± 0.4 |
| O | 2.2 ± 0.1 | 4.2 ± 0.2 |
| Ar | 0.93 ± 0.04 | 1.80 ± 0.10 |
| W | 0.08 ± 0.01 | < 0.1 |

*Nt = Atoms/$cm^2$ x $10^{16}$

**Table 2. Results of RBS Analysis of the W/Si Multilayer.**

| Element | Nt* | Atomic % |
|---|---|---|
| W | 12.7 ± 0.4 | 41.4 ± 0.3 |
| Si | 17.7 ± 0.6 | 57.5 ± 0.3 |
| Ar | 0.32 ± 0.04 | 1.00 ± 0.10 |
| O† | 0.16 ± 0.02 | — |

*Nt = Atoms/cm$^2$ x $10^{16}$.

†O in surface layer only.

**Table 3. Results of RBS Analysis of the Optical Data Storage Tri-Layer.**

| Layer | Element | Nt* | Atomic % | Ratio |
|---|---|---|---|---|
| 1 | Al | 14.8 ± 0.4 | 38.9 ± 0.6 | $N_O/N_{Al}$ = 1.51 ± 0.04 |
| | O | 22.3 ± 0.8 | 58.6 ± 0.7 | |
| | Ar | 0.9 ± 0.2 | 2.5 ± 0.3 | |
| 2 | RE | 1.13 ± 0.03 | 17.4 ± 0.6 | $N_{RE}/(N_{RE}+N_{TM})$ = 0.199 ± 0.001 |
| | TM | 4.56 ± 0.13 | 70.3 ± 0.6 | |
| | Ar | 0.80 ± 0.17 | 12.3 ± 1.8 | |
| 3 | Al | 4.8 ± 0.2 | 38.2 ± 0.9 | $N_O/N_{Al}$ = 1.57 ± 0.06 |
| | O | 7.5 ± 0.3 | 59.8 ± 1.0 | |
| | Ar | 0.25 ± 0.10 | 2.0 ± 0.6 | |

*Nt = Atoms/cm$^2$ x $10^{16}$.

FIGURE CAPTIONS

Fig. 1. Production of the backscattering spectrum for a two-element compound film on a low-mass substrate and determination of areal density, Nt, and stoichiometric ratio, $N_c/N_b$.

Fig. 2. The 1.9 MeV $^4$He backscattering spectrum of a 620 Å magnesium fluoride coating on a carbon substrate. The film was manufactured by electron-beam evaporation with Ar ion-assisted deposition. Data acquisition time was five minutes.

Fig. 3. The 1.9 MeV backscattering spectrum of a 620 Å tungsten/silicon multilayer deposited on a carbon substrate by dc-sputtering with argon. The same data are shown with different vertical scales in a) and b). Data acquisition time was five minutes.

Fig. 4. Backscattering spectra of a 5300 Å rare-earth transition-metal optical data-storage tri-layer, $Al_2O_3$/(RE-TM)/$Al_2O_3$, deposited on a carbon substrate by Ar sputtering, for incident $^4$He analysis beams of energies a) 1.9 MeV and b) 3.8 MeV. Data acquisition time was less than ten minutes per spectrum. The numbers in parentheses are layer numbers, with layer 1 at the surface.

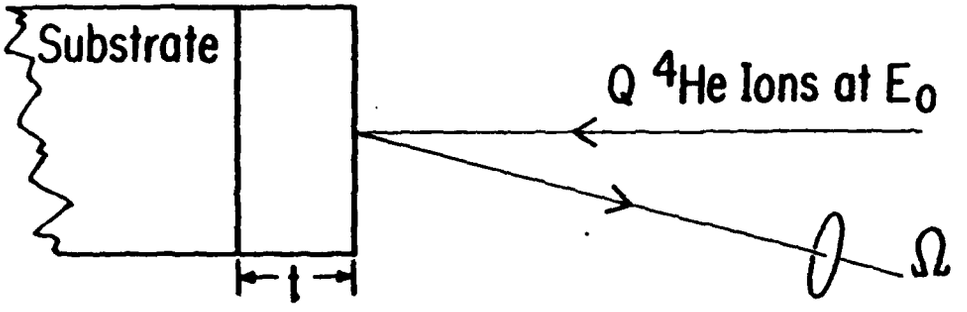


$$(Nt)_i = \frac{A_i}{Q\Omega\sigma_i}$$

$$\frac{c}{b} = \frac{N_c}{N_b} = \left(\frac{A_c}{A_B}\right)\left(\frac{\sigma_B}{\sigma_c}\right)$$

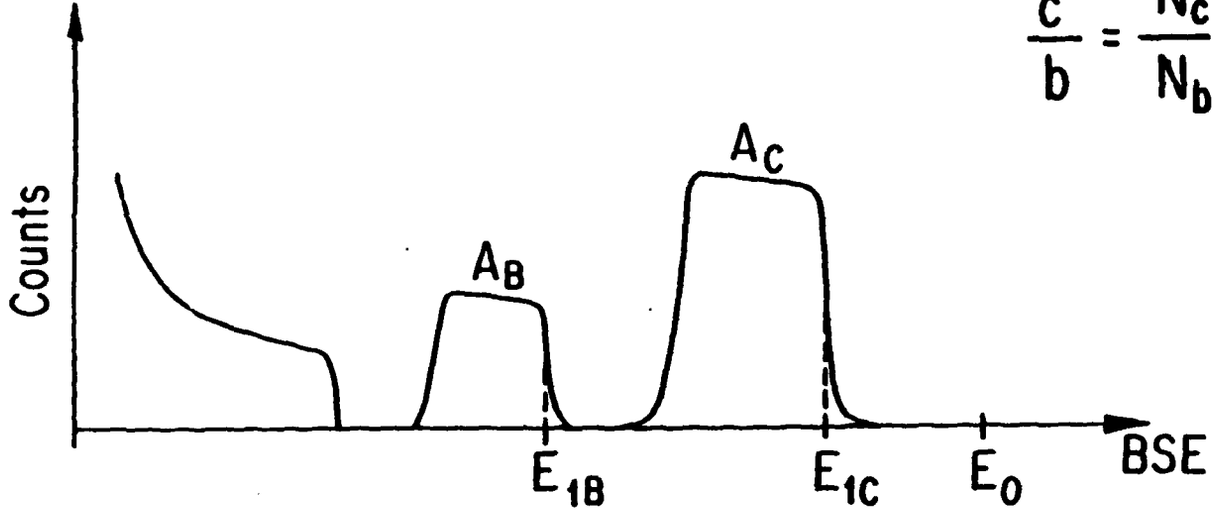


Fig. 1

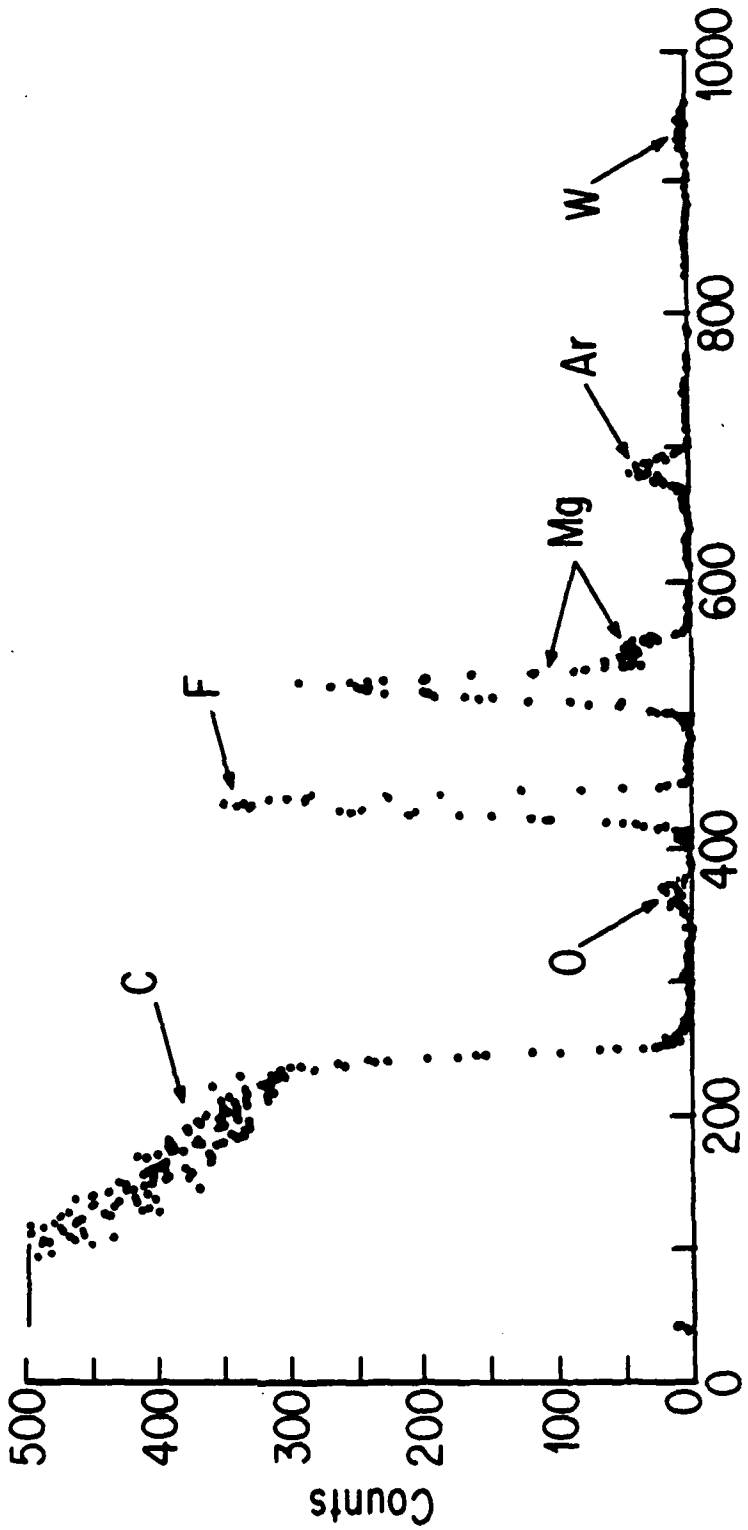
Counts
500
400
300
200
100
0
0
200
400
600
800
1000
Channel Number
C
O
F
Mg
Ar
W

Fig. 2

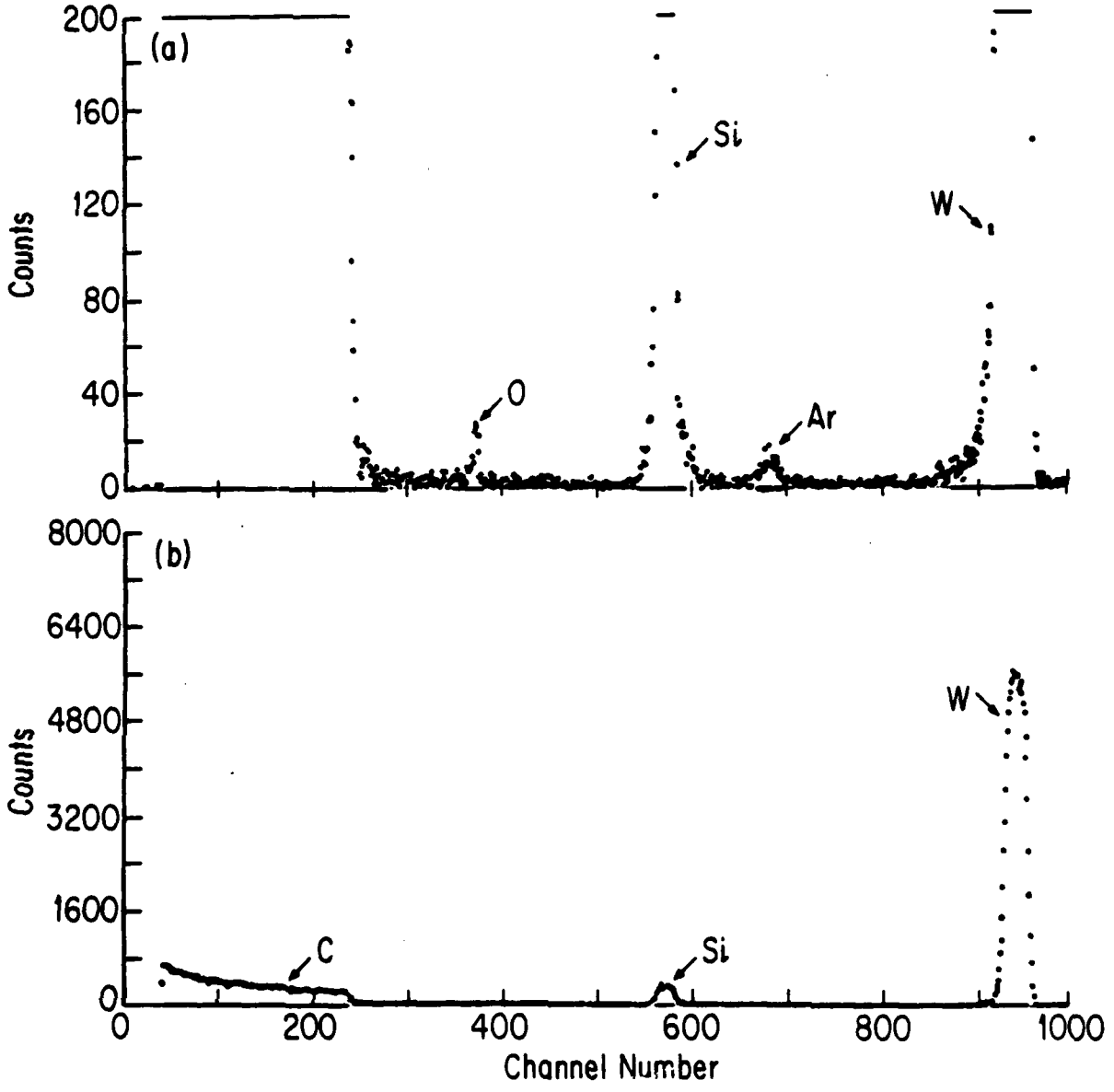
200
(a)
160
120
80
40
0
Counts
Si
W
O
Ar
8000
(b)
6400
4800
3200
1600
0
Counts
W
C
Si
0
200
400
600
800
1000
Channel Number

Fig. 3

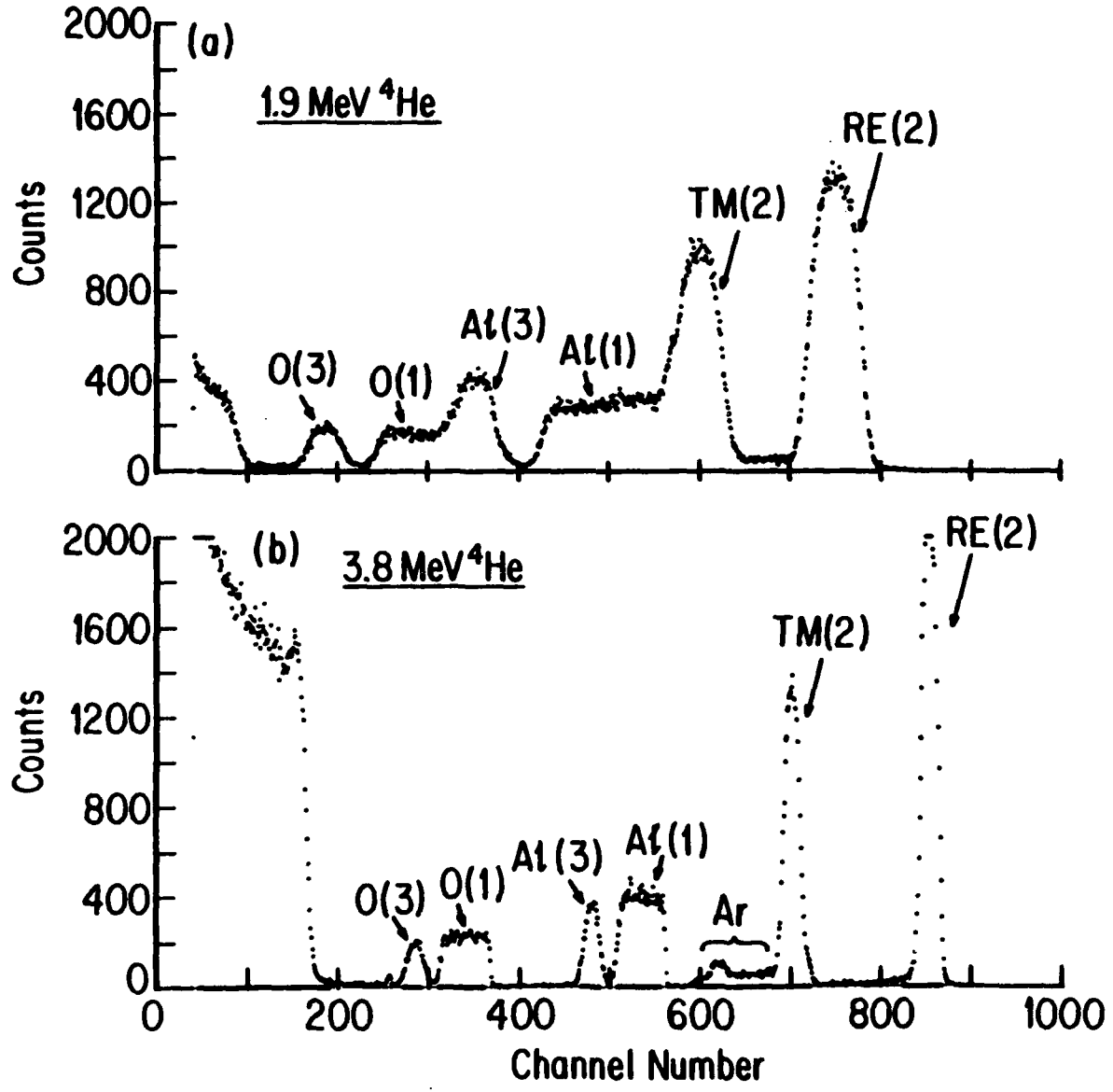
(a)
1.9 MeV $^4$He
Counts
2000
1600
1200
800
400
0
O(3)
O(1)
Al(3)
Al(1)
TM(2)
RE(2)
(b)
3.8 MeV $^4$He
Counts
2000
1600
1200
800
400
0
O(3)
O(1)
Al(3)
Al(1)
Ar
TM(2)
RE(2)
0
200
400
600
800
1000
Channel Number

Fig. 4

# APPENDIX D

# A CONTINUUM MODEL OF THIN FILM DEPOSITION AND GROWTH

Andrew J. Bernoff
Department of Mathematics
University of Arizona, Tucson AZ 85721

Seth Lichter
Aerospace and Mechanical Engineering Department
University of Arizona, Tucson AZ 85721

October 10, 1988

## ABSTRACT

A continuum theory for the deposition and growth of solid films is presented. The theory is developed in a coordinate independent manner and so incorporates the fully nonlinear physics. The evolution of the film is modelled in three steps. First, the adsorption of atoms in the incident beam is modelled as a ballistic process. Second, the random motion of the adatoms is treated as a diffusive process. Finally, sticking of adatoms to the film occurs as a Poisson process. The resulting system of differential equations is examined in several parameter limits. The diffusively dominated limit appears similar to zone I of the structure-zone model. Generically the surface slope develops discontinuities; these 'kinks' play the role of grain boundaries. In the ballistically dominated case these kinks may be advected along the surface giving rise to columnar like microstructure.

# I. INTRODUCTION

While some features of film morphology are correlated to substrate temperature by Movchan and Demchishin's (1969) structure zone model, prediction of film properties (such as film density, rate of growth, column size) from deposition conditions is an actively pursued goal for both theoretical interest and technological importance. Past research has concentrated on explaining the microscopic dynamics of individual adatoms. Computer simulations serially deposit spheres or disks onto previously deposited particles to simulate the arriving beam flux. The adatoms then move over the surface according to some hopping algorithm. Continuum-like models also explicitly include microscopic variables such as adatom size. (See Bartholomeusz et al. (1987) for a review of previous research.)

In this paper the properties on the large scale are obtained by averaging over an ensemble of individual particles passing through a control volume on the surface. The local analysis is performed in a coordinate independent fashion; consequently the local balance then yields deposition equations in general coordinates that have the advantage of being fully nonlinear on the macroscopic scale. A simple ballistic argument yields a scattering cross-section which determines the number of adatoms that are added to the surface layer and their velocity along the surface. The present paper attempts to track an atom from the beam until it is fixed to the film: it incorporates both a model of the initial collision with the interface and the adatom's mobility on the surface. It is hoped that this more comprehensive viewpoint will eventually explain a number of morphological features. In this paper some basic analysis of pertinent limiting cases is considered; a comprehensive categorization of behavior over the full parameter range is left for future efforts. In Section II the physical mechanisms are identified and incorporated into a mathematical formulation. An analysis of this model is presented in Section III. Results and comparison with experiment is in Section IV. In the appendix details of the ballistic cross-section are presented.

## II. FORMULATION

In this section a local analysis of the adatom dynamics is used to deduce the deposition equations. The formulation incorporates the effects of incoming momentum, adatom motion including convection and diffusion, and sticking. The incoming beam is assumed to be unidirectional and uniform. The incident atoms hit the substrate, and a portion of them join a loosely bound surface layer. A ballistic argument determines the portion of the beam flux which is not reevaporated. The flux rate onto a particular portion of the surface is then dependent upon the surface's orientation (Dirks and Leamy, 1977). The adatoms in this surface layer then move by convection and surface diffusion until they eventually stick leading to accretion of the deposited film. Bulk diffusion is ignored. Finally, adhering to the surface is modelled as a Poisson process and that consequently the deposition rate is proportional to the adatom concentration.

A length and time scale are chosen such that the variation on the substrate is initially order unity. Consider a location on the surface, $\vec{p}$, and let the normal at this point be denoted by $\hat{n}$ (Figure 1a). The incident adatom flux, $\vec{J}$, will be assumed to be in a direction, $\hat{J}$ and of intensity $J$,

$$\vec{J} = J\hat{J}. \tag{2.1}$$

Moreover, the magnitude of the incident velocity, $V$, will also be assumed to be constant.

As the atoms strike the surface some of them will be reflected off the surface, and some will be adsorbed into the surface layer. In the appendix this process is examined in detail; here only two properties of the adatoms adsorbed at each point need to be known in detail, the angular flux density of adatoms, $J_\psi$, and the mean velocity of the adsorbed adatoms $V_\psi$. Define a polar angle $\psi$ in the tangent plane and a corresponding unit vector $\hat{\psi}$. Then $J_\psi$ is the flux density per unit radian and $V_\psi$ is the mean velocity of the adatoms leaving in the $\hat{\psi}$ direction after collision.

The adatom travels along the surface in the $\hat{\psi}$ direction until it collides with another

adatom or some local surface feature. The occurence of this second collision is a Poisson distributed process with timescale $1/\gamma$. The length travelled before the second collision is then of order $V/\gamma$. The case when both these scales are small in comparison to the characteristic scales of the surface is considered, that is

$$\frac{1}{\gamma}, \frac{V}{\gamma} \ll 1. \tag{2.2}$$

Before the adatom undergoes a second collision, its velocity is determined by the scattering angle; consequently, this population of adatoms will be called coherent. After the adatom has undergone a second collision, it will be assumed that it is scattered randomly. This population will be referred to as incoherent.

The equation of motion for the density of coherent adatoms, $c$, can now be computed by considering the flux balance in a small region, $\mathcal{A}$, of the surface. Denote the edge as $\sigma$ and the normal to the edge in the surface as $\hat{\eta}$ (figure 1b). Then the flux balance yields

$$\partial_t \left\{ \int_{\mathcal{A}} c \, d\mathcal{A} \right\} = \int_{\mathcal{A}} J_n \, d\mathcal{A} - \gamma \int_{\mathcal{A}} c \, d\mathcal{A} + \oint_\sigma d\sigma \int_0^{2\pi} d\psi (\hat{\psi} \cdot \hat{\eta}) \mathcal{F}_\psi(\vec{p}(\sigma)). \tag{2.3}$$

Here the left hand side of (2.3) is the time rate of change of the volume of adatoms in $\mathcal{A}$. The terms on the right hand side are the flux through the top of $\mathcal{A}$, the loss due to deflection, and the flux through the edge of $\mathcal{A}$, respectively. The adsorbed flux density, $J_n$, at a given point on the surface, $\vec{p}$, can be computed by summing the fluxes scattered on the surface through all angles,

$$J_n(\vec{p}) = \int_0^{2\pi} d\psi J_\psi(\vec{p}), \tag{2.4}$$

and the incident flux adsorbed through the upper surface is then given by integrating $J_n$ over $\mathcal{A}$. The second term represents the loss of flux through deflection. This is modelled as a Poisson process; consequently the time rate of loss of coherent adatoms is just a constant fraction, $\gamma$, of the population. The last term in (2.3) represents the flux of adatoms through the edge, $\sigma$, computed by integrating the surface flux due to adatoms moving in a particular

orientation through a boundary element. The flux of adatoms moving in the $\hat{\psi}$ direction at a point on the boundary $\vec{p}(\sigma)$ can be computed as

$$\mathcal{F}_\psi(\vec{p}(\sigma)) = \int_0^\infty dr J_\psi(\vec{p}(\sigma) - r\hat{\psi}, t - t')e^{-\gamma t'}, \tag{2.5}$$

where the integrand is the contribution to the flux from a point a distance $r$ in the $-\hat{\psi}$ direction. The exponential term is the probability that a particle remains in the coherent population after a time $t'$. The particles which strike the surface at a point, $\vec{p} - r\hat{\psi}$, will arrive at the location $\vec{p}$ at time $t'$ if

$$r = V_\psi t'. \tag{2.6}$$

Using the restrictions (2.2) the integral (2.5) can be evaluated to leading order as

$$\mathcal{F}_\psi(\vec{p}(\sigma)) \approx \int_0^\infty dt' V_\psi(\vec{p}(\sigma), t) J_\psi(\vec{p}(\sigma), t) e^{-\gamma t'} = \frac{1}{\gamma} V_\psi(\vec{p}(\sigma), t) J_\psi(\vec{p}(\sigma), t), \tag{2.7}$$

Applying the divergence theorem to equation (2.3), and letting $\mathcal{A}$ shrink to a small area yields the flux balance,

$$c_t = J_n - \gamma c - \frac{1}{\gamma} \nabla_s \cdot (\vec{V}_a J_n), \tag{2.8}$$

where the average velocity $\vec{V}_a$ has been defined as

$$\vec{V}_a = \frac{\int_0^{2\pi} d\psi J_\psi V_\psi \hat{\psi}}{J_n}. \tag{2.9}$$

The subscript $s$ on the vector operators is to indicate that they are acting along the surface defined by $\vec{p}$. The quantities $J_n$ and $\vec{V}_a$ are determined by the particular model used for ballistic scattering. These quantities are computed for various cases in the appendix.

Applying (2.2) shows that at leading order the solution to (2.8) is

$$c(\vec{p}, t) = \frac{1}{\gamma} J_n \tag{2.10}$$

which can be interperted physically as the incident flux times the average time to deflection of an adatom.

Equation (2.8) describes the evolution of $c$ due to the coherent motion of ballistic scattering. The incoherent motion of adatoms caused by random scattering on the surface must also be included. It will be assumed that after an adatom in the surface layer is deflected that the orientation of its velocity is determined randomly. Consequently, the motion of the particle can be modelled as a diffusive process.

The rate at which particles leave the coherent adatom concentration is $\gamma c$; they then become part of an incoherent adatom density $d$. Adatoms are removed from the incoherent state by sticking to the surface; this is again assumed to be a Poisson process with a mean lifetime $1/\gamma'$. The equation of motion for $d$ is now given by

$$d_t = \gamma c - \gamma' d + \nu \nabla_s^2 d, \tag{2.11}$$

where $\nu$ is a diffusion constant.

As adatoms are deposited, the surface grows outward along its normal in proportion to the rate of deposition,

$$\vec{p}_t = \gamma' d \hat{n}. \tag{2.12}$$

This equation together with (2.8) and (2.11) specify the evolution of the surface.

To summarise, the adatom motion on the surface is due to a component which depends on the direction of the incident flux plus a randomly oriented diffusive component. The flux rate of particles which ultimately stick on the surface is given by $J_n$ and will be determined in the appendix by considering the collision of an incident particle with the surface. The model equations governing the process of film growth are

$$c_t = J_n - \gamma c - \frac{1}{\gamma} \nabla_s \cdot (\vec{V}_a J_n), \tag{2.13a}$$

$$d_t = \gamma c - \gamma' d + \nu \nabla_s^2 d, \tag{2.13b}$$

$$\vec{p}_t = \gamma' d \hat{n}, \tag{2.13c}$$

where

$\vec{p}$ = location of the surface

$\hat{n}$ = surface normal

$c$ = coherent adatom volume density

$d$ = incoherent adatom volume density

$J_n$ = adsorbed adatom flux

$\vec{V}_a$ = average adsorbed adatom velocity

$1/\gamma$ = coherent adatom deflection rate

$1/\gamma'$ = incoherent adatom sticking rate

$\nu$ = incoherent adatom diffusion constant

## III. ANALYSIS

### A. Conservation of integrated flux

In this section it is shown how the integrated adsorbed incident flux relates to the integrated flux in the coherent and incoherent adatom populations and the increase in volume of the film. By considering the total incident flux onto the surface it is possible to determine an expression for the rate of growth of the film. Consider a domain, $\mathcal{A}$, with periodic or no-flux boundary conditions. Define the volume of previously deposited film below $\mathcal{A}$ as $\mathcal{V}$. Similarly, define the volume of incoherent and coherent adatoms on the surface as

$$\int_{\mathcal{A}} c \, dS = \mathcal{C}, \tag{3.1a}$$

$$\int_{\mathcal{A}} d \, dS = \mathcal{D}, \tag{3.1b}$$

respectively, where $dS$ is an element of surface area.

Integrating equation (2.13a) over the surface relates the total adsorbed incident flux,

$$\mathcal{J} = \int_{\mathcal{A}} J_n dS, \tag{3.2}$$

to the evolution of $\mathcal{C}$,

$$\mathcal{C}_t + \gamma\mathcal{C} = \mathcal{J}. \tag{3.3}$$

Similarly integrating (2.13b) relates the evolution of $\mathcal{C}$ and $\mathcal{D}$,

$$\mathcal{D}_t + \gamma'\mathcal{D} = \gamma\mathcal{C}. \tag{3.4}$$

Finally the time rate of change of the volume of the film can be related to the sticking of incoherent adatoms by dotting (2.13c) into the surface normal and integrating over the surface,

$$\mathcal{V}_t = \gamma'\mathcal{C}. \tag{3.5}$$

The conservation of total mass can now be obtained by adding (3.3,4,5) together,

$$\partial_t(\mathcal{C} + \mathcal{D} + \mathcal{V}) = \mathcal{J}. \tag{3.6}$$

Equations (3.3-3.6) demonstrate how the incident flux cascades through the various stages of the model. They allow the mean growth rate of the thin film to be determined as a function of the integrated adsorbed flux.

B. Diffusion Dominated Dynamics

In this section the case when diffusion dominates the evolution of the interface will be considered. The mean diffusion length, $L_d$, of an incoherent adatom can be approximated by considering (2.13b),

$$L_d = \left(\frac{\nu}{\gamma'}\right)^{1/2}. \tag{3.7}$$

Suppose the surface microstructure varies on a scale that is small compared to the diffusion length, that is $L_d \gg 1$. In this case diffusion will be the dominant surface process. Equation (2.13b) will relax towards an equilibrium where $\nabla_s d$ is zero, that is a state where the concentration of $d$ is uniform on the surface. This implies

$$d \approx \frac{\mathcal{D}}{\mathcal{A}}. \tag{3.8}$$

Solving (3.4) now yields

$$d(t) \approx \frac{1}{\mathcal{A}} \int_{-\infty}^{t} \gamma \mathcal{C} e^{-\gamma' t'} dt', \tag{3.9}$$

or applying (2.10),

$$d(t) \approx \frac{1}{\mathcal{A}} \int_{-\infty}^{t} \mathcal{J} e^{-\gamma' t'} dt'. \tag{3.10}$$

In the limit when $\mathcal{J}_t/\mathcal{J} \gg \gamma'$ this reduces to

$$\gamma' d \approx \frac{\mathcal{J}}{\mathcal{A}}. \tag{3.11}$$

which is simply the average adsorbed flux.

If we define a new time scale,

$$\tau = \int_0^t \gamma' d \, dt, \tag{3.12}$$

equation (2.13c) takes a particularly simple form

$$\vec{p}_\tau = \hat{n}. \tag{3.13}$$

Physically, the surface grows at a constant rate in the direction of its normal. In the limit defined by (3.11) the rate of growth is simply the average adsorbed flux rate. Equation (3.13) is an eikonal equation that commonly arises when considering the rays of a wave equation and can be solved implicitly with the method of characteristics (Whitham, 1974).

It will be convenient to introduce a coordinate system for equations (2.13); define the surface elevation, $p$, measured above some plane with cartesian coordinates $x_i = (x, y)$, then

$$\vec{p} = (x, y, p(x, y, t)). \tag{3.14}$$

Equation (2.13c), which gives a Lagrangian description of the interface, can be converted to an Eulerian description. The normal at a point on the surface is given by

$$\hat{n} = \frac{1}{(1 + p_x^2 + p_y^2)^{1/2}} (-p_x, -p_y, 1). \tag{3.15}$$

If we denote by a dot the time derivative in the Lagrangian coordinate, the chain rule yields

$$p_\tau = \dot{p} + p_x \dot{x} + p_y \dot{y}, \tag{3.16}$$

which after using (3.13) yields

$$p_\tau = (1 + p_x^2 + p_y^2)^{1/2}. \tag{3.17}$$

Following Whitham (1974) an implicit solution to the initial value problem (3.17) can be found. It will be convenient in what follows to use index notation with the summation convention; define the gradient $\partial_i = (\partial_x, \partial_y)$. Suppose initially,

$$p(x_i) = P(x, y) \quad \text{at} \quad \tau = 0. \tag{3.18}$$

Then at a later time $t$ the solution at a point $\check{x}_i = (\check{x}, \check{y})$ can be found in terms of $P(x, y)$,

$$p(\check{x}, \check{y}, \tau) = P(x, y) + \frac{\tau}{(1 + \partial_k P \partial_k P)^{1/2}}, \tag{3.19}$$

where $\check{x}_i$ is defined implicitly as a function of $x_i$ and $\tau$,

$$\check{x}_i = x_i - \frac{\tau \partial_i P}{(1 + \partial_k P \partial_k P)^{1/2}}. \tag{3.20}$$

The implicit solution (3.20) allows some explicit special solutions; in particular, a plane will grow with a unit velocity normal to its surface and a spherical cap will remain spherical with a constantly increasing radius.

Because (3.20) is an implicit solution corresponding to characteristics, it admits the possibility of multivalued solutions. To determine if and when this happens it is necessary to decide if (3.20) provides a continuous bijection from $x_i$ to $\check{x}_i$. This will be the case if the Jacobian, $Q$, between the two coordinates is always non-zero. Using (3.20) to compute the Jacobian yields the determinant

$$Q = \left| \frac{\partial \check{x}_i}{\partial x_j} \right| = |\delta_{ij} - \tau M_{ij}| \tag{3.21}$$

where the $\delta_{ij}$ is the Kronecker delta function and

$$M_{ij} = \frac{\partial_{ij}P(1+\partial_k P\partial_k P)^{1/2} - \partial_i P\ \partial_k P\ \partial_{jk}P}{(1+\partial_k P\partial_k P)^{3/2}}. \tag{3.22}$$

To understand (3.22) requires a basic knowledge of differential geometry (Do Carmo, 1976). The determinant and trace of $M_{ij}$ are the *Gaussian curvature* and twice the *mean curvature* respectively. This implies that the eigenvalues of $M_{ij}$ are exactly the *principal curvatures*, $\kappa_1, \kappa_2$ of the surface. Geometrically $1/\kappa_1, 1/\kappa_2$ correspond to the maximum and minimum radius of the osculating circle at a point on $P$. From (3.21) it follows that $Q$ will vanish when

$$\tau = \min_{\{x_i\}}\left(\frac{1}{\kappa_1}, \frac{1}{\kappa_2}\right) \tag{3.23}$$

Note that if $\kappa_1, \kappa_2$ are never greater than zero, the initial condition is convex, and the solution never breakdowns. However, if the initial condition is non-convex anywhere, at least one of the curvatures will be positive and the solution will eventually break down.

The form of this breakdown can be deduced by noting that the gradient of (3.17) is a first order semi-linear hyperbolic system for $\partial_i p$. Consequently the gradient will develop shocks (discontinuities) and $p$ will develop 'kinks' (discontinuities in the derivative of $p$). In two dimensions these kinks will occur at isolated points; in three dimensions they will occur on curves on the surface. A description of the motion of these kinks is needed for (3.17) to provide a complete description of the dynamics. Fortunately, physical insight provides a unique solution for the motion of the kinks. The equations are invariant under multiplying $x_i$, $p$ and $\tau$ by a constant; from this it follows that the velocity is dependent only on the slope of the tangent plane on each side of the kink. The isotropy of space now implies that the kink must propagate along the angle bisector of the dihedral angle formed by the tangent planes at the kink (figure 2). This rule together with the characteristic description given by (3.19,20) is sufficient to describe the dynamics. A sample numerical evolution of a two dimensional initial condition is shown in figure 3.

In three dimensions other phenomena can occur; the kinks correspond to boundaries

between grains. If the evolution from an initial condition corresponding to a rough substrate is considered, various bifurcations can occur. The initial appearance of the kink will still occur at a point corresponding to the highest curvature of a concavity. After formation the kink will become a line of discontinuity. Pairs of lines of kinks can collide creating triple points where three grains meet (figure 4). These triple points can also occur by the appearance of a new discontinuity in curvature transverse to an existing line of kinks. The evolution of this triple conjunction is again easily prescribed; it must propagate along the line given by the intersection of the angle bisectors of the three dihedral angles created by the tangent planes at the point. In this way an initially variable topograghy will lead to a system of kinks connected at triple points, resembling the networks of grains seen in thin film growth.

C. Ballistic Dominated Dynamics

A second special case of interest is when ballistic effects dominate the effect of diffusion. The limit considered here is when the diffusion length is much smaller than the characteristic length in the problem, that is $L_d \ll 1$. In addition, it will be assumed that the deposition time is short compared to the the surface growth rate, that is $1/\gamma' \ll 1$. In this case, at leading order

$$\gamma' d \approx \gamma c \approx J_n. \tag{3.24}$$

Equation (2.13c) now reduces to

$$\vec{p}_t = J_n \hat{n}. \tag{3.25}$$

It will be convenient to consider a two dimensional evolution for equation (3.25). Following (3.14) define the height of the surface as

$$\vec{p} = (x, y, p(x,t)), \tag{3.26}$$

where the dependence of $p$ on $y$ has been suppressed. In addition, it is more illuminating to introduce $\phi$, defined as the angle the surface normal makes with the direction of incoming

flux. It will be assumed that $\hat{J} = -\hat{z}$, which implies

$$cos\phi = -\hat{J} \cdot \hat{n} = \frac{1}{(1+p_x^2)^{1/2}}. \tag{3.27}$$

Equation (3.27) and the restriction that $\phi$ is positive when the slope of $p$ is positive specify $\phi$ in terms of $p$.

The assumption $\hat{J} = -\hat{z}$ is not at all restrictive; the isotropy of our formulation guarantees that looking at vertical flux on a slanted surface is identical to looking at flux incident from the same angle on a flat surface. Using (3.27), $p$ can be eliminated in favor of $\phi$ in equation (3.25),

$$\phi_t = cos^2(\phi)\partial_x(J_n sec(\phi)), \tag{3.28}$$

From the ballistic results in the appendix, it is clear that $J_n$ depends only on $\phi$, so equation (3.28) can be rewritten as

$$\phi_t + U(\phi)\phi_x = 0. \tag{3.29}$$

where

$$U(\phi) = -((J_n)_\phi cos(\phi) + J_n sin(\phi)) \tag{3.30}$$

Equation (3.29) is a wave equation. Any initial condition with a variation in $\phi$ and $U$ should cause the formation of shocks. Note that a shock corresponds to a discontinuity in $\phi$; from (3.27) it follows that this corresponds to a kink in the surface of the film as described by $\vec{p}$.

Figure 5 shows $U$ graphed for various ballistic models. Physical symmetry implies that the velocity is an antisymmetric function of $\phi$. It is curious to note that in the three dimensional hard sphere case that $U$ is zero, and equation (3.29) corresponds to growth at a constant rate towards the source. For the other three dimensional cases note that $U$ is negative for $\phi > 0$, and decreases to a minimum and tends to zero as $\phi$ tends to $\pi/2$. For the two dimensional case hard sphere $U$ changes sign; this will lead to qualitatively different dynamics. This should be taken as a caution against using two dimensional ballistic models.

When equation (3.29) becomes invalid due to shock formation, it is essentially because of the formation of high gradients in $\phi$. Because derivatives become large, higher order terms in the equation become important. This will lead to a regularization of the wave equation.

The next higher order contributions due to corrections to (3.24) can easily be computed. Substituting (3.24) into (2.20) yields

$$\gamma' d \approx J_n + \nu \nabla_s^2 d - d_t - c_t - \frac{1}{\gamma} \nabla_s \cdot (\vec{V}_a J_n) \tag{3.31}$$

which resubstituting (3.24), and using (3.27) and (3.29) yields

$$\gamma' d \approx J_n + \left[ \left( \frac{1}{\gamma'} + \frac{1}{\gamma} \right) U(J_n)_\phi - \frac{cos(\phi)}{\gamma} \partial_\phi (\vec{V}_a J_n) \right] \phi_x - \frac{\nu}{\gamma'} cos(\phi) \partial_x \left( cos(\phi) \partial_x (J_n) \right). \tag{3.32}$$

The second and third terms on the right hand side represent corrections to the approximation made by (3.24). By balancing the leading order term $J_n$ against each of these terms the shock width produced by each of the regularizations can be deduced. Note that the second term has a single $x$ derivative; it corresponds to a dissipative regularization. This term becomes important on the shock lengthscale $L_s$ which is dimensionally approximated by

$$L_s \sim J_n \left( \frac{1}{\gamma} + \frac{1}{\gamma'} \right) + \frac{V}{\gamma}. \tag{3.33}$$

Note that in general this scale is on the order the ballistic scattering distance; consequently the arguments used to derive (2.13a) are no longer valid. If this term leads to the regularization, a detailed examination of the ballistic effects in this region will be needed.

If the third term in (3.32) leads to the regularization of the shock, the shock width $L_s'$ will be

$$L_s' \sim \left( \frac{\nu}{\gamma} \right)^{1/2} = L_d \tag{3.34}$$

which is exactly the diffusion length! Note that the term has two $x$ derivatives corresponding to a dispersive regularization.

To understand qualitatively the dynamics of these two regularization the special case $\phi$ is nearly constant is considered. Let

$$\phi(x,t) = \phi_0 + \epsilon\Phi(x,t) \tag{3.31}$$

where $\epsilon \ll 1$. Consider a change of variables into a frame moving at the phase velocity $U(\phi_0)$, and on a slow time scale,

$$X = x - U(\phi_0)t, \tag{3.35a}$$

$$T = \epsilon t, \tag{3.35b}$$

Then equation (3.29) can be expanded as

$$\Phi_T + U'(\phi_0)\Phi\Phi_x + F(\phi_0)\Phi_{xx} + G(\phi_0)\Phi_{xxx} + \ldots = 0. \tag{3.36}$$

where

$$F(\phi_0) = \frac{cos(\phi_0)}{\epsilon}\left[\left(\frac{1}{\gamma'} + \frac{1}{\gamma}\right)U(J_n)_\phi - \frac{cos(\phi_0)}{\gamma}\partial_\phi(\vec{V}_a J_n)\right], \tag{3.37a}$$

$$G(\phi_0) = \frac{\nu}{\epsilon\gamma'}cos^3(\phi_0)(J_n)_\phi. \tag{3.37b}$$

In the case when $L_s \gg L_d$ the $\Phi_{xx}$ term will be the dominant regularization. In this case equation (3.36) is Burger's equation. When $F(\phi_0)$ is negative, the shock will have a width of $O(L_s/\epsilon)$, and characteristics will flow uniformly into the shock. This leads to the decay of the shock and for large time the solution tends to a uniform constant. When $F(\phi_0)$ is positive the dissipation is acting in a negative sense, and the equation is ill-posed. Any small disturbance will tend to focus and blow up in a finite amount of time. Presumably this blow up might saturate if higher order terms are included. However, any model with this asymptotic limit presumably exhibits highly chaotic dynamics, similar to what is seen in the Kuramoto-Sivashinsky equation.

In the case when $L_s \ll L_d$ the $\Phi_{xxx}$ term will be the dominant regularization. In this case equation (3.36) is the Korteweg-deVries (KdV) equation. KdV is well known for

exhibiting soliton type solutions; lump-like objects which are exponentially localised and translate without change. The width of the soliton would be $O(L_d/\epsilon)$. Note that in terms of the surface elevation $p$ a soliton would be a step separating two regions of constant slope (figure 6). As $\epsilon$ increases, presumable this would correspond to a narrow region of width $L_d$ separating two flat regions, and translating with speed of $U(\phi_0)$.

## IV. RESULTS AND CONCLUSIONS

In this paper a formalism is described for deriving a continuum model of thin film growth. The deposition is broken into three processes: a ballistic scattering model is used to determine adsorption onto the surface; the random walk of the adatoms on the surface is described by a diffusion equation; and sticking of the adatoms to the surface is described as a Poisson process. Because the model is formulated in a coordinate independent fashion, the local dynamics, which are basically linear, lead to a fully nonlinear model of the large scale evolution. This supersedes the earlier work of Lichter and Chen (1986) who only considered linear perturbations to a flat film.

The proportion of incident atoms adsorbed can be computed from the ballistic models described in the appendix. This in turn allows the film growth rate to be computed and compared to experiment.

In the case when surface diffusion is the dominant process, an eikonal equation has been derived to describe the growth of the film. The film locally grows at a constant rate normal to its surface. The eikonal equation has a special solution of note; a sphere or spherical cap will grow in a self similar fashion with a constantly growing radius. This means a local bulge in the substrate leads to a cone like solution. In addition an imperfection seeding the medium may also cause a conical growth pattern.

The regime in which this behavior is expected is given by the mean diffusion length, $L_d \gg 1$. This parameter can be expected to depend exponentially on the inverse of the temperature (Burton et al, 1951); this implies that low substrate temperatures will cor-

respond to a large diffusion length. The cone-shaped microstructure with spherical caps corresponds to characteristic morphology of zone 1 of Movchan and Demchishin's structure zone model.

In addition, the eikonal equations predict the formation of kink like discontinuity of slopes. A network of such kinks is expected for an initially rough substrate. This network of grain boundaries seems characteristic of experimental observations (Bartholomeusz et al., 1987).

The model is also examined in the case when ballistic advection is much greater than diffusion. Here the characteristic equation describing the film's growth is a first-order wave equation. For three dimensional hard sphere scattering, the phase velocity of the wave equation is zero; consequently the solution will always grow in a self-similar fashion towards the incident flux. However, energy loss to the atomic lattice is expected (Lennard-Jones, 1937) after the substrate has been coated with the incident species. This energy loss is modelled by using a ballistic cross-section with a spherical particle with a finite effective mass. This leads to a non-uniform phase velocity for the governing wave equation. This non-uniformity will lead to shock formation which once again manifests itself as a discontinuity in the surface slope. These shocks will propagate across the film; their tracks will leave columnar like deposition.

The details of the shock structure depend upon the higher order corrections to the wave equation. Two candidates for regularizing the wave equation have been identified. When surface diffusion is small compared to the coherent scattering distance of an adatom, the regularization is dissipative, and a Burger's type equation is an appropriate model for the evolution. In this case shocks are localised and propagate (Whitham, 1974). When the diffusion length is longer than the coherent scattering length, the appropriate regularization is dispersive. Here the canonical governing equation is Korteweg-deVries. This allows the possibilty of soliton like solutions corresponding to a step-like surface geometry. These equations undoubtable exhibit a rich and varied dynamics depending on the parameter

regimes examined and consequently they are left for future study.

Note that in the diffusion dominated limit, a flat surface will grow in a direction normal to its surface independent of the direction of the incident flux. In the ballistically dominated limit, when three dimensional hard sphere scattering is considered, the surface grows at a constant rate in the direction of the incident flux independent of the surface normal. It seems logical to assume that when these two effects are comparable the surface will grow at some angle between the normal and the direction of incident flux. Experiments observe that the angle of columnar growth in zone 2 of Movchan and Demchishin's structure zone model is intermediate between these two extremes, and follows the empirical relationship known as the tangent rule (Dirks and Leamy, 1977). Our model suggests that this is effect may be due to a balance of surface diffusion and ballistic effects.

## APPENDIX. BALLISTIC COMPUTATION OF FLUX CROSS-SECTIONS

In this appendix a formalism for using the ballistics of a two sphere interaction to derive a flux and velocity cross-section on the surface of the film is presented. Consider an incident spherical particle striking a surface with a rough atomic scale. Assume that the orientation of the surface on the atomic scale is basically random. This case corresponds to the incident particle being scattered from a spherical body because the orientation of the normal to a sphere is isotropic in space. In addition, the film will have a certain degree of elasticity. This will be modelled by defining a mass ratio, $M$, between the mass of the incoming adatom and the effective mass of the particle struck in the film. The limit $M \rightarrow \infty$ correponds to scattering off a fixed hard sphere, whereas $M = 1$ corresponds to striking an unbound adatom. The study is restricted to $M$ between these limits.

Using conservation of momentum and energy allows us to relate the exit velocity $V_e$ and scattering angle, $\beta'$, as a function of the incident velocity, $V$, and impact angle, $\beta$ (figure 7). The velocity ratio can be computed as

$$\frac{V_e}{V} = \frac{\left(M^2 - sin^2(\beta')\right)^{1/2} - cos(\beta')}{1+M}. \qquad (A1)$$

The relation between the impact angle and scattering angle can only be written implicitly,

$$ctn(\beta') = \frac{cos(2\beta) - \frac{1}{M}}{sin(2\beta)}. \qquad (A2)$$

The incident flux is assumed to be arriving vertically, that is

$$\hat{J} = -\hat{z}. \qquad (A3)$$

The scattering from a unit sphere at the origin will be computed. Define spherical polar coordinates, where $\alpha, \beta$ are the azimuthal angle measured from $\hat{x}$ and the declination from $\hat{z}$ respectively. The projection along the $z$- axis is the unit circle. Define the radial component, $r$, in the $x$-$y$ plane,

$$r = (x^2 + y^2)^{1/2} = sin\beta, \qquad (A4)$$

then the differential flux density, $dJ$, is given by the flux times the area element in the plane divided by the total area of the projection,

$$dJ = \frac{J}{\pi}\, r\, dr\, d\alpha. \qquad (A5)$$

Notice that the integral over the entire cross-section simply yields $J$. Substituting (A4) into (A5) yields the cross-section as a function of $\alpha, \beta$

$$dJ = \frac{J}{\pi} sin(\beta)cos(\beta)\, d\alpha\, d\beta. \qquad (A6)$$

To compute the flux scattered out at various angles, the scattering angle must be known; assume that the particle leaves in a direction $\alpha', \beta'$ . For the geometry considered here the azimuthal angle remains the same ($\alpha' = \alpha$) and equation (A2) relates the scattering angle $\beta'$ to the impact angle $\beta$. The differential cross-section for the scattered particles can now be written as

$$dJ = \frac{J}{\pi} sin(\beta)cos(\beta) \left(\frac{d\beta}{d\beta'}\right) d\alpha'\, d\beta', \qquad (A7)$$

where it is understood that $\beta$ is a function of $\beta'$.

Finally, it is desirable to compute the differential cross section in a spherical coordinate system oriented along the normal to the surface, $\hat{n}$. Let the angle between the normal and $\hat{z}$ be denoted by $\phi$; without loss of generality it can be assumed that the normal lies in the $x$-$z$ plane and that its projection on $\hat{x}$ is negative. Define an angle of declination from the normal, $\chi$, and an azimuthal angle, $\psi$, which is measured from the $\hat{x}$ direction. The two coordinate systems are then related by

$$cos(\chi) = cos(\beta)cos(\phi) - sin(\phi)sin(\beta)cos(\alpha), \tag{A8a}$$

$$sin(\chi)cos(\psi) = cos(\beta)sin(\phi) + cos(\phi)sin(\beta)cos(\alpha), \tag{A8b}$$

$$sin(\chi)sin(\psi) = sin(\beta)sin(\alpha). \tag{A8c}$$

Equations (A8) can now be used to convert (A7) into an expression in terms of $\chi, \psi$

$$dJ = \frac{J}{\pi}\left(\frac{d\beta}{d\beta'}\right) cos(\beta)sin(\beta)\left(\frac{sin(\chi)}{sin(\beta')}\right)\, d\psi\, d\chi, \tag{A9}$$

where $\beta$ and $\beta'$ must be eliminated in terms $\psi, \chi$.

Finally, the angular cross section can be obtained by integrating over the range of $\chi$ which are deflected onto the surface. In addition, $dJ$ is the differential cross-section per unit area in the x-y plane. In the paper the incident flux per unit area on the surface of the film is desired; the ratio of these areas, which is given by the dot product of the normal to the surface and $\hat{z}$, is simply $cos(\phi)$. Consequently

$$J_\psi = cos(\phi)\int_\chi dJ. \tag{A10}$$

In the remainder of this appendix the cross sections for various particular cases are computed. Two types of surface trapping are considered; tangent trapping, where only the adatoms deflected nearly tangent to the surface will not be revaporated and will ultimately stick, and adsorption trapping where any adatom with a velocity directed into the surface after scattering is assumed to be entrapped by the surface adatom layer.

1.Three Dimensional Hard Sphere Scattering: Tangent and Adsorption Trapping

This corresponds to the case to an infinite mass ratio ($M = \infty$). From (A1,A2) it follows that

$$V_e = V \qquad \beta' = 2\beta. \tag{A11}$$

Substituting into (A7) yields

$$dJ = \frac{J}{4\pi} sin(\beta')\ d\alpha'\ d\beta' = \frac{J}{4\pi} dS', \tag{A12}$$

where $dS'$ is the element of surface area. This implies that the adatoms are scattered with a constant density per solid angle. Moreover, the cross-section is independent of surface orientation

To evaluate the integral (A10), first consider the tangent trapping case. Note that scattering with $\chi = \frac{\pi}{2}$ corresponds to leaving tangent to the surface. Define a small angle $\Delta$, corresponding to the angular cross-section around $\chi = \frac{\pi}{2}$ that are trapped by the surface. In this case $J_\psi$ can be approximated by

$$J_\psi \approx \Delta dJ|_{\chi=\frac{\pi}{2}}. \tag{A13}$$

This allows the computation of

$$J_\psi = \frac{J\Delta}{4\pi} cos(\phi) \tag{A14}$$

and (2.4) yields

$$J_n = \frac{J\Delta}{2} \cos(\phi). \tag{A15}$$

In the absorption case all adatoms with $\frac{\pi}{2} < \chi < \pi$ will be added to the surface layer. In this case,

$$J_\psi = \frac{J}{4\pi} cos(\phi), \tag{A16}$$

and

$$J_n = \frac{J}{2} \cos(\phi). \tag{A17}$$

## 2. Two-dimensional Hard Sphere Scattering: Tangent Trapping

If the two dimensional hard sphere case is considered, isotropic scattering is no longer seen; this should be taken as an omen that two dimensional ballistic simulations may have drastically different results from their three dimensional analogies.

In two dimensions the differential flux density is given by

$$dJ = \frac{J}{2}dr = cos(\beta)d\beta. \tag{A18}$$

Substituting (A11) yields

$$dJ = \frac{J}{4}cos(\frac{\beta'}{2})d\beta'. \tag{A19}$$

Note that $\chi = \beta' + \theta$. In this case $J_\psi$ is replaced by $J_+$ and $J_-$ defined as the density of adatoms scattered forward and backward repectively. Only the tangent trapping case will be computed here; for it

$$J_\pm = \pm\frac{J\Delta}{4}cos(\frac{\pi}{4} \mp \frac{\phi}{2})cos(\phi). \tag{A20}$$

The integrated flux is defined as

$$J_n = J_+ + J_- = \frac{J\Delta}{4\sqrt{2}}cos(\frac{\phi}{2})cos(\phi). \tag{A21}$$

## 3. Adatom Scattering: Tangent Trapping

In this case an adatom scattering off a particle of equal mass is considered; that is $M = 1$. Considering relationship (A2) shows that

$$\beta' = \beta + \frac{\pi}{2}. \tag{A22}$$

Consequently, $\frac{\pi}{2} < \beta' < \pi$ and for this range the velocity is given by,

$$V_\psi = -cos(\beta'). \tag{A23}$$

Substituting into (A7) yields

$$dJ = -\frac{J}{\pi}cos(\beta')sin(\chi)d\chi d\psi. \tag{A24}$$

Judicious application of equations (A8) yields

$$cos(\beta') = cos(\chi)cos(\theta) + sin(\chi)cos(\psi)sin(\theta) \qquad (A25)$$

and applying (A8) yields

$$J_\psi = -\frac{2J\Delta}{\pi}cos(\psi)cos(\phi)|sin(\phi)| \qquad (A26)$$

To evaluate the integrated flux (A26) is integrated over $\psi$ for $\beta > \frac{\pi}{2}$, to yield

$$J_n = \frac{2J\Delta}{\pi}|sin(\phi)|cos\phi. \qquad (A27)$$

4.Adatom Scattering: Adsorption Trapping

In the case of a adsorption trapping, the density given by (A24) must be integrated over the sector where $\beta', \chi > \frac{\pi}{2}$. This yields after modest calculation

$$J_n = Jcos(\phi)\left[\frac{cos^3(\phi) + cos(\phi)}{2} + \frac{sin(\phi)}{2\pi}(2\phi + sin(2\phi))\right]. \qquad (A28)$$

## BIBLIOGRAPHY

B.J. Bartholomeusz, K-H. Muller, & M.R. Jacobson, "Computer Simulation of the Nucleation and Growth of Optical Coatings," in *Modeling of Optical Thin Films*, Proceedings of SPIE, 20-21 August 1987, M.R. Jacobson, ed. **821** (1987).

W.K. Burton, N. Cabrera, & F. C. Frank, "The Growth of Crystals and the Equilibrium Structure of Their Surfaces", Phil. Trans. Roy. Soc., **A23**, 299-358 (1951).

A.G. Dirks and H.J. Leamy, "Columnar Microstructure in Vapour Deposited Thin Films," Thin Solid Films **47** 219-233 (1977).

M.P. Do Carmo, *Differential Geometry of Curves and Surfaces*, Prentice-Hall, New Jersey, 1976.

S. Lichter & J. Chen, "Model for Columnar Microstructure of Thin Solid Films", Phys. Rev. Lett. **56**, Vol. 13, 1396-1399 (1986).

J. E. Lennard-Jones, "The Interaction of Atoms and Molecules with Solid Surfaces; XI - The Disperal of Energy from an Activated Link", Proc. Roy. Soc. **A163**, 127-131 (1937).

B.A. Movchan & A.V. Demchishin, "Study of the Structure and Properties of Thick Vacuum Condensates of Nickel, Titanium, Aluminum Oxide and Zirconium Dioxide", Fiz. metal. metalloved. **28** (1969) 83-90.

G. B. Whitham, *Linear and Nonlinear Waves,* Wiley-Interscience, New York, 1974.

# FIGURE CAPTIONS

Figure 1a. Schematic of the film surface. A point on the surface is denoted by $\vec{p}$. The normal to the surface is $\hat{n}$. The incident flux $\vec{J}$ is assumed uniform and unidirectional.

Figure 1b. Control volume on the film surface. A flux balance through the top of the control surface $\mathcal{A}$ and edge $\sigma$ is shown. The normal to $\mathcal{A}$ is denoted $\hat{n}$ whereas the normal along the edge $\sigma$ is denoted $\hat{\eta}$. Flux and velocity along the surface $J_\psi$ and $V_\psi$ are defined as functions of location and polar angle on the tangent plane. At each point on $\sigma$ a directional flux $\mathcal{F}_\psi$ is defined. The flux in a direction $\hat{\psi}$ through $\sigma$ is given by $(\hat{\psi} \cdot \hat{\eta})\mathcal{F}_\psi(\vec{p}(\sigma))$.

Figure 2. Propagation of a kink along the angle bisector.

Figure 3. Sample evolution for the eikonal equation. The evolution of an initial condition corresponding to a sinusoidal substrate is shown at evenly spaced time intervals. The concavity leads to the formation of a kink type discontinuity. The kink propagates along the angle bisector of the tangent plane (cf. figure 2). Note that surface roughness decreases with increasing time.

Figure 4. Triple points. In three dimensions three kinks can originate from a single point. Near the triple point the surface can be approximated by the tangent planes to the three grains between the three kinks. The motion of the point is along the angle bisector of the dihedral angles formed by the tangent planes. The networks of kinks connecting triple points form a grain-like structure which is similar to that observed experimentally.

Figure 5. Velocity $U$ as a function of $\phi$ for various models. Note that the three-dimensional hard sphere model is identically zero. The two-dimensional hard sphere model exhibits a change of sign not seen in any of the three dimensional models. Presumably the solutions for finite mass ratios ($M$) greater than unity lie between the $M = 1$ and $M = \infty$ cases and also exhibit a single maximum.

Figure 6. Soliton propagation. Equation (3.36) has soliton like solutions in the dispersively regularised limit. The soliton in $\phi$ corresponds to a step in surface elevation of width $L_d$ between regions of uniform slope. The step, like the soliton will propagate with a speed $U(\phi_0)$.

Figure 7. Schematic of a scattering collision. The incident particle, $m_1$, with initial velocity $V$ strikes the stationary particle $m_2$ at an impact angle $\beta$. It is scattered through an angle $\beta'$ with an exit velocity $V_E$. The ballistic cross-section can be examined, and $\beta'$ and $V_E$ can be computed as a function of $V$, $\beta$, and the mass ratio $M = m_2/m_1$.

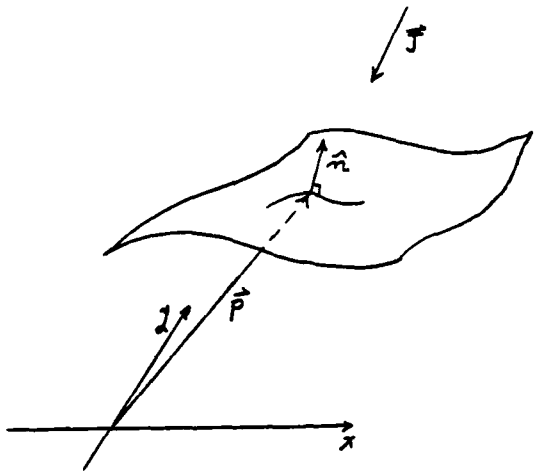


FIG. 1a

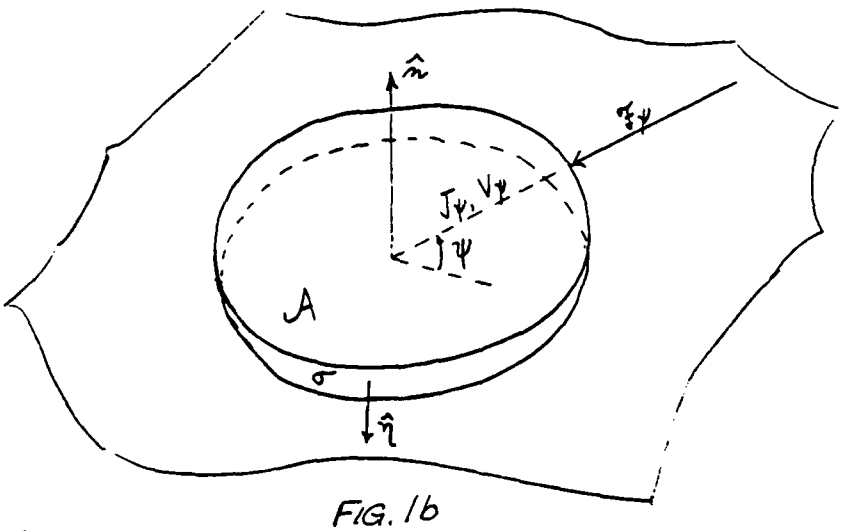


FIG. 1b

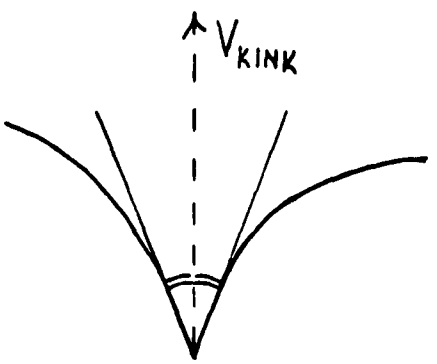


FIG. 2

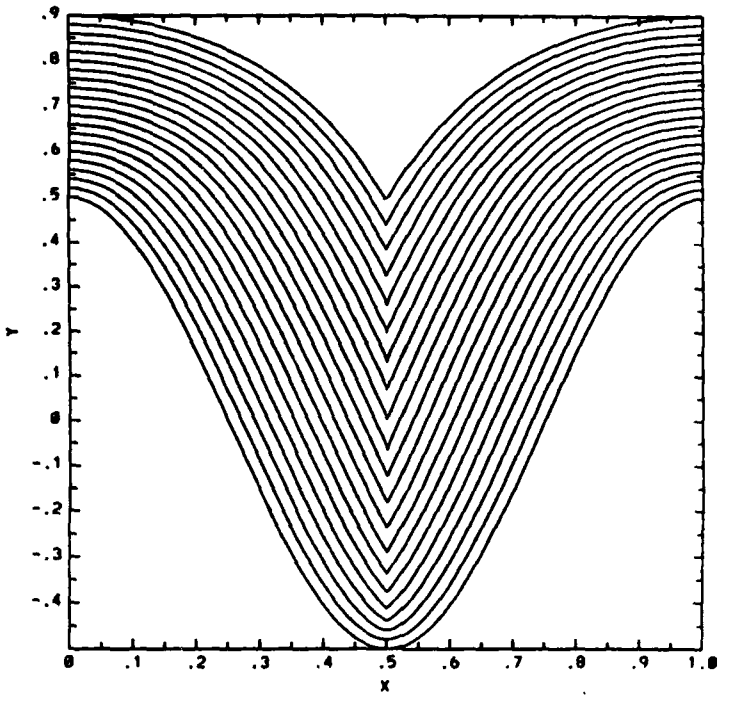


FIG. 3

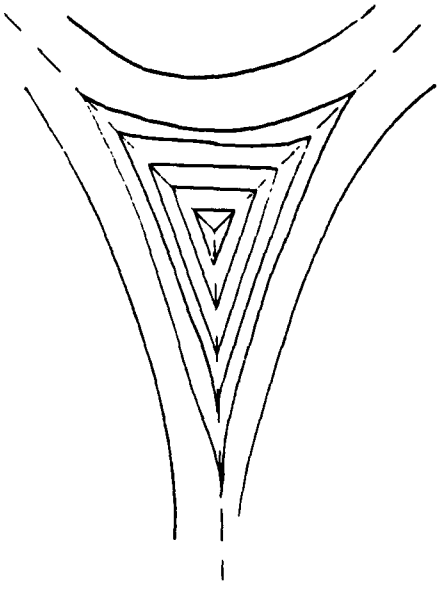

FIG. 4

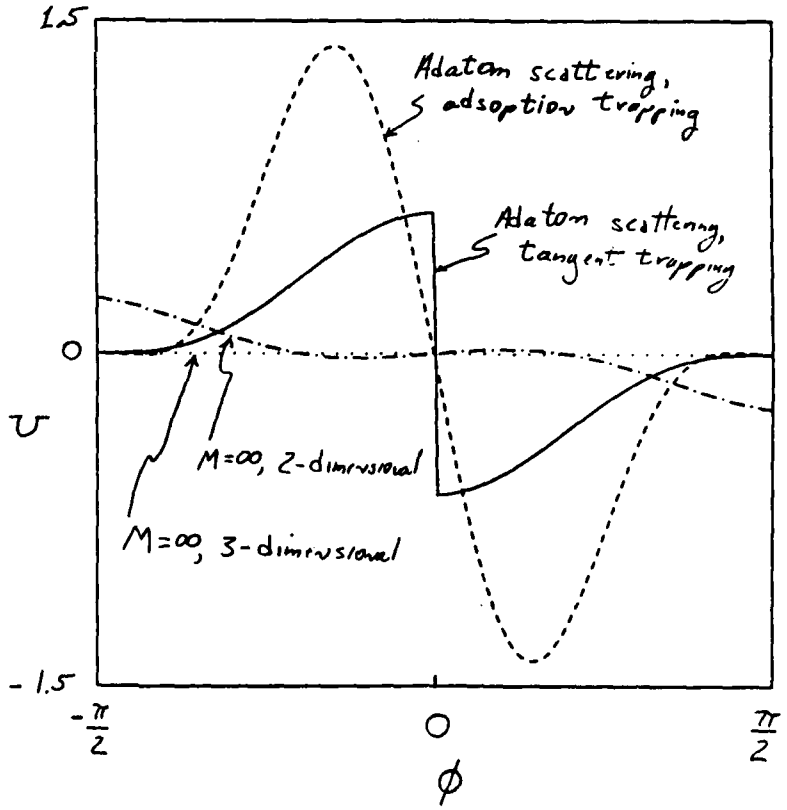


FIG. 5

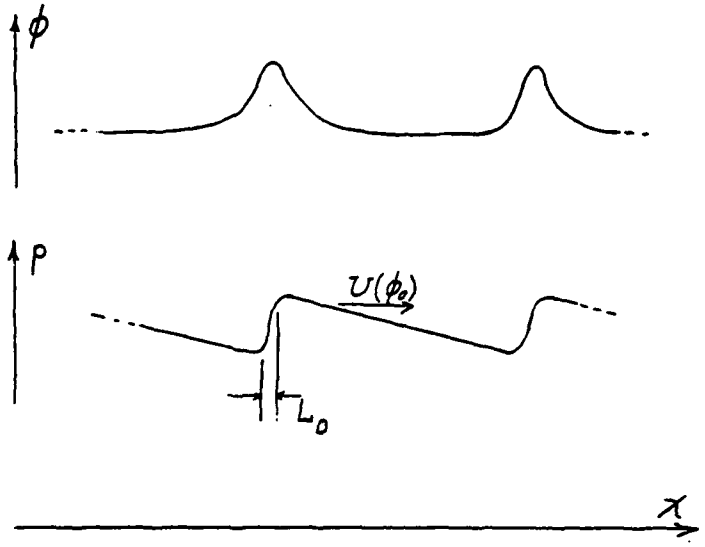


FIG. 6

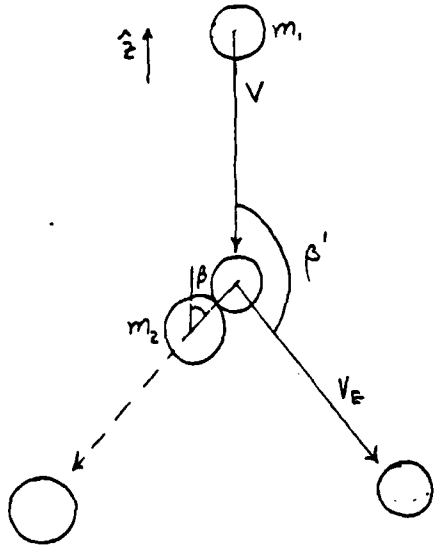


FIG. 7

# APPENDIX E

## Analysis and Results of Existing Instrumentation - W. Wolfe

One aspect of the project has been the development of instrumentation to measure the performance and properties of thin films. Although there is no dearth of capability to measure the spectral distribution of both the reflectivity and transmissivity of thin films, there is a paucity of measurement capability for the assessment of the scattering characteristics of these films. This section addresses accomplishments and ideas concerning the three-dimensional properties of scattering from thin films: scattering as a function of position on the surface as well as depth effects.

*Current Instrumentation*

First, the instrument developed provides a good, relative assessment of the scattering characteristics of a surface, whether it is a simple surface or one with coatings. Light illuminates the surface at an incidence angle of about 80°. It thus provides a rather shallow, broad spot on the surface of the sample; there is relatively little depth penetration. The light is from a HeNe laser and is well collimated. Viewing is normal to the surface, with a microscope objective of numerical aperture 0.4 and focal spot 7 $\mu$m. The detector behind this optic is a silicon photodiode. The geometry is shown in Fig. 1. The spot can be scanned over a total field of 1×1 mm$^2$ by controlling the motion of the sample, which is situated on an x-y stage, using a computer. The illuminated spot is actually much larger than the viewing spot.

*What does this system actually measure and what information does it provide?*

The viewing system senses all the light scattered toward it in its solid-angle field of view. This is a combination of the light scattered from the surface and the illuminated sub-surface "slice" that is within the field of the view of the receiver. Although the interpretation is not straightforward, the patterns of relative intensity are very nice.

Shown in Fig. 2 are the results of a spatial scan on a section of Halon. Halon is a material that is used as a photometric reference standard in the visible spectral region. It is almost isotropic and has a hemispherical reflectivity of almost one. It accomplishes these two feats by being rough (with respect to wavelength) and non-absorbing. The pattern shown indicates a measured intensity ratio of about 5:1 over the scanned field of 0.1×0.1 mm. This spatial pattern is not inconsistent with a Lambertian reflector. On a scale of 7 $\mu$m the surface is inhomogeneous. The surface is rough with respect to the wavelength, and it does reflect more or less in a

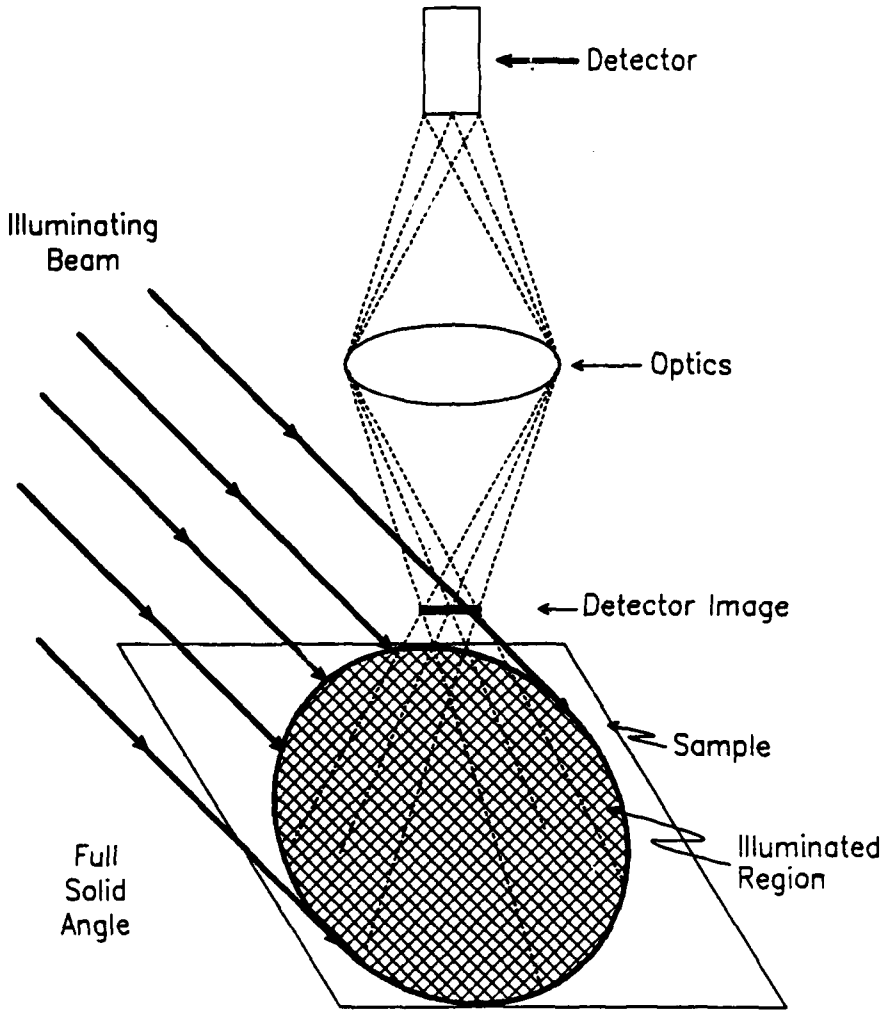


*Figure 1. Geometry of illumination and sensing.*

particular direction for each small area. The BRDF curve, shown in Fig. 3, reveals that these variations must average to give a uniform pattern.

Shown in Fig. 4 is the pattern of a highly reflecting, specular surface. It too varies from spot to spot. The scanning scatterometer also provides a reasonable representation of its homogeneity (or lack thereof). A BRDF plot is given in Fig. 5.

It is reasonable to ask whether a BRDF measurement could be used to calibrate the scanning scatterometer (SS). The answer is, "Yes, but. . . ." We compare the SS to the AZSCAT (Arizona Scatterometer). Both can be made to have the same incidence angle and wavelength. However, the AZSCAT collects radiation from a 1-cm diameter spot and 1-$\mu$sr field, whereas the SS collects from a 7-$\mu$m diameter

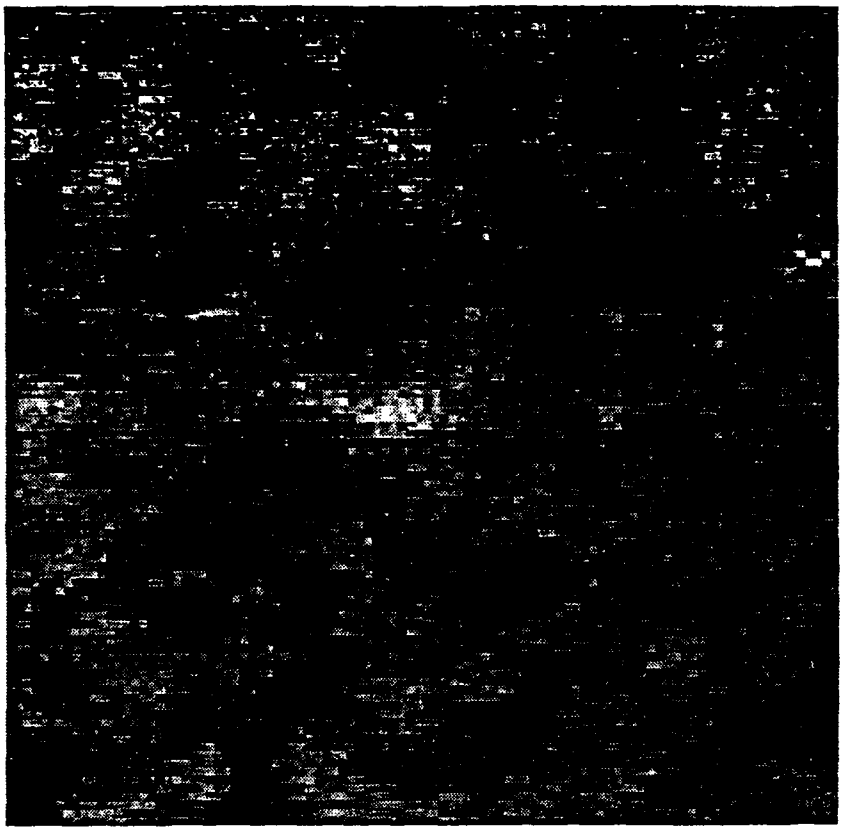

*Figure 2. Halon scan; 0.1×0.1 mm.*

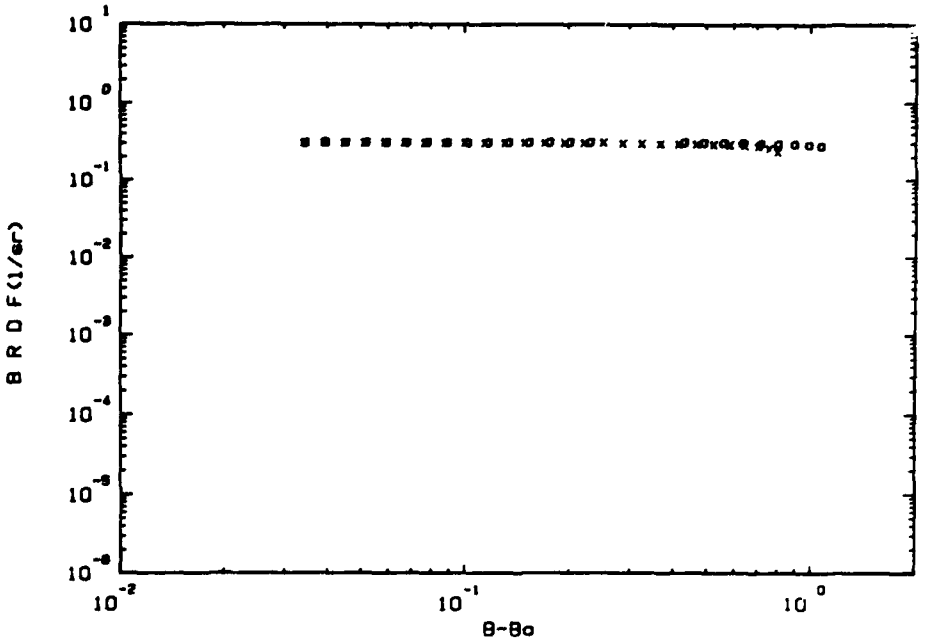


*Figure 3. Halon scan; BRDF plot: Xs are B - Bo > 0, Os are B - Bo < 0.*

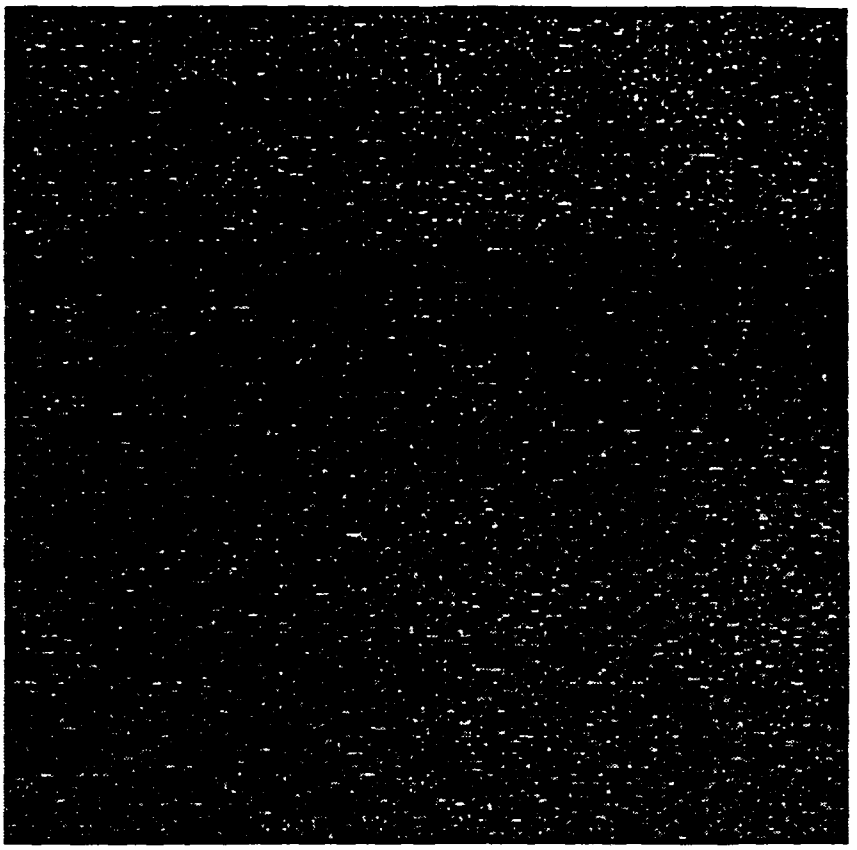

*Figure 4. Highly reflective, specular surface; 5 Å rms sample, 200×200 μm.*

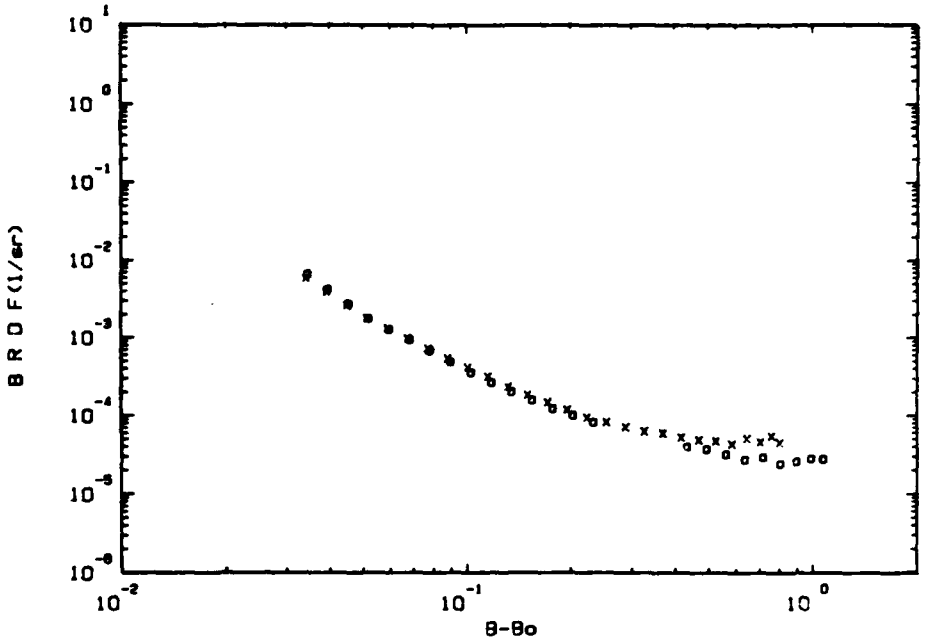


*Figure 5. BRDF plot for sample in Fig. 4 (Xs are B -Bo > 0, Os are B -Bo < 0).*

spot and 0.3-sr field. To generate equivalence, the SS results would have to be integrated over more than its whole field of view, and the AZSCAT results would have to be integrated over one-third its total range. This is more integration than has been done in the United States since the Civil War!

So, AZSCAT measures angle-resolved scattering over relatively large spots and the SS measures angle-integrated scattering from small spots. Each is useful; each is different; they are complementary probes.

Of course it is interesting to ask whether there is a way to calibrate, regularize, rationalize the two instruments so that a calibrated BRDF spatial scan could be made. It seems clear that one should make the spot of the AZSCAT as small as that of the SS or make the angle of the SS as small as that of AZSCAT—or at least make the two approach each other. There are two issues involved. One is radiometric sensitivity; the other is instrumental capability.

The fundamental equation for the noise equivalent BRDF in this situation is

$$\text{NEBRDF} = \frac{R^2\sqrt{A_d B}}{E_i A_o A_r \cos\theta_i \theta_s D^*}$$

where

$R$ = distance from the sample to the detector
$A_d$ = detector area
$B$ = noise bandwidth
$E_i$ = sample irradiance
$A_o$ = observation area
$A_r$ = receiver area
$\theta_i$ = angle of incidence
$\theta_s$ = angle of scatter
$D^*$ = specific detectivity

With appropriate implementation, the bandwidth B can be 1 Hz and the detector area $A_d$ can be 20 $\mu$m on a side ($4\times10^{-6}$ cm$^2$). A reasonable value for the distance R is 20 cm and for the laser power 5 mW. The $D^*$ of a good silicon detector is about $10^{12}$ cmHz$^{1/2}$W$^{-1}$. So most of the values are fixed, chosen or determinable. For these values

$$\text{NEBRDF} = \frac{(400\ \text{cm}^2)(20\times10^{-4}\ \text{cm})(1\ \text{Hz})}{(E_i A_o A_r \cos\theta_i \cos\theta_s)\times10^{12}\ \text{cmHz}^{1/2}\text{W}^{-1}}$$

$$= \frac{0.8\times10^{-12}\ \text{cm}^2\text{W}}{E_i A_o A_r \cos\theta_i \theta_s}$$

If the viewing is done normally, then $\theta_i = \theta_s$. If it is $60^0$ then $\cos\theta = 0.5$. The irradiance will be the power divided by the beam area divided by the cosine of the incidence angle. Thus

$$\text{NEBRDF} = \frac{A_b(1.6\times10^{-12}\ \text{cm}^2\text{W})}{P_I A_o A_r}$$

If one now requires that the NEBRDF is $10^{-6}\text{sr}^{-1}$, then $A_oA_r$ must be $10^{-4}\text{cm}^{-4}$. The product of the observation area and the collecting area is a constant. One can back off some and require that

$$A_o\Omega = \frac{10^{-4}}{400} = 0.25\times10^{-6}\ \text{cm}^2\text{sr}$$

The system throughput is a constant. For 10 $\mu$m and 0.3 sr, this is $3\times10^{-7}$ or $0.3\times10^{-6}$. These are approximately the parameters of the SS. For the AZSCAT, the parameters are approximately 1 cm and $10^{-6}$sr. The AZSCAT could reduce its observation area, but not by much. So neither instrument can be improved by much—except by greatly increasing the observation time.

It would seem from this analysis that there is no way to properly compare the two instruments. The SS measures the scattering from a small spot over a large angular area. The AZSCAT measures the scattering from a large spot over a small angular area. For BRDFs on the order of $10^{-6}\text{sr}^{-1}$ in the visible, neither can be improved markedly. These are the BRDFs of interest. For larger ones, comparisons can be made and measured. For instance, a BRDF of $10^{-2}\text{sr}^{-1}$ .somewhat lower than a perfect isotropic reflector at $0.3\text{sr}^{-1}$ could be accomplished by decreasing the collection angle of the SS with an aperture stop, and increasing the collection angle of the AZSCAT with a collection lens. Other such maneuvers are possible.

*Instrumentation for Bulk and Surface Measurements*

In the beginning there was light, and specular reflection measurements were made. But man grew sophisticated and wished to know how light scatters from materials. And now he would like to measure how much scatters from the surface and how much from the volume. Not an easy question! (But it is easier than how this all began.)

"Traditional" scatter measurements are made by shining light on a transparent surface and viewing the light that is either back scattered or forward scattered from that "spot." Of course every optical system views a solid angle, so the scattered light is not from the spot but from the entire solid angle that is viewed. This means that most measurements of BTDF include surface scatter, subsurface scatter and

volume scatter. Most BRDF measurements of reflecting, opaque surfaces include surface and some subsurface scattering. Most BRDF measurements of transparent samples include volume scattering as well as the scattering from both surfaces. Separation of these effects is possible to some extent, but it is not easy.

Consider the geometry of Fig. 6. The beam is incident at some carefully chosen, arbitrary angle. The light that gets to the aperture scatters from the front surface over an area B1 with a certain BRDF. It scatters as well from the sample volume between B1 and B2 in the beam. It also scatters from the back surface B2. These are the primary scatterers. Next, the scatter from B1 is specularly reflected from the back surface and scattered from the back surface. The incident beam is scattered from the volume to the back surface and reflected up. These are secondary scatterers. Tertiary ones include scatter from the front to the back and back and then up; from the volume to the back and up; from the back through the volume and up, back to front and up. It is hoped that higher-order scattering can be neglected. The message here is that scattering in a non-absorbing sample is a highly complex matter. In the diagram shown, the flux on the aperture comes from the first-surface BRDF at one angle, second-surface BRDF at another, volume scatter at an intermediate angle, and then there are second-order effects. Emphasis can be applied to front-surface, back-surface, or volume scattering depending upon the geometry, as shown in Figs. 7, 8 and 6 respectively.

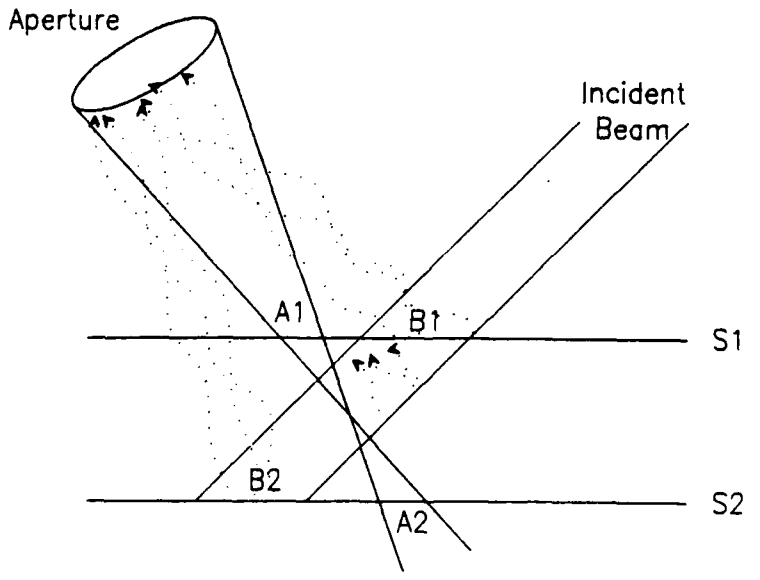


*Figure 6. A possible scattering geometry.*

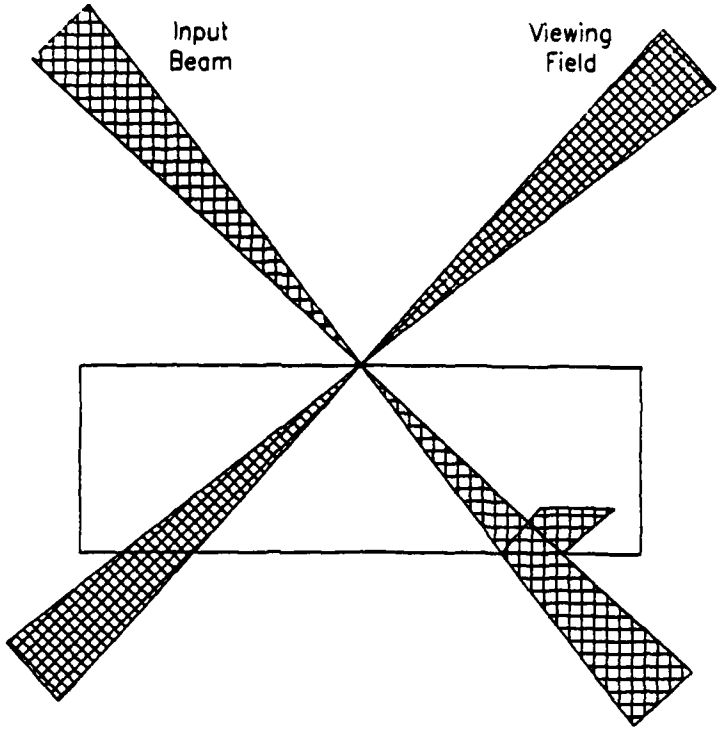


*Figure 7. Emphasis of front-surface scatter.*

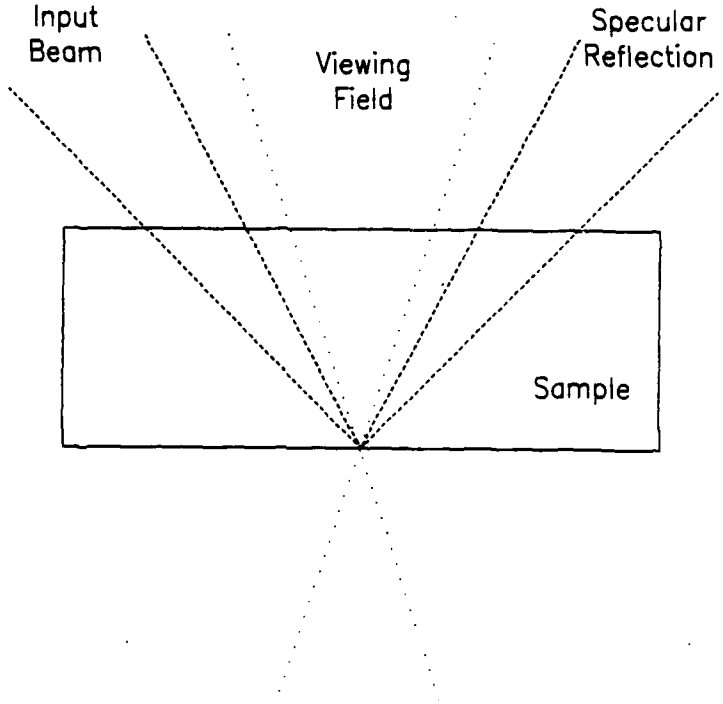


*Figure 8. Emphasis of back-surface scatter.*

One approach to modeling all this, and therefore to measuring it, is to calculate the BRDF from the first surface based on the well-known formulae and the geometry, add to this the BRDF from the second surface—with a slightly different angle (based on Snell's Law), and add an appropriate amount of surface scatter. All these must be weighted by the solid angles of collection. Several measurements at different incidence and scatter angles must be made to separate the effects.

A second approach, that may be used to complement the first, is the use of frustrated total internal reflection. The frustration in this case is the result of scatter, rather than the close juxtaposition of another material. The geometry of the radiometry is critical. The collimated beam is arranged to exit the sample at a critical angle.

The specular beam is then totally reflected by a perfectly smooth surface. A rough surface will scatter some of the beam out of the surface—according to the well-known equations of the vector EM Theory. Some light is also scattered by the volume into angles that are less than critical. By careful focusing and direction of the field of view of the receiver, the scattering from the near-surface structure can be emphasized. The entire secret seems to be to consider as carefully as possible the focusing geometries of both beams. One approach is shown in Fig. 7, where the collimated beam is viewed as it would strike and where it doesn't. If both beams are focused on the surface, the emphasis is on the surface scatter. It may not completely separate surface from volume scatter, but it should emphasize one over the other to an extent that significant measurements can be made. The geometry is shown in Fig. 9.

A third approach is that of nephelometry. The input beam and viewing field are arranged such that the beam strikes the surfaces only outside the field of view. The main scatter will then be that from the volume, but it will be modified by the surface. It should also be possible to move the field to measure the surface to obtain correlative data. This is shown in Fig. 6, where neither surface is viewed.

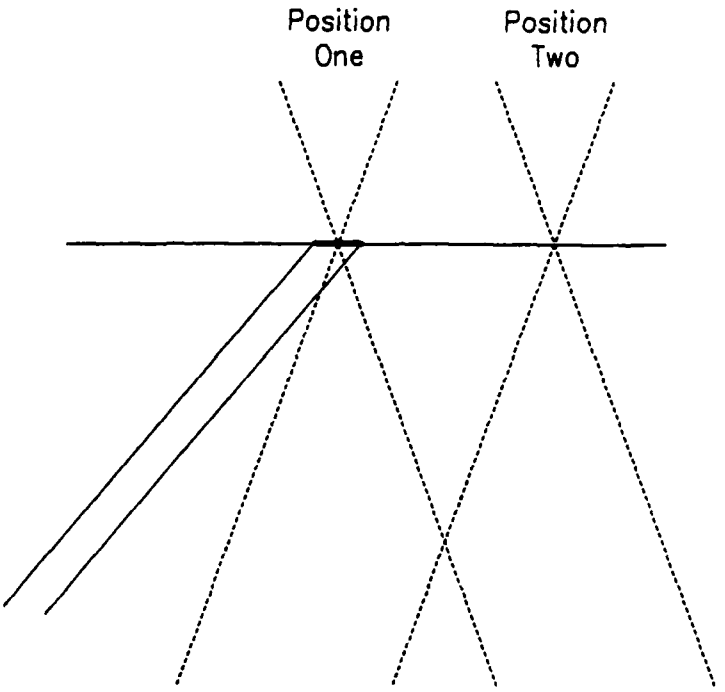


*Figure 9. Critical incidence viewed in two positions.*

# APPENDIX F

# Anisotropic Orientation Distribution in Polycrystalline Langmuir-Blodgett Monolayers Revealed by Second-Harmonic Generation

Victor Mizrahi, George I. Stegeman, and Wolfgang Knoll*

Optical Sciences Center

University of Arizona

Tucson, Arizona 85721

**Abstract**

We demonstrate, by the use of second-harmonic generation, that a significant anisotropy in Langmuir-Blodgett monolayers may be imposed by the deposition process. This represents the first demonstration of a systematic influence on the properties of a prepared monolayer due to the type of film balance employed.

**PACS numbers:** 78.65-s, 68.55-a, 42.65 Ky.

*Permanent address:

Max-Planck-Institut für Polymerforschung

Jakob-Welder-Weg 11, D-6500 Mainz, FRG

Monolayer studies with cyanine dyes at the water-air interface were of great interest in the past because of their technical importance as sensitizers in photography.[1,2] Recently, they have been used more generally as model systems for the study of the crystallization and self-organization processes in quasi two-dimensional systems.[3-6] Moreover, these monomolecular layers are the basic units for the build-up of multilayer assemblies by the Langmuir-Blodgett dipping technique[7] aimed at tailoring, at the molecular level, functional superstructures[8] with special properties. Thus techniques are necessary that allow for a sensitive characterization of the geometric as well as electronic structure of mono- and multilayers. Second-harmonic generation (SHG), with its intrinsic surface and thin film sensitivity, has been shown to fulfill these requirements. Previous workers have derived information about molecular hyperpolarizabilities or orientational properties of single molecules or parts of the molecules.[9-14]

We will show in this letter that structural information is also available at the supramolecular level of single crystallites and demonstrate this by elucidating the slight anisotropy in the orientation of elliptically shaped monomolecular crystallites,[5] so-called J-aggregates,[15,16] on the water surface. We show that this anisotropy is maintained during the transfer process and is dependent on the type of Langmuir film balance employed for the preparation of the monolayer.

The cyanine dye used is S120, (1-methyl-1'-octadecyl-2,2'-cyanine iodide, structural formula given in Fig. 1, kindly provided by Dr. K. Wirthensohn, University of Munich) which can be spread, compressed, and thereby organized at the water-air interface.[17] The break in the pressure-area isotherm (Fig. 1) marks the onset of the formation of crystalline, highly fluorescing aggregates which are induced by increasing the lateral pressure $\pi$ to above 5 mN m$^{-1}$. These J-[15] or Scheibe[16]-aggregates can be grown to dimensions of 10 to 100 $\mu$m. A typical ensemble of elliptically shaped, randomly oriented crystallites is shown in the inset of Fig. 1. This fluorescence-microscopic picture was taken from the water surface at $\pi \cong 15$ mN m$^{-1}$ with polarized light. Only those aggregates with their transition dipole moment parallel to the E-field fluoresce brightly.

For the preparation of the J-aggregate monolayers, two differently designed Langmuir troughs were used. The first one was a commercial (Joyce-Loebl, JL for short) tank equipped with a Wilhelmi plate for the pressure reading. A special feature of this system is the half-immersed teflon-coated glass-fiber ribbon which confines the spread molecules to a well-defined area (Fig. 2a). Compression is achieved at constant perimeter by two counterpropagating overarms which leave the center line of the working area still (see Fig. 2a). The second trough is home built (HB) and equipped with an integrated fluorescence microscope.[18] Here, compression is performed by a single moving barrier which slides over the edges of the teflon frame (Fig. 2b). The resulting compression speed profile across the monolayer is substantially different from the first one (schematically indicated in both figures by the length of the arrows) with considerable shear stress along the long edges of the frame. Fluorescence microscopy during compression shows that this stress relaxes stochastically in the densely-packed J-aggregate layers which are very stiff. The result is a slight positionally dependent orientational redistribution of the crystallites.

The monolayers were transferred onto hydrophobic substrates as follows: First, two clean BK-7 slides were mounted together with edges sealed with Teflon ribbon in order to prevent subphase liquid from penetrating between the plates. This assembly was then coated with one cadmium arachidate monolayer by the usual vertical dipping technique. Dye monolayer transfer onto the front side was subsequently performed on the down stroke - either by hand or by a mechanical sample lift with the substrate being mounted nearly horizontally. The angle $\alpha$ between an arbitrarily chosen axis in the plane of the substrate and the center line of the monolayer could be chosen freely (see Figs. 2) to an accuracy of $\pm 5^{\circ}$. While submerged the substrate was rotated to the vertical and the water surface aspirated. A protective overlayer of arachidic acid was added in a conventional upstroke. Finally the two slides were separated and only the front one was used for the experiments. This procedure ensured the coating of only one side of the substrate, with the back side being absolutely free of contamination.

The laser at frequency $\omega$ was incident on the center of the substrate at an angle $\theta$ relative to the surface normal, with the dye monolayer on the second surface of the glass slide. The intersection with the beam is adjusted to insure that a fixed spot on the sample is illuminated when the sample is rotated around the normal to the surface by an angle $\Phi$.[19,20] The second-harmonic (at $2\omega$) generated by the film travels collinearly with the laser beam and is detected in the forward direction. The laser beam consists of 35 ps pulses at 10 pulses per second at a wavelength of 1.064 $\mu$m. Typical experimental pulse energies were 1 mJ spread over a measured beam diameter ($1/e^2$) of 2.3 mm. Polarizers allowed for a free choice of $\hat{s}$- or $\hat{p}$-waves for both frequencies, $\omega$ and $2\omega$.

We describe the SHG process by a nonlinear polarization, $P_{2\omega}$, associated with the monolayer, induced by the electric field of the laser, $E_\omega$:

$$P_{2\omega} = \chi^{(2)} : E_\omega E_\omega \ . \tag{1}$$

The form of $\chi^{(2)}$ is determined by the crystal symmetry of the J-aggregates. For a single oriented J-aggregate, the second-harmonic signal may then be calculated in the usual way.[21] In fact, fluorescence microscopy shows that the film consists of a macroscopic distribution of J-aggregates (see inset of Fig. 1), each of which is oriented at an angle $\Phi_1$, relative to some $\hat{y}$ axis of the film as a whole. The laser beam samples $\cong 10^3$ J-aggregates whose dimensions are large compared with the second-harmonic wavelength. We therefore average the second-harmonic signal[9] from a single oriented J-aggregate over the macroscopic distribution function, $\rho(\Phi_1)$. Here $\rho(\Phi_1)$ is the number of aggregates oriented at $\Phi_1$, per unit $\Phi_1$. Thus the total second-harmonic signal is given by

$$S(\Phi) = \int_0^{2\pi} \rho(\Phi_1)\, S^{mic}(\Phi - \Phi_1) d\Phi_1 \ . \tag{2}$$

where $S^{mic}$ is the second-harmonic signal from an individual J-aggregate oriented at $\Phi - \Phi_1$ relative to the laboratory frame $\Phi = 0$ axis. We now expand both the distribution

function $\rho(\Phi_1)$, and $S^{mic}$ in a Fourier series and obtain

$$\rho(\Phi_1) = \sum_{m=0}^{\infty} \rho_m \cos(m\phi_1 + \delta_m) \tag{3}$$

and

$$S^{mic}(\Phi - \Phi_1) = \sum_{n=0}^{\infty} S_n \cos[n(\Phi - \Phi_1) + \epsilon_n] \, . \tag{4}$$

Generally only a few terms in this last series are required to specify $S^{mic}(\Phi - \Phi_1)$. Substituting Eqs. (3) and (4) into Eq. (2), performing the integration and setting $\delta_0 = \epsilon_0 = 0$ gives

$$S(\Phi) = \pi \cdot \rho_0 S_0 + \pi \sum_{m=0}^{\infty} \rho_m S_m \cos(m\Phi + \delta_m + \epsilon_m). \tag{5}$$

Clearly $S(\Phi)$ will show an angular dependence containing only those spatial frequencies present in both $S^{mic}(\Phi)$ *and* $\rho(\Phi_1)$. Since we expect that $S^{mic}$ from a single J-aggregate has lower than isotropic symmetry, we can deduce from $S(\Phi)$ information about the macroscopic distribution function $\rho(\Phi_1)$. Alternatively, given $\rho(\Phi_1)$, it is possible to determine the microscopic symmetry class of the individual J-aggregate.[20]

The $\Phi$-dependence of the second-harmonic signal observed under $\hat{p}_{in} \rightarrow \hat{p}_{out}$ conditions (i.e., incident laser $\hat{p}$ polarized, analyzer set to record only $\hat{p}$-polarized second-harmonic output), from a dye layer deposited in the JL trough with $\alpha = 0^0$, is shown in Fig. 3a. Clearly, the sample is not macroscopically isotropic, but shows a two-fold rotational symmetry. This result is somewhat surprising, as it has generally been believed that molecules on the water surface of a Langmuir-trough are isotropically distributed. We, on the other hand, are dealing here - at least in the late stage of the isothermal compression - with large, elliptically shaped crystallites. It is therefore well conceivable that the two moving belts apply an uniaxial force to the aggregates which leads to some orientation upon compression. To test this, and to rule out that the observed anisotropy

in the macroscopic distribution function was induced during the transfer process, we deposited another film on a similar substrate, but this time with the slide rotated to approximately $\alpha = 45^0$ in the plane of the water surface (horizontal dipping is employed throughout) so that the compression axis was rotated $45^0$ relative to a marked edge of the substrate. The SHG measurements of this film are shown in Fig. 3b. As expected for our interpretation, the origin of the curve is shifted by approximately $45^0$ and the direction of the shift is correct. The slight assymmetries are attributed to a residual lateral inhomogeneity, which can be directly observed by scanning the laser beam across the sample.

When the monolayer is prepared on the HB trough with the single compressing barrier, Fig. 4 shows that for $\alpha = 0$ the twofold symmetry of the distribution function is again found under $\hat{p}_{in} \rightarrow \hat{p}_{out}$ conditions. However there is a loss of the correlation between the azimuth dipping angle $\alpha$ and the phase angle $(\delta_m + \epsilon_n)$ of the $\phi$-scan, $S(\phi)$. In order to ensure that the observed phase angles are not influenced by the hand-dipping process, a mechanical sample lift was employed which could be positioned prior to the monolayer deposition to a much better angular accuracy. Despite the obvious loss in phase correlation, these samples seem to be more isotropic in their macroscopic orientation distribution as judged from the considerably reduced modulation. Also the lateral homogeneity was significantly better, as checked by a separate experiment. As demonstrated by the full lines in Fig. 4, the angular dependence can be described by a single cos $2\Phi$ function, with negligible improvement by adding some cos $4\Phi$ contributions (not shown).

In concluding we note that for most applications of LB films, (poly-) crystalline monolayers of different materials are grown on the water surface and then transferred to the solid support. We have, we believe for the first time, demonstrated a systematic influence of the type of film balance employed on the properties of the prepared monolayer. And we have shown that SHG is a sensitive tool to monitor even subtle anisotropies in the macroscopic orientation distribution of polycrystalline monolayers.

## Acknowledgments

This research was supported by AFOSR contract number AFOSR-87-0344 and JSOP contract number F4962-88-C-0009.

## References


1. D. F. O'Brien, Photgr. Sci. Eng. 17, 226 (1973).
2. R. Steiger and F. Zbinden, J. Imaging Sci. 32, 64 (1988).
3. H. Kuhn, Thin Solid Films 99, 1 (1983).
4. H. Grüninger, D. Möbius, and H. Meyer, J. Chem. Phys. 79, 3701 (1983).
5. C. Duschl, M. Lösche, A. Miller, A. Fischer, H. Möhwald, and W. Knoll, Thin Solid Films 133, 65 (1985).
6. C. Duschl, D. Kemper, P. Meller, H. Ringsdorf, and W. Knoll, submitted.
7. K. B. Blodgett and I. Langmuir, Phys. Rev. 51, 980 (1937).
8. H. Kuhn, D Möbius, and H. Bücher, in *Physical Methods of Chemistry*, Vol. 1, Part 3B, A. Weissberger and B. W. Rossiter, eds., (Wiley, New York, 1972).
9. J. R. Girling, N. A. Cade, P. U. Kolinsky, J. D. Earls, G. H. Cross, and J. R. Peterson, Thin Solid Films 132, 101 (1985).
10. Th. Rasing, Y. R. Shen, M. W. Kin, P. Valint, Jr., and J. Bock, Phys. Rev. A 31, 537 (1985).
11. Th. Rasing, Y. R. Shen, M. W. Kim, and S. Grubb, Phys. Rev. Lett. 55, 2903 (1985).
12. Th. Rasing, G. Berkovic, Y. R. Shen, S. G. Grubb, and M. W. Kim, Chem. Phys. Lett. 130, 1 (1986).
13. G. Berkovic, Th. Rasing, and Y. R. Shen, J. Opt. Soc. Am. B 4, 945 (1987).
14. J. R. Girling, N. A. Cade, P. V. Kolinsky, R. J. Jones, I. R. Peterson, M. M. Ahmad, D. B. Neal, M. C. Petty, G. G. Roberts, and W. J. Feast, J. Opt. Soc. Am. B 4, 950 (1987).
15. E. E. Jelley, Nature 139, 631 (1937).
16. G. Scheibe, Kolloid Zeitschrift 82, 1 (1938).
17. C. Duschl, W. Frey, C. Helm, J. Als-Nielsen, H. Möhwald, and W. Knoll, Thin

Solid Films 159, 386 (1988).

18. M. Lösche and H. Möhwald, Rev. Sci. Instrum. 55, 1968 (1984).

19. V. Mizrahi, F. Suits, J. E. Sipe, U. J. Gibson, and G. I. Stegeman, Appl. Phys. Lett. 51, 427 (1987).

20. Victor Mizrahi, G. I. Stegeman, and Wolfgang Knoll, in preparation.

21. Victor Mizrahi and J. E. Sipe, J. Opt. Soc. Am. B 5, 660 (1988). Note that in Eq. (3.33) the $\epsilon(2\omega)$ should have been $\epsilon'(2\omega)$.

## Figure Captions

Fig. 1. Pressure-area curve of a cyanine dye (S120, structure formula given in the inset) monolayer on pure water (Millipore quality, pH 5.5, T = 22°C). The onset of J-aggregate formation is indicated by the arrow. The inset shows a fluorescence microscopic picture taken from the water surface with polarized excitation at a pressure $\pi$ = 15 mN $m^{-1}$. The area shown corresponds to 75×100 $\mu$m.

Fig. 2a. Schematic top view of the Joyce-Loebl Langmuir trough used for some of the J-aggregate monolayer preparations. Special features are the two counterpropagating overarms which control the active area by means of the Teflon-coated glass-fiber ribbon at constant perimeter. The arrows indicate the resulting compression speed profile on the monolayer with the characteristic center line of speed zero. There the (near) horizontal transfer of the condensed monolayers (at $\pi$ = 40 mN $m^{-1}$) onto the hydrophobic substrate was performed by hand at various angles $\alpha$.

Fig. 2b. Schematic top view of the home made Langmuir trough which was equipped with an integrated fluorescence microscope. Compression is performed with a single moving Teflon barrier gliding over the edges of the teflon frame. The resulting compression speed profile with its shear stress at the edges is again indicated by the arrows. Deposition of the monolayer onto the substrate was performed by a mechanical sample lift.

Fig. 3. Angular $\Phi$ dependence of the second-harmonic intensity of a S120 J-aggregate monolayer transferred form the Joyce-Loebl trough at $\alpha$ = 0° (a) and $\alpha$ = 45° (b). Angle of incidence 35°, laser pulse energy 1.5 mJ; $\hat{p}$-polarization for $\omega$ and $2\omega$ radiation. Note the corresponding phase shift of the $\Phi$-scan.

Fig. 4. Same as in Fig. 3, but for a monolayer prepared in the home-built Langmuir trough. For (a), $\alpha = 0^0$ and the modulation can be fit (solid line) to the single cosine function $1.53 + 0.18 \cos (2\Phi - 32^0)$. For (b), $\alpha = 45^0$ and the full line corresponds again to a single cosine function $1.41 + 0.15 \cos (2\Phi - 157^0)$). Note the uncorrelated phase of the $\Phi$-scan.

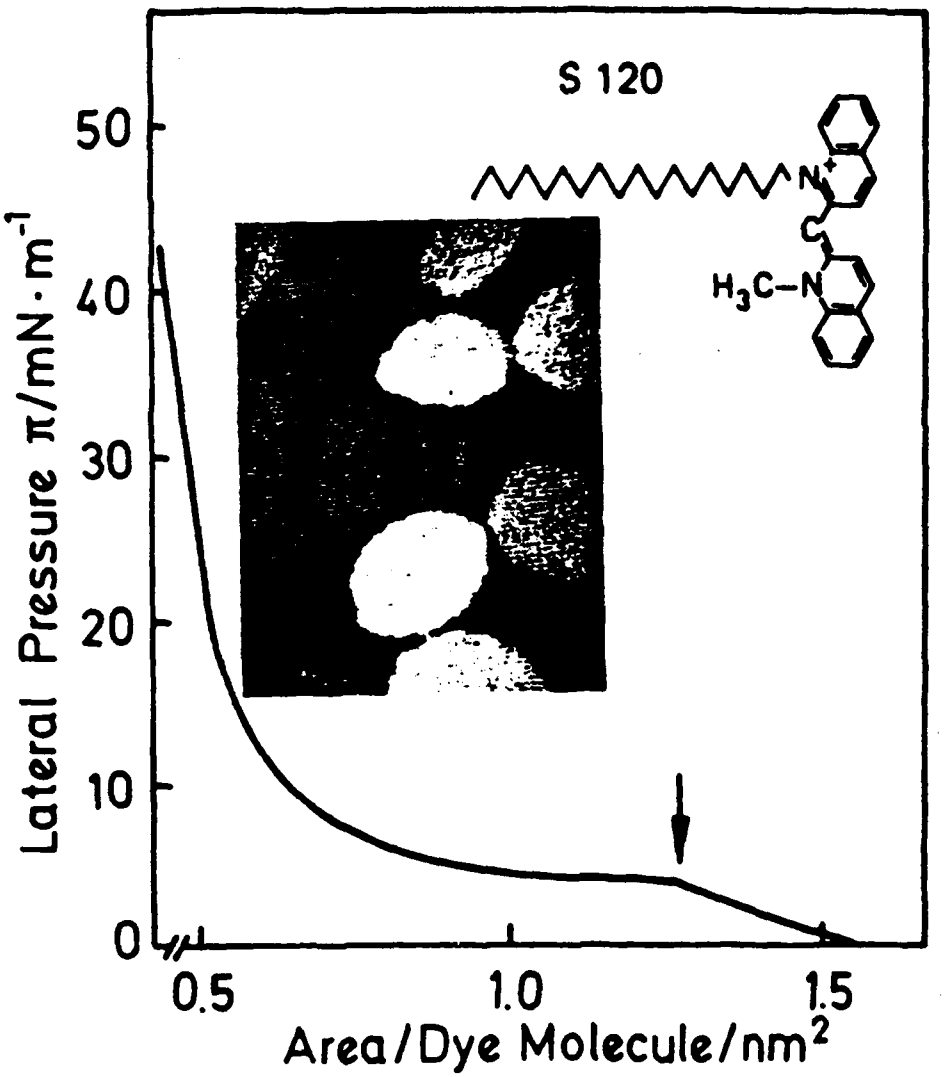
S 120
$H_3C-N$
Lateral Pressure π/mN·m$^{-1}$
50
40
30
20
10
0
0.5
1.0
1.5
Area/Dye Molecule/nm$^2$

Fig. 1

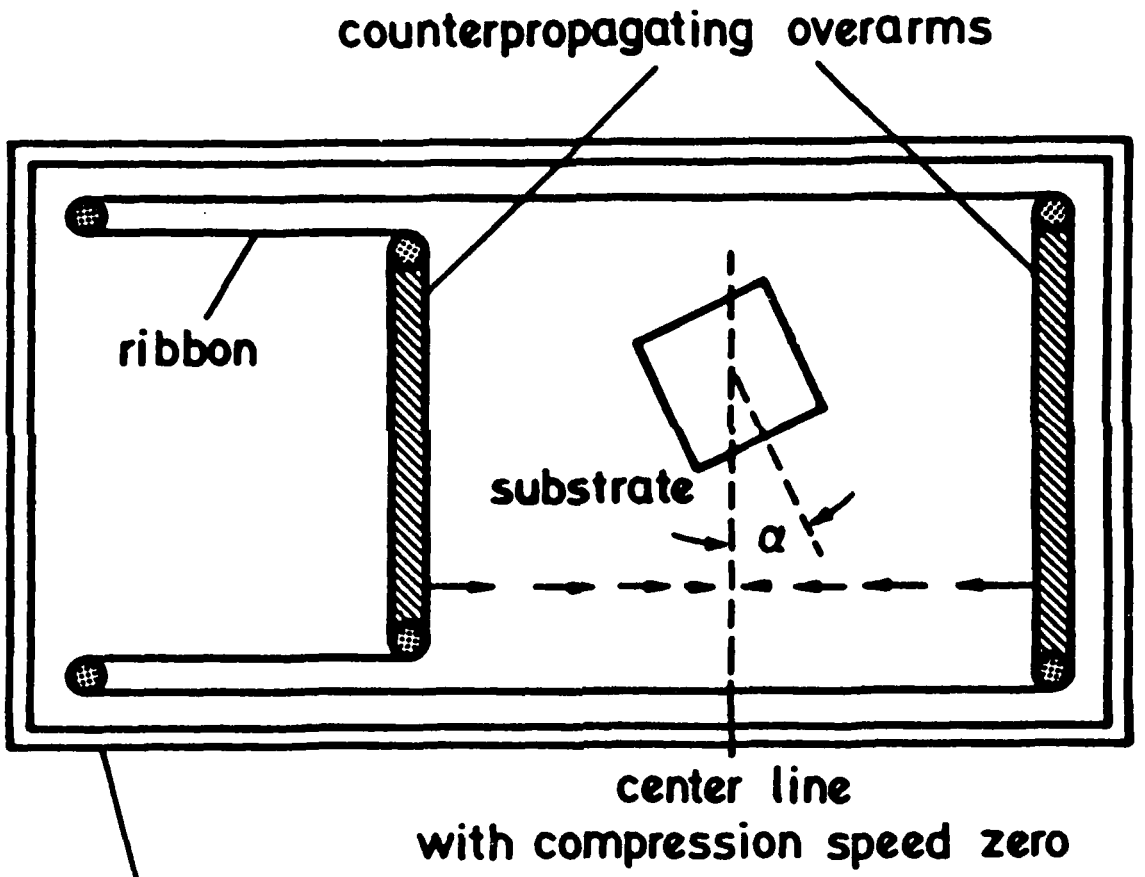
counterpropagating overarms
ribbon
substrate
α
center line
with compression speed zero
teflon trough

Fig. 2a

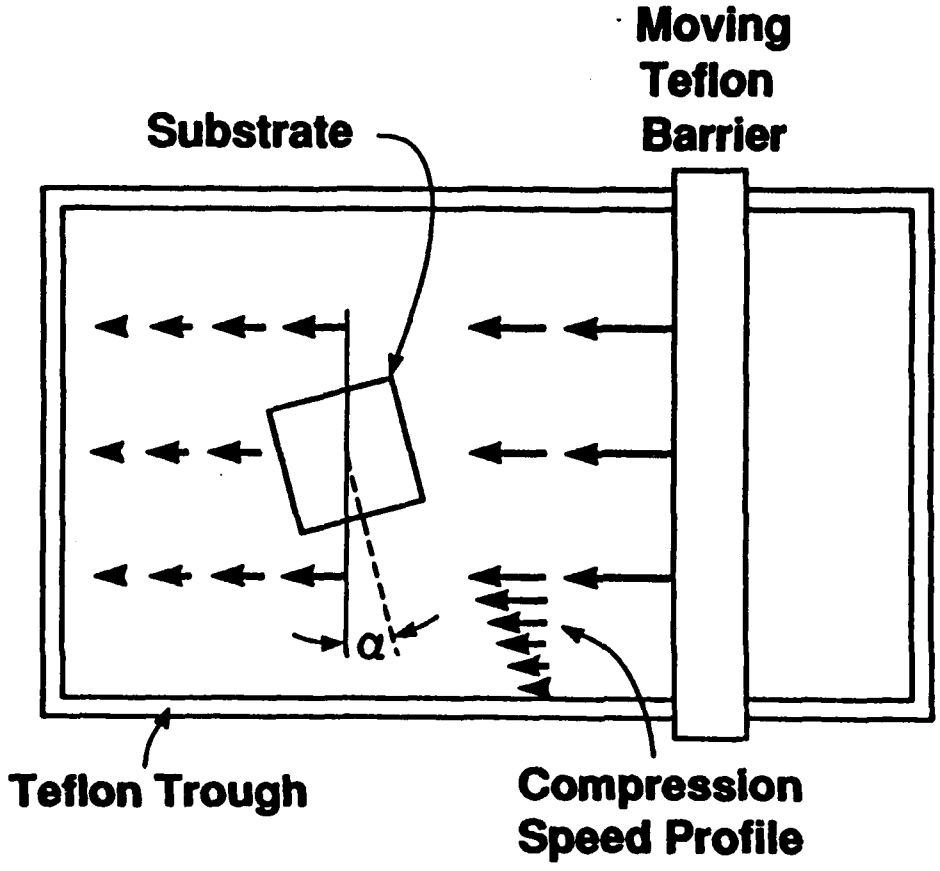
Moving
Teflon
Barrier
Substrate
α
Teflon Trough
Compression
Speed Profile

Fig. 26
(50%) rec

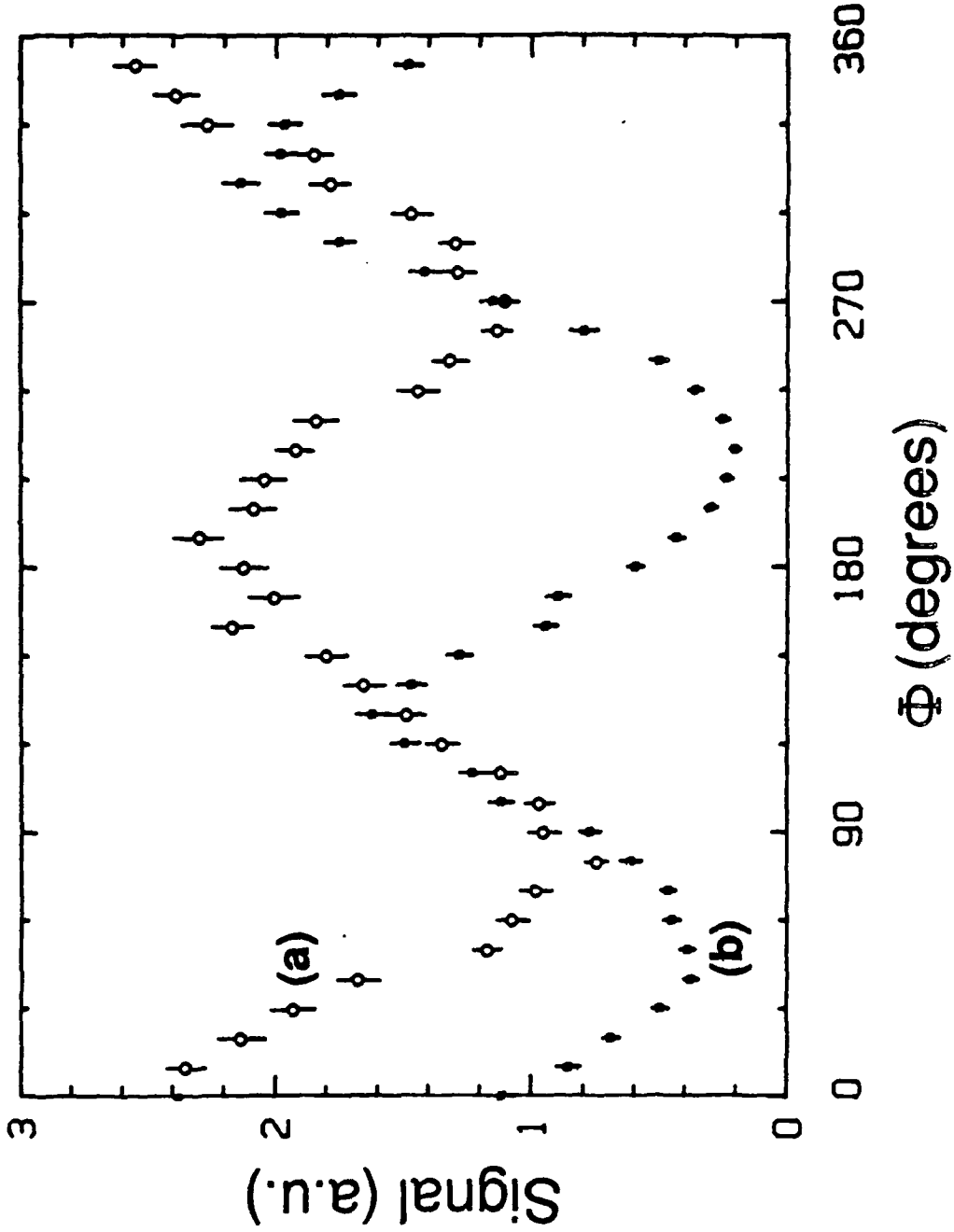


Fig 3

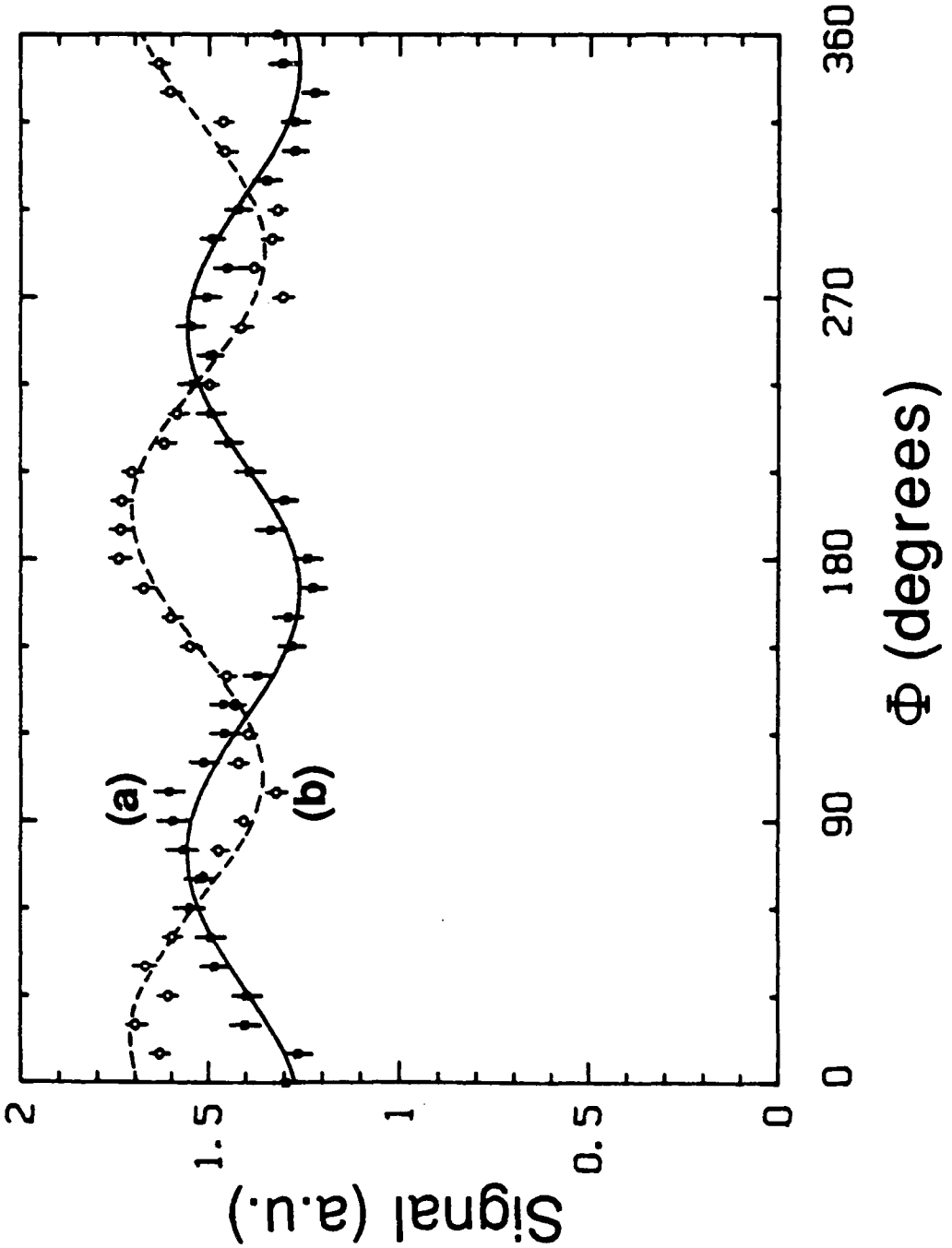
Signal (a.u.)
2
1.5
1
0.5
0
0
90
180
270
360
Φ (degrees)
(a)
(b)